

SEL-77-026

NON-LINEAR GYRORESONANT INTERACTIONS OF ENERGETIC PARTICLES
AND COHERENT VLF WAVES IN THE MAGNETOSPHERE

by

Umran Savas Inan

August 1977

Technical Report No. 3414-3

Prepared under

National Aeronautics and Space Administration
Contract NGL 05-020-008
Office of Naval Research
Contract Nonr N00014-75-C-1095
Contract Nonr N00014-76-C-0689

Radioscience Laboratory
Stanford Electronics Laboratories
Stanford University Stanford, California

This research is a Ph. D. dissertation submitted to Stanford University.
It is dedicated to my mother and father

HAYRIYE and MUSTAFA INAN

and to my wife

ELIF INAN

ABSTRACT

The study of wave particle interactions in the earth's magnetosphere has advanced markedly in the last decade. Understanding of these interactions is important because of their possible impact on the ionosphere in general and VLF and ULF communications in particular, their control of the radiation belt particles and the role played by the waves in diagnostics of the magnetosphere. One important class of wave particle interactions is the gyroresonant interaction of coherent VLF whistler mode waves and energetic particles. The waves involved can be natural whistlers or discrete emissions or signals injected into the magnetosphere from VLF ground transmitters, such as the Stanford University transmitter at Siple, Antarctica, and large scale power grids. These coherent waves interact in the cyclotron-resonance mode with the energetic particles trapped in the radiation belts. As a result the waves grow or decay in amplitude and the particles are perturbed in pitch angle and energy. The perturbations in pitch angle are of special importance in that they result in precipitation of particles into the ionosphere. Until recently this effect has only been studied using linear theory and analytical techniques. In the present work, a computer simulation study of this interaction is made with special emphasis on computing the wave's effect on the particles. With this approach it is possible to obtain a full nonlinear solution of the equations of motion in an inhomogeneous medium. The nonlinear results are compared with those of the linear theory and a convenient criterion is presented for determining when a complete nonlinear solution is required. It is found, for example, that in the case of equatorial scattering by a 5 kHz CW pulse near $L = 4$

linear theory begins to break down when the wave amplitude exceeds 3 mV. We represent a full distribution of energetic particles by 40-50,000 test particles, distributed appropriately in phase space. By computing the complete trajectories of all these particles the perturbation of the full distribution is estimated. The wave induced precipitated flux is computed and it is shown that significant particle fluxes (order of 10^{-1} ergs/cm²-sec) can be precipitated into the atmosphere by waves of moderate intensity (order of 10 mV). These fluxes produce significant perturbations in the nighttime ionosphere. Both the incoming fluxes and the ionospheric perturbations appear to be measurable by presently available instruments.

TABLE OF CONTENTS

<u>Chapter</u>	<u>Page</u>
I. INTRODUCTION	1
A. THE EARTH'S INNER MAGNETOSPHERE	1
B. REVIEW OF PREVIOUS WORK	8
C. OUTLINE OF THE REPORT	10
D. CONTRIBUTIONS OF THE PRESENT WORK	13
II. BASIC PHYSICS AND EQUATIONS OF MOTION	15
A. THE MODEL MAGNETOSPHERE	15
B. DYNAMICS OF RADIATION BELT PARTICLES	18
C. COHERENT VLF WHISTLER MODE WAVES IN THE MAGNETO- SPHERE	27
D. EQUATIONS OF MOTION	43
E. ENERGY AND MOMENTUM TRANSFER	52
F. LINEAR THEORY	55
III. DESCRIPTION OF THE SIMULATION	59
A. INTRODUCTION	59
B. COMPUTATION OF THE MEDIUM PARAMETERS	59
C. MAIN SIMULATION	60
IV. STUDY OF THE INTERACTION	68
A. SCATTERING OF A SINGLE RESONANT SHEET	68
B. QUANTITATIVE CRITERIA FOR DETERMINING THE APPLICABILITY OF LINEAR THEORY	87
C. THE TRAPPED MODE	97
V. PRECIPITATED FLUX FROM A FULL DISTRIBUTION OF PARTICLES . .	117
A. SIMULATION OF THE DISTRIBUTION FUNCTION	117
B. COMPUTATION OF FLUX FOR A PARTICULAR CASE	122

TABLE OF CONTENTS (Cont.)

<u>Chapter</u>	<u>Page</u>
C. LEVERAGE	133
D. IONOSPHERIC EFFECTS	135
VI. CONCLUSIONS	140
A. SUMMARY AND DISCUSSION	140
B. MEASUREMENTS OF THE PRECIPITATED FLUX	142
C. INTENSITY OF COHERENT WAVES IN THE MAGNETOSPHERE	144
D. DISCUSSION	146
E. APPLICATIONS AND FUTURE IMPLICATIONS	151
F. SUGGESTIONS FOR FUTURE WORK	153
APPENDIX A.	157
APPENDIX B.	160
APPENDIX C.	163
APPENDIX D.	165
REFERENCES	176

LIST OF TABLES

<u>Table</u>	<u>Page</u>
1 Parameter values for the example case	71
2 Values of ρ for different cases	94

ILLUSTRATIONS

<u>Figure</u>	<u>Page</u>
1.1 The general outline of the magnetosphere	3
1.2 The inner magnetosphere, dipole field lines, plasma-pause and some energetic particle trajectories.	4
2.1 Coordinate system and symbols for the dipole geometry and the diffusive equilibrium model	16
2.2 Particle motion in a homogeneous static magnetic field . . .	19
2.3 The trajectory of an energetic particle trapped in the earth's field	22
2.4 Cross field drifts	26
2.5 A typical whistler event	32
2.6 Observation of transmitter signals on the IMP-6 satellite	35
2.7 Transmitter signals received at the conjugate point in Roberval, Canada.	36
2.8 Reception of transmitter signals	37
2.9 Examples of power-line radiation into the magnetosphere....	38
2.10 Spectrogram of a typical example of observation of ELF hiss on the OGO-4 satellite	39
2.11 Longitudinal whistler-mode wave fields	42
2.12 Coordinate system for the equations of motion	45
2.13 The quantity η , defined as the ratio of percentage pitch angle change to percentage energy change as a function of pitch angle	54
3.1 Computation of the medium	61
3.2 Complete interaction of the wave and a test particle . . .	63
3.3 Sample particle trajectories	66
4.1 Description of the interaction studied in this section . .	69
4.2 Single particle trajectories for $B_w = 10$ mG.	70

ILLUSTRATIONS (Cont.)

Figure		Page
4.3	Single particle trajectories for $B_w = 50$ mγ.	74
4.4	Total scattering $\Delta\alpha_{eq}$ versus initial phase for different wave amplitudes, for $L = 4$ and $n_{eq} = 400$ el/cc... .	77
4.5	Comparison of results of linear theory and the full nonlinear analysis	81
4.6	RMS and mean scattering for linear and nonlinear analyses as a function of wave amplitude	82
4.7	Initial pitch angle dependence of the total scattering versus ϕ_0 for $n_{eq} = 400$ el/cc and $B_w = 10$ mγ. . . .	84
4.8	Variation of total scattering with equatorial cold plasma density, n_{eq}	86
4.9	Total scattering as a function of resonance point along the field line	88
4.10	Total scattering as a function of wave intensity for $\alpha_{eq_0} = 70^\circ$	99
4.11	$ \Delta\alpha_{eq} $ for the $\phi_0 = 0$ particle versus α_{eq_0} for three different wave intensities	100
4.12	Trajectory of a strongly trapped particle	102
4.13	$ \Delta\alpha_{eq} $ for the $\phi_0 = 0$ particle versus B_w for different α_{eq_0}	105
4.14	$ \Delta\alpha_{eq} $ for the $\phi_0 = 0$ particle versus B_w for different α_{eq_0}	109
4.15	Interaction length, L_I , versus B_w plotted for different α_{eq_0}	110
4.16	Percentage energy change, ΔK_E , for the $\phi_0 = 0$ particle versus α_{eq_0} plotted for different B_w	112
4.17	Total absolute energy change in electrons volts versus α_{eq_0} plotted for different B_w	113
4.18	Percentage energy change ΔK_E versus B_w plotted for different α_{eq_0}	114

ILLUSTRATIONS (Cont.)

<u>Figure</u>		<u>Page</u>
4.19	RMS scattering $\sqrt{\langle (\Delta\alpha_{eq})^2 \rangle}$ versus ρ	116
5.1	Simulation of the distribution function	118
5.2	Pitch angle dependence of the two distributions used in the calculations	124
5.3	Normalized particle distribution $f(\alpha)$	126
5.4	The one-pass precipitated flux in the 1-2 keV range as a function of wave intensity	130
5.5	Precipitation induced density enhancements produced by three monoenergetic incoming fluxes at 1.5, 7 and 30 keV..	137

LIST OF PRINCIPAL SYMBOLS

B_o	= geomagnetic field
B_w	= wave magnetic field
e	= electronic charge, 1.602×10^{-19} coulombs
f	= wave frequency, $\omega/2\pi$
f_H	= electron gyrofrequency, $\omega_H/2\pi$
f_p	= electron plasma frequency, $\omega_p/2\pi$
$f(v_{\parallel}, \alpha)$	
$f(v, \alpha)$	= energetic particle distribution functions
$f(v_{\perp}, v_{\parallel})$	
k	= wave number
K_E	= kinetic energy, $\frac{1}{2} mv^2$
L	= equatorial geocentric distance (in earth radii) of the magnetic field line. Defined on p. 15, Eq. (2.3).
L_I	= interaction length
m	= mass of an electron, 9.109×10^{-31} kg.
n_{eq}	= equatorial cold plasma density
n	= wave refractive index
N_T	= total number density of precipitated electrons
N_e	= number density of isotropically distributed energetic electrons in the 1-2 keV energy range.
Q	= precipitated energy deposition rate
R	= geocentric distance
R_o	= radius of the earth, 6370 km.
$v_{p,g}$	= wave phase and group velocities
v	= energetic electron velocity

LIST OF PRINCIPAL SYMBOLS (Cont.)

- $v_{\parallel, \perp}$ = components of the energetic particle velocity parallel and perpendicular to the static magnetic field.
- v_R = local cyclotron-resonance velocity, $\frac{\omega_H - \omega}{k}$.
- v_k = 1.9×10^7 m/sec, velocity corresponding to 1 keV energy, $\frac{1}{2} mv^2 = 1$ keV.
- z = distance along the field line.
- α = particle pitch angle, $\tan^{-1} \left(\frac{v_{\perp}}{v_{\parallel}} \right)$
- α^{1c} = half angle of the loss cone. Defined on p. 23.
- λ = geomagnetic latitude.
- θ = wave normal angle, $\angle (\vec{k}, \vec{B}_0)$
- τ_B = bounce period of energetic particles.
- δ = wave polarization
- ρ = ratio of wave and inhomogeneity forces. Defined on p. 91.
- ϕ = phase of the energetic electron with respect to the wave, $\angle (v_{\perp}, -\vec{B}_w)$.
- ϕ_u = unperturbed phase, i.e. ϕ for $B_w \approx 0$.
- η = ratio of the percentage pitch angle and energy changes. Defined on p. 53.
- Φ = differential energy spectrum (number of electrons per unit area per unit time per unit solid angle per unit energy).
- Φ_1 = differential energy spectrum of ~ 1 keV electrons with $\alpha \approx 90^\circ$.
- $\Delta(\cdot)$ = change in the quantity (\cdot) .
- $(\cdot)_{eq}$ = equatorial value of the quantity (\cdot) .

ACKNOWLEDGEMENTS

This research was supervised by Professor R. A. Helliwell and Dr. T. F. Bell. Their advice, encouragement and experience have significantly affected its course both in topic and content. I wish to express my sincere appreciation for their support and guidance. I am particularly indebted to them for the physical insights gained during countless stimulating discussions on many aspects of this research.

I would also like to thank my third reader Prof. O. Buneman for his interest and useful comments and Dr. M. Walt of the Lockheed Physical Sciences Laboratory for his comments on Chapters 4 and 5.

My thanks are also due to members of the VLF group of the Radio-science Laboratory of Stanford, especially to Prof. J. P. Katsufakis for his support and encouragement, to Drs. D. L. Carpenter and C. G. Park for their careful and critical reading of the manuscript, to all the other members of the group for their cooperation and friendship and to Dr. T. L. Crystal with whom I not only had many constructive discussions but also had the pleasure of sharing an office for four years. I want also to thank all persons involved in the preparation of the manuscript and especially to Barbara DeClue for her excellent and conscientious typing.

I am grateful to my parents for their continuous moral support and to my wife Elif for her inspiration, patience and encouragement throughout the course of this work.

This research was supported in part by the National Aeronautics and Space Administration under grant NGL-05-020-008 and in part by the Office of Naval Research under grants N00014-75-C-1095 and N00014-76-C-0689. The bulk of our computations were made on the CDC7600 computer of the National Center for Atmospheric Research (NCAR) in Boulder, Colorado, which we have used through a Remote Job Entry Terminal at Stanford. Our use of this facility was made possible by a computer time grant from NCAR. NCAR is sponsored by the National Science Foundation.

1. The first part of the report is a general
introduction to the subject of the study.
It discusses the importance of the study and
the objectives of the research. The second part
of the report is a detailed description of the
methodology used in the study. This includes
a description of the data collection methods,
the sample size, and the statistical methods
used to analyze the data. The third part of
the report is a discussion of the results of the
study. This includes a description of the
findings and a discussion of the implications
of the results. The final part of the report
is a conclusion and a list of references.

I. INTRODUCTION

The subject of this research is the nonlinear cyclotron resonance wave-particle interaction in the magnetosphere, with particular emphasis on the wave-induced perturbations of the energetic particles. In this section we give a brief introduction to the topic and describe the present work and the specific contributions.

A. THE EARTH'S INNER MAGNETOSPHERE

The immediate environment of the earth consists of (i) the neutral atmosphere, extending up to 60 km above the earth's surface, (ii) the ionosphere, a region of highly ionized gas (heavy ions, protons and electrons) as well as neutral particles extending up to about 1000 km altitude, and (iii) the magnetosphere consisting mainly of protons and electrons and extending up to a distance of $\sim 100,000$ km from the earth. Although the boundary between the atmosphere and the ionosphere is rather abrupt, such is not the case for the ionosphere-magnetosphere boundary. The magnetosphere could be viewed as a smooth continuation of the ionosphere and has often been referred to as the 'outer ionosphere.'

The structure and the physical processes of the magnetosphere are controlled mainly by the earth's magnetic field and the energy from the sun. This energy arrives at the earth in different forms and is deposited at different locations. Some is introduced at the outer boundary by the solar wind, a hot (10^5 K) solar gas, mainly protons and electrons traveling outward from the sun at speeds of ~ 500 km/s. Containing 5-10 charged particles per cm^3 at 1 A.U., the solar wind is prevented from reaching the earth itself by the effects of the earth's magnetic field. A bow-shock is formed at $\sim 12 R_0$, with the solar wind dragging magnetic lines of

force around the earth in the anti-solar direction, forming a large tail containing plasma and magnetic field. A sketch of the magnetosphere is shown in Fig. 1.1. For a thorough discussion of solar wind and magnetosphere interaction the reader is referred to Akasofu and Chapman [1972].

The region of interest for this report is the inner magnetosphere. This is the region within about 7 earth radii of the earth. A good approximation to the earth's magnetic field in this region is that of a centered dipole inclined with respect to the rotation axis by about 11° . A sketch of the inner magnetosphere and the dipole field lines is shown in Fig. 1.2.

The inner magnetosphere is populated by background 'cold' plasma, mainly electrons and protons in the 0.1 eV to 1 eV energy range. Often the inner magnetosphere exhibits an abrupt boundary, called the plasma-pause, at which the electron concentration drops by roughly two orders of magnitude [Carpenter, 1963]. Its geocentric distance is highly variable ranging from 2 earth radii after the onset of a major substorm to as much as 7 earth radii after a long (several days) period of quieting. The region inside the plasmapause is called the plasmasphere [Carpenter and Park, 1973]. The thermal or 'cold' plasma is created through ionization by solar ultra-violet radiation in the daytime F region of the ionosphere, and flows upward along field lines into the plasmasphere. At night, ionization stored in the plasmasphere flows downward to help maintain the nighttime F region [Park, 1970]. The cold plasma in the plasmasphere is commonly assumed to be a neutral isothermal mixture of electrons and positive ions (mainly H^+ , but some He^+ and O^+) which is in diffusive equilibrium along the magnetic field lines under the effect of

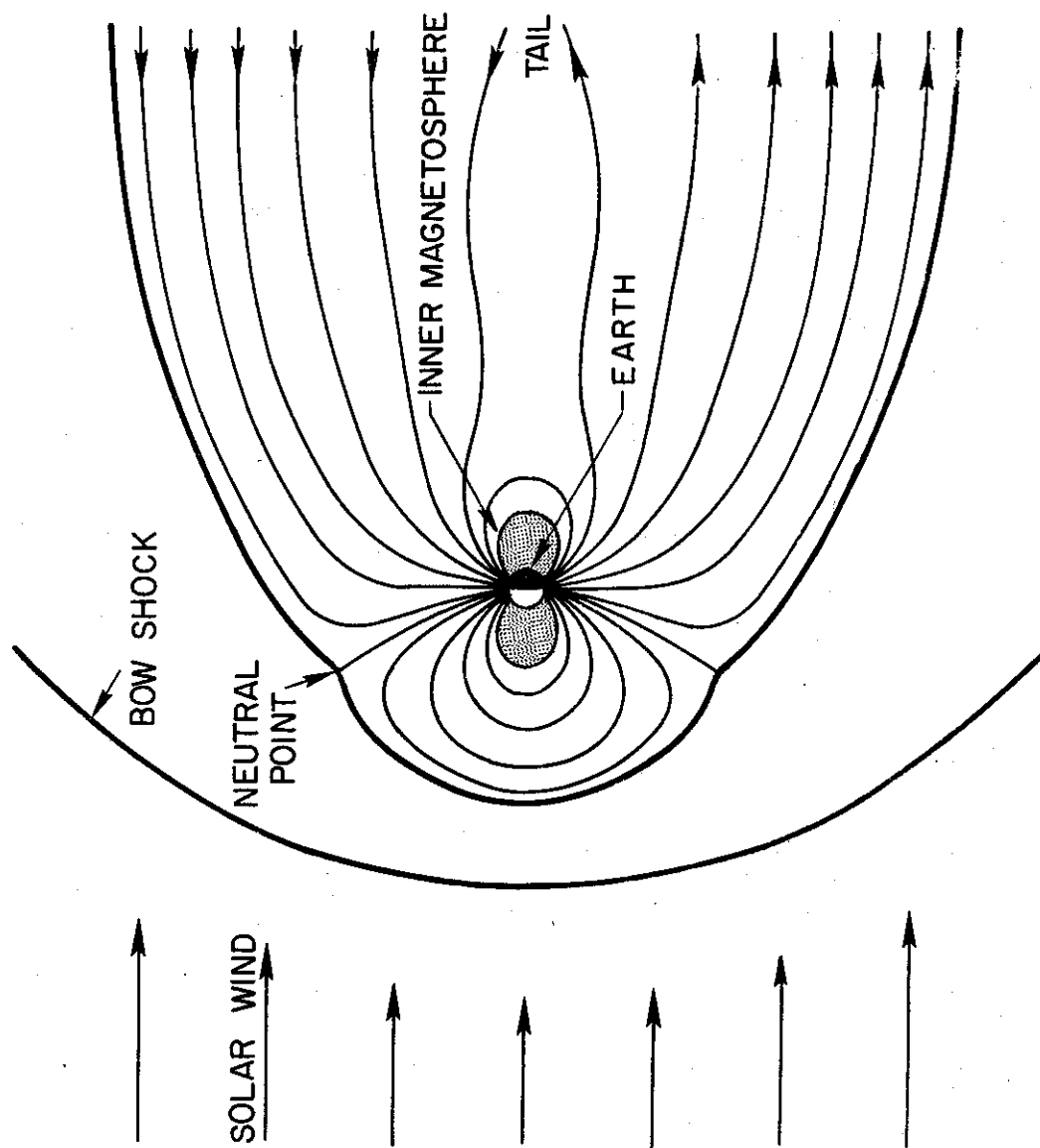


FIGURE 1.1 THE GENERAL OUTLINE OF THE MAGNETOSPHERE

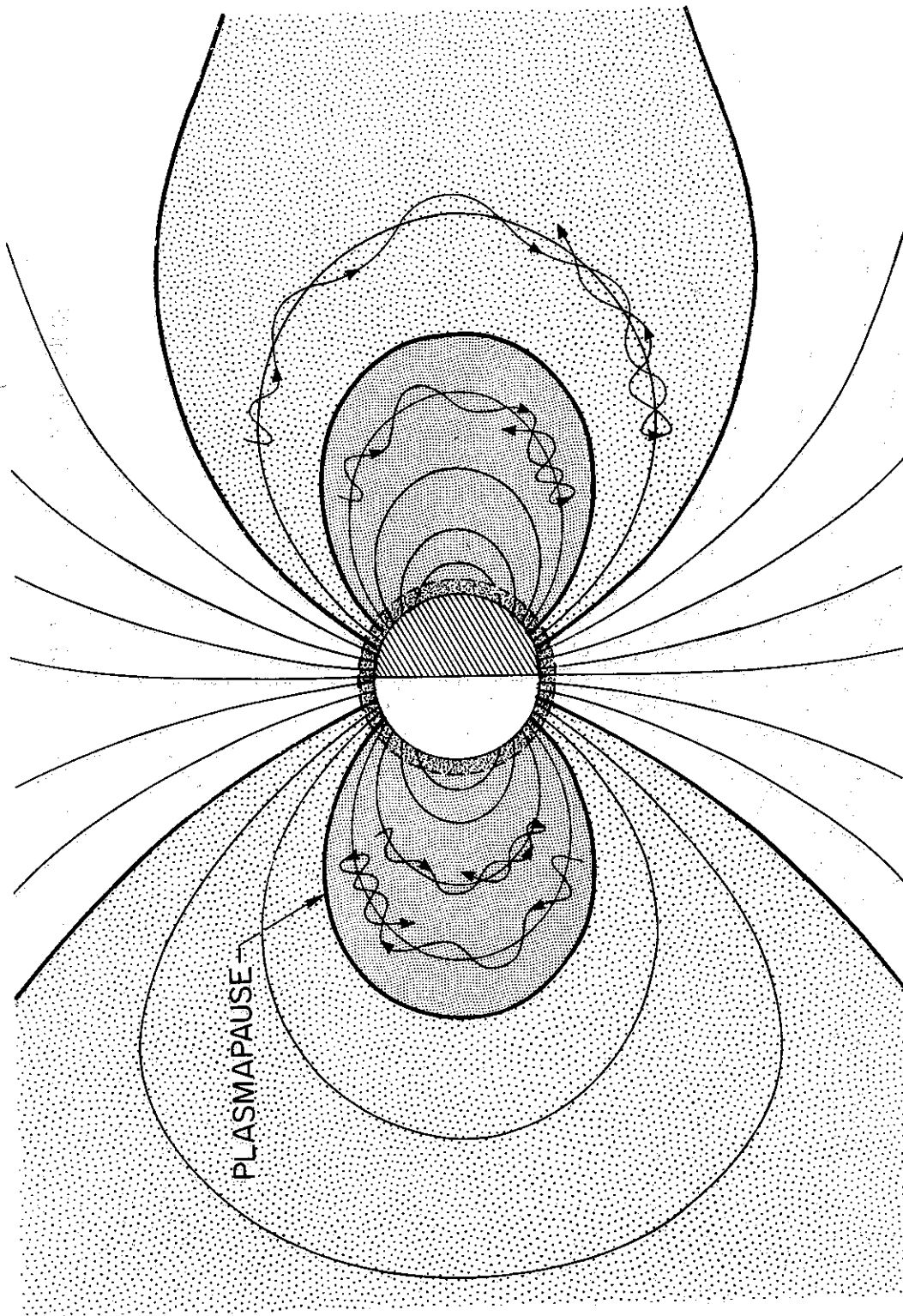


FIGURE 1.2 THE INNER MAGNETOSPHERE, DIPOLE FIELD LINES, PLASMAPAUSE AND AN ENERGETIC PARTICLE TRAJECTORY.

the earth's gravitational and centrifugal forces [Angerami and Thomas, 1964]. The cold plasma densities in the plasmasphere range from 10^4 particles/cc at 1000 km altitude to ~300-400 particles/cc at the inner edge of the plasmasphere.

In addition to the cold plasma, the inner magnetosphere is also populated by energetic (hot) particles which constitute the earth's radiation belts. These particles, mainly protons and electrons with energies from 10 keV up to 100 MeV, are magnetically trapped in the earth's field. They execute a helical gyro motion around the field lines and bounce back and forth between conjugate hemispheres. Typical energetic particle trajectories are shown in Fig. 1.2.

The study of the radiation belts has been increasingly important and relevant for almost all areas of magnetospheric physics in the last two decades [Hess, 1968; Roederer, 1970; Akasofu and Chapman, 1972].

Although the source and loss processes of these energetic particles are not fully understood, one possibility is that the particles of the solar wind enter the magnetosphere through the tail, are accelerated along the magnetic field lines and enter the plasmasphere at the sunward side after arriving there through the mechanism of cross-field drifts. In addition to being trapped along the field lines the energetic particles drift in the azimuthal direction due to both $\vec{E} \times \vec{B}$ and gradient $|\vec{B}|$ drifts.

An important loss process for the radiation belt particles is wave-particle interactions. The magnetosphere is extremely rich in the kinds of waves that it supports. As an excellent and unique example of a dense, 'infinite' magnetoplasma, it supports wave modes in a broad range

of frequencies from 1 Hz up to 100 MHz. Almost all of these modes exhibit fundamental wave properties like dispersion and anisotropy. Some of these modes (e.g., the whistler mode) can resonate with the energetic particles due to their low wave phase velocities [Brice, 1964]. During these wave-particle resonant interactions the waves are amplified or damped through various plasma instability mechanisms and the particles are scattered in energy and pitch angle, the latter being the angle of inclination of the particle velocity vector with respect to the magnetic field direction. As a result of these perturbations some particles are precipitated out of the radiation belts and into the atmosphere. These precipitated particles produce secondary ionization, emit x-rays and in general produce significant perturbations in the lower ionosphere.

Wave particle interactions can be roughly classified as being either incoherent or coherent. The former involves incoherent wide band electromagnetic waves such as ELF-VLF plasmaspheric hiss. In these interactions the forces exerted by the wave on the particle are uncorrelated and the particles execute a random walk in velocity space. Coherent interactions involve narrowband waves such as VLF signals from ground transmitters, natural whistlers, triggered emissions and signals induced by large scale power grids. During such coherent interactions the wave induced forces on the particle are cumulative in nature. The particles can therefore be phase locked with the coherent wave and execute well defined motions during which they suffer significant perturbations in energy and momentum. Much work over the past decade has been devoted to the study of incoherent wave particle interactions. Relatively little effort has been made to study coherent interactions.

The purpose of the research presented in this report is to determine the nature of particle precipitation caused by the cyclotron resonance interaction between a coherent whistler-mode signal and energetic particles in the 0.5 keV to 200 keV range. An important characteristic of the whistler mode is that $f < f_H$, where f is the wave frequency and f_H is the electron gyrofrequency. The wave polarization is elliptical in general and right-hand circular for the case of propagation along the static magnetic field, with the wave vectors rotating in the same sense as a gyrating electron for the propagating mode. Furthermore the wave phase velocity is of the order of $0.01c$ - $0.1c$. Therefore these 'slow' waves can achieve both longitudinal and cyclotron resonances with relatively low energy particles [Brice, 1964].

The cyclotron (or gyro) resonance interaction is an interaction in which the doppler-shifted wave frequency seen by the electrons is equal to the electron gyrofrequency. In that case the particles experience an approximately stationary wave field for an extended period of time; significant cumulative interactions can occur resulting in exchange of energy between the wave and the particles through the wave's electric field. The pitch angle, i.e. the direction of the particle velocity, also changes due to the transfer of the particle's parallel (along static magnetic field) momentum to perpendicular momentum (or vice-versa) under the influence of the wave's magnetic field. When the particle pitch angle is lowered below a value called the 'loss cone' pitch angle the particle reaches the atmosphere and is precipitated. It is this wave induced pitch angle scattering by coherent VLF whistler mode waves that is the subject of this report.

In the following we give a brief review of previous work done in the field of pitch angle scattering due to wave-particle interactions.

B. REVIEW OF PREVIOUS WORK

There has been considerable work done on the pitch angle scattering of radiation belt particles by electromagnetic waves [Dungey, 1963, 1964; Kennel and Engelmann, 1966; Kennel and Petschek, 1966; Roberts, 1966, 1968, 1969; Gendrin, 1968; Kennel, 1969; Lyons et al., 1971, 1972; Ashour-Abdalla, 1972; Schulz and Lanzerotti, 1973; Lyons, 1973, 1974a,b]. Most of this work, however, has addressed the problem of scattering by wideband, incoherent whistler mode turbulence. The idea has been that the trapped particle population interacts through cyclotron resonance with electromagnetic disturbances along its orbit and is subjected to a series of scatterings that are random in both direction and size. Hence the individual particles of the population undergo a random walk in pitch angle, and diffusion in equatorial pitch angle space results. This diffusion can then be studied by calculating the incoherent diffusion coefficients and solving a Fokker-Planck equation [Roberts, 1966].

This approach is well justified for studying the scattering due to interaction with certain kinds of magnetospheric signals, for example, auroral VLF hiss or ELF plasmaspheric hiss, since such waves are indeed wide band and highly incoherent [Muzzio, 1971; Gurnett and Frank, 1972; Thorne et al., 1973; Laaspere and Hoffman, 1976].

The physics in our case is fundamentally different because it involves highly coherent, narrowband whistler mode waves. When a particle population encounters such coherent waves, the series of scatterings experienced by the particles are not random in direction or size. The in-

dividual particles of the population can be phase locked with the coherent signal for distances of many hundred wavelengths and undergo large pitch angle changes in a single encounter with the wave. It is therefore incorrect to assume that the particles execute a random walk in pitch angle during the course of one bounce period when interacting with coherent waves.

The study of wave-particle interactions with coherent waves is very important. Examples of such highly coherent magnetospheric signals are natural whistlers [Helliwell, 1965], triggered VLF emissions [Stiles and Helliwell, 1975], signals that are injected into the magnetosphere by VLF ground transmitters [Helliwell and Katsufakis, 1974] and large scale power grids [Helliwell et al., 1975; Park, 1976] or signals from satellite borne VLF transmitters, such as that planned for the AMPS mission.

During the past three years VLF wave injection experiments have been carried out using the Stanford University variable frequency VLF transmitter at Siple Station in the Antarctic [Helliwell and Katsufakis, 1974]. The Siple wave injection experiment is an active experiment designed to study coherent VLF wave particle interactions in the magnetosphere. One goal of the experiment is to learn how to control the energetic particles by the injected waves.

Once control is established, the energetic particles can be used as tools to study other important processes. For example, the control of energetic particle precipitation would permit controlled studies of x-ray, ionization and radiation emission processes in the ionosphere. The generation and study of precipitation induced modifications in the D-region [Helliwell et al., 1973] would also be facilitated. Further-

more, modulation of precipitation flux might provide a means to produce Pc-1 ULF waves [Bell, 1976] on a controlled basis. Reducing the particle population in the radiation belts with appropriate transmissions is another possible future application. Although ground transmitters illuminate a relatively large region of the magnetosphere [Inan et al., 1977a], satellite transmitters may be necessary for applications requiring high wave amplitudes.

Theoretical studies of the coherent cyclotron resonance wave-particle interaction have concentrated on wave growth and generation due to the phase bunching of the energetic particles [Brice, 1964; Bell and Buneman, 1964; Helliwell, 1967, 1970; Dysthe, 1971; Nunn, 1971, 1974; Palmadesso and Schmidt, 1971, 1972; Matsumoto, 1972; Brinca, 1972; Bud'ko et al., 1972; Helliwell and Crystal, 1973; Karpman et al., 1974a,b].

Pitch angle scattering induced by coherent waves have been considered by only a few authors [Das, 1971; Ashour-Abdalla, 1972]. However a linear theory was employed in each of these studies. Although it is generally accepted that linear theory applies for small wave amplitudes, none of the authors who have used this theory has given quantitative justification for the assumptions. The main advantage of the theory is that it considerably simplifies the analysis.

C. OUTLINE OF THE REPORT

This report describes a computer simulation approach to the study of the cyclotron resonance wave particle interaction between coherent VLF whistler mode signals and energetic electrons in the magnetosphere. In particular, we consider the wave-induced pitch angle scattering of the particles. One important result of this scattering is precipitation

of particles into the atmosphere.

We have employed a Lagrangian formulation involving a test particle simulation of the nonlinear equations of motion. In this approach, the effect of a wave signal on a particle population is calculated by simulating the interaction for a sufficient number of test particles. Although the purpose of this simulation is to compute the wave's effect on the particles, our results are also directly applicable to the problem of wave growth and generation through phase bunching [Helliwell, 1967; 1970], since we compute the full phase motion of all test particles in order to obtain the total scattering.

Since we use a test particle approach, our calculations do not include the effects of the electromagnetic fields generated by the perturbed energetic particles. In effect we assume that the currents stimulated in the energetic particle population do not lead to significant damping or amplification of the wave near the magnetic equatorial plane. Experimental results indicate that this assumption holds true a good deal of the time in the magnetosphere. A discussion of this point is included in Chapter 6.

In this report we have considered only the case of a monochromatic whistler mode signal. However the computer program is quite general and is capable of dealing with the case of single pulses or a train of pulses. The case of a single frequency is not as limited as it might seem, since there is some reason to believe that the interaction with a wave with linearly increasing or decreasing frequency is quantitatively not much different [Helliwell, 1970]. We also limit ourselves to wave propagation strictly along the static magnetic field lines with k parallel to \bar{B}_0 .

We assume that the wave is not affected by the energetic particles and has a uniform amplitude over the field line near the equatorial plane. The energetic particles also do not interact with each other. This assumption allows the computation of the particle trajectories sequentially instead of in parallel.

The computer simulation is versatile and can be used for a variety of magnetospheric conditions. In this report we give results for a 5 kHz wave signal propagating along the dipole field line which has an equatorial geocentric distance of about 4 earth radii.

The organization of the report is as follows. Chapter 2 provides the basic physics and derives the equations of motion. The trapped particles and the coherent VLF waves that exist in the magnetosphere and the principles of the gyroresonant interaction through which these two affect each other are described there.

In Chapter 3 we describe the computer simulation of the interaction. The computer program is given in an Appendix.

Chapter 4 treats the nonlinear trajectories of single resonant particles and sheets of resonant particles distributed in cyclotron phase. The purposes of this chapter are (i) to understand the physics of the interaction and the dependence of total scattering on different wave, medium and particle parameters, and (ii) to define the limitations of linear theory.

In Chapter 5 we give an application of the simulation to a sample computation of the precipitated flux using a full distribution of particles. We present the results in units that are comparable with measurements.

In the last chapter, conclusions, discussion and suggestions for future work are given.

D. CONTRIBUTIONS OF THE PRESENT WORK

1) We have for the first time computed the precipitated fluxes due to interaction of a full distribution of energetic particles and coherent VLF waves. Our results show that significant energy fluxes (10^{-1} ergs/cm²-sec) can be deposited by moderate intensity (~ 10 mV) coherent waves. These fluxes produce significant perturbations in the lower ionosphere. Both the incoming fluxes and the perturbations produced by them are well within the resolution of current instruments.

2) Our results show that nonlinear effects are significant for wave amplitudes as low as 3 mV. We have also formulated a convenient quantitative criterion for determining the applicability of linear theory under given conditions.

3) The complete nonlinear equations of motion for particles that cyclotron resonate with a whistler-mode wave in an inhomogeneous magnetosphere are simulated on a computer. It is shown that the inhomogeneity of the medium can be incorporated with little additional computer time, by employing spatial instead of temporal steps in the simulation.

4) The straightforward computer simulation of the wave particle interaction has led to a clear presentation of several different aspects of the physics of the interaction such as wave trapping and relative effects of the wave and inhomogeneity forces. We have shown the dependence of the particle perturbations on a number of wave, medium and particle parameters.

5) Our work has provided a basis for future studies which may be undertaken with relatively minor modifications of the present computer simulation. Some of these are described in a section of Chapter 6 on "suggestions for future work."

II. BASIC PHYSICS AND EQUATIONS OF MOTION

A. THE MODEL MAGNETOSPHERE

The earth's magnetic field in the inner magnetosphere can be closely approximated by a centered dipole inclined with respect to the rotation axis by about 11° . The magnetic field strength in that case is given by

$$B_0 = 0.312 \times 10^{-4} \left(\frac{R_0}{R} \right)^3 (1 + 3 \sin^2 \lambda)^{1/2} \frac{\omega b}{m^2} \quad (2.1)$$

where λ is the geomagnetic latitude, R is the geocentric distance and R_0 is the mean radius of the earth, 6370 km. Figure 2.1 illustrates the dipole geometry and the symbols used.

A dipole field line is described by the relation

$$\frac{R}{\cos^2 \lambda} = \frac{R_0}{\cos^2 \lambda_0} \quad (2.2)$$

$$\psi = \psi_0$$

where the subscript "o" refers to the earth's surface and ψ is the geomagnetic longitude. The field lines in any meridional plane can be uniquely identified by a parameter L defined as

$$L = \frac{R_{eq}}{R_0} = \frac{1}{\cos^2 \lambda_0} \quad (2.3)$$

where R_{eq} is the geocentric distance of the field line at the equator. For example the $L = 4$ field line crosses the geomagnetic equator at a geocentric distance of 4 earth radii and enters the earth at geomagnetic

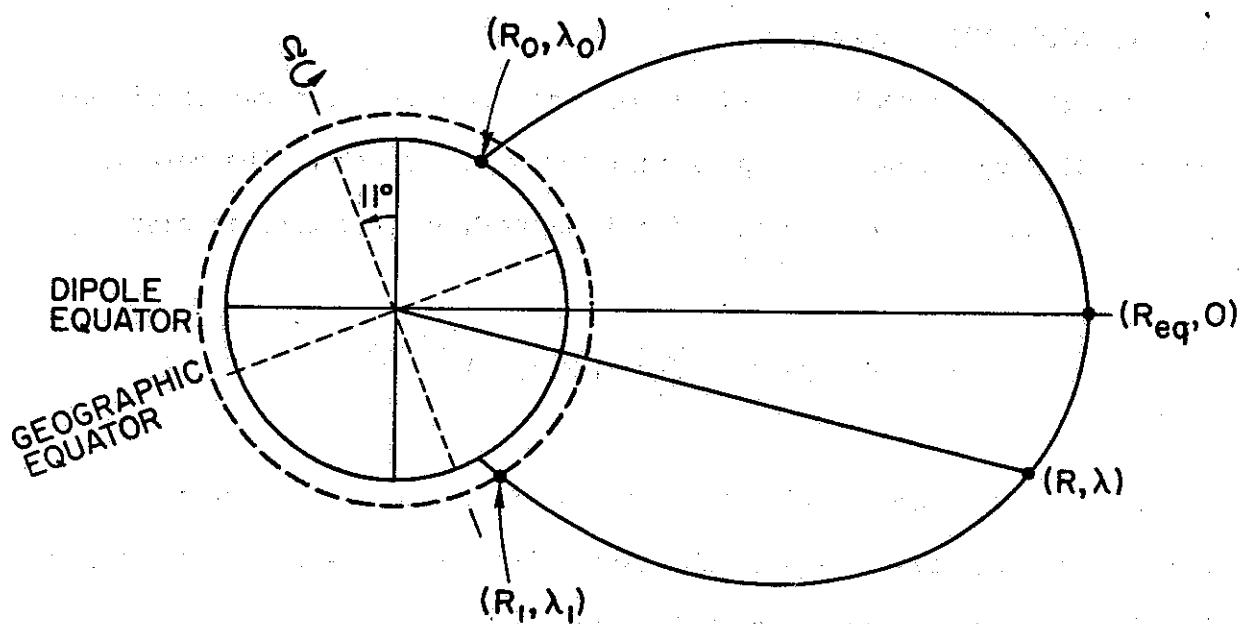


FIGURE 2.1 COORDINATE SYSTEM AND SYMBOLS FOR THE DIPOLE GEOMETRY AND THE DIFFUSIVE EQUILIBRIUM MODEL.

latitudes $\pm 60^\circ$.

The cold plasma in the inner magnetosphere can be approximated by a diffusive equilibrium model in which the neutral isothermal mixture of electrons and positive ions (H^+ , He^+ and O^+) is in diffusive equilibrium along the magnetic field lines, under the influence of the earth's gravitational and centrifugal forces [Angerami and Thomas, 1964]. The electron density in this case is given by [Park, 1972]

$$\begin{aligned}
n_e &= n_1 \left[\sum_i c_i \exp \left(-\frac{z_G}{H_i} \right) \right]^{1/2} \\
z_G &= R_1 - \frac{R_1^2}{R} - \frac{\Omega}{2g_1} (R^2 \cos^2 \lambda - R_1^2 \cos^2 \lambda_1) \\
H_i &= \frac{k_b T_p}{m_i g_1}
\end{aligned} \tag{2.4}$$

where c_i is the fractional abundance of the ionic species, n is electron density, R is the geocentric distance, Ω is the angular speed of rotation of the earth, g is the acceleration of gravity, θ is the dipole latitude, k_b is the Boltzmann's constant, m is the mass and T_p is the plasma temperature. The subscript i refers to the i th ionic species and the subscript 1 refers to the reference level of the diffusive equilibrium model at 1000 km altitude. The coordinates and symbols used are shown in Fig. 2.1. The geopotential height z_G takes into account the variations of gravitational force with distance and the centrifugal force due to corotation of the plasma with the earth. The diffusive equilibrium model is inaccurate at high latitudes and particularly outside the plasmasphere.

The 'cold' magnetospheric plasma consists of particles with less than a few electron volts energy. The electrons have gyroradii (radius of gyration around the magnetic field) of a few meters. Mixed with the cold plasma are energetic (hot) particles, electrons and positive ions that populate the radiation belts. These particles have energies extending up to hundreds of MeV with electron gyroradii of hundreds of meters. They execute rapid motions along the field lines and stay trapped in the radiation belts due to the inhomogeneity of the earth's magnetic field. The motion of these high energy particles is almost completely

controlled by the magnetic field. The effect of gravitational and centrifugal forces can be ignored. In the next section we study the motion of the energetic particles trapped in the earth's radiation belts.

B. DYNAMICS OF RADIATION BELT PARTICLES

Charge motion in a static magnetic field:

A charged particle moving in the presence of a magnetic field follows a helical path as a result of its motion parallel to the field superimposed on its gyration in the plane perpendicular to the magnetic field, as shown in Fig. 2.2. The components of the particle velocity parallel and perpendicular to the field direction are denoted by v_{\parallel} and v_{\perp} respectively. The gyrofrequency ω_H and the gyroradius r_H (radius of gyration around the center line) and the gyroperiod T_H are given by

$$\omega_H = \frac{qB_0}{m}; \quad T_H = \frac{2\pi}{\omega_H} \quad (2.5)$$

$$r_H = \frac{mv_{\perp}}{qB_0} = \frac{mv \sin \alpha}{qB_0}$$

where $\alpha = \tan^{-1} \frac{v_{\perp}}{v_{\parallel}}$ is the particle's pitch angle. Electrons and protons gyrate in opposite directions as shown in Fig. 2.2.

A static magnetic field cannot do work on the particle since the force on the particle ($\vec{v} \times \vec{B}_0$) is perpendicular to the direction of motion. The magnetic field can, however, change the direction of particle velocity and therefore the direction of momentum. The total kinetic energy of the particle, given by $1/2 mv^2$, is conserved along its trajectory. Therefore, in a spatially changing magnetic field, such as the earth's

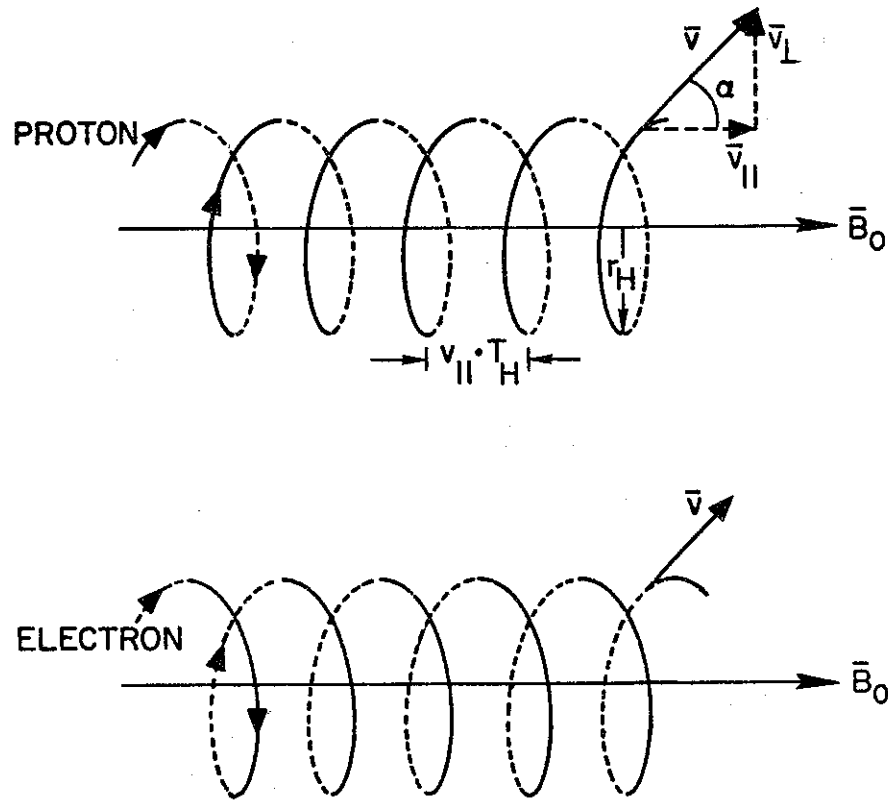


FIGURE 2.2 PARTICLE MOTION IN A HOMOGENEOUS STATIC MAGNETIC FIELD.

field, the particle orbit (characterized by ω_H and r_H) must change in such a way as to conserve total kinetic energy. The fact that the static magnetic field does no work on the particle means that the magnetic flux linking the orbit of a particle gyrating about a field line (while at the same time moving along the line) is constant. Otherwise in the frame of reference which follows the parallel motion, $\frac{\partial B_0}{\partial t} \neq 0$ and the electric field produced (through $\nabla \times \vec{E} = -\frac{\partial \vec{B}_0}{\partial t}$) would accelerate the particles, causing a change in energy. Hence,

$$\text{Flux} = B_0 r_H^2 = \text{constant} \quad (2.6)$$

Substituting the expression for r_H we obtain

$$\text{Flux} = B_0 \left(\frac{mv \sin \alpha}{qB_0} \right)^2 = \text{constant}$$

since $v = \text{constant}$ (conservation of energy) we have

$$\frac{\sin^2 \alpha}{B_0} = \text{constant} \quad (2.7)$$

Hence as the magnetic field changes along the particle trajectory, the pitch angle must change in accordance with (2.7). Note that we have presented an approximate and heuristic derivation of (2.7). For a precise and rigorous derivation the reader is referred to Northrop [1963] or Buneman [1973]. In order for (2.7) to apply the condition

$$\left(\frac{T_H v_H}{B_0} \right) \frac{dB_0}{dz} \ll 1 \quad (2.8)$$

where z is the distance along the field line, must hold. In other words the particle must go through many gyrations in a distance over which the magnetic field changes appreciably. This approximation is called the 'adiabatic approximation' and the quantity $\mu = \frac{v^2}{B_0}$ is called the first adiabatic invariant. The condition (2.8) is well satisfied for all inner magnetospheric conditions. According to (2.7), as B_0 increases along the trajectory the particle pitch angle also increases. At the point where $\alpha = 90^\circ$, the particle must turn around or 'mirror,' since v_{\parallel} has been reduced to zero.

In the earth's dipole field as defined by (2.1), it is convenient to relate the mirror point to the equatorial parameters. The value of

the static magnetic field at the mirror point ($\alpha = 90^\circ$) is given by

$$B_m = \frac{B_{eq}}{\sin^2 \alpha_{eq}} \quad (2.9)$$

where B_{eq} , α_{eq} are the magnetic field and the pitch angle at the equator, respectively.

Figure 2.3 shows a portion of the trajectory of a typical particle in a dipole field. Since the dipole field is symmetrical about the magnetic equator the particles mirror at 'conjugate' points as the bounce back and forth between hemispheres.

Bounce period:

The time it takes the particle to travel from one mirror point to another is $\tau_B/2$, where τ_B is called the 'bounce period.' Note that for a given dipole field line (specified by its L value as defined in (2.3)), the location of the mirror point is independent of particle energy and is uniquely determined by α_{eq} , through (2.9). The bounce period τ_B however depends on both v (i.e. energy) and α_{eq} , and is given by

$$\tau_B = 2 \int_{z_m}^{z'_m} \frac{dz}{v_{||}(z)} \quad (2.10)$$

where z is the distance along the field line. We have, at any point,

$$v_{||}(z) = v \cos \alpha(z) = v [1 - \sin^2 \alpha(z)]^{1/2} = v \left[1 - \frac{B(z)}{B_{eq}} \sin^2 \alpha_{eq} \right]^{1/2} \quad (2.11)$$

where v is the total particle velocity. In the last part of the above we have used (2.7). Now using (2.9) we obtain

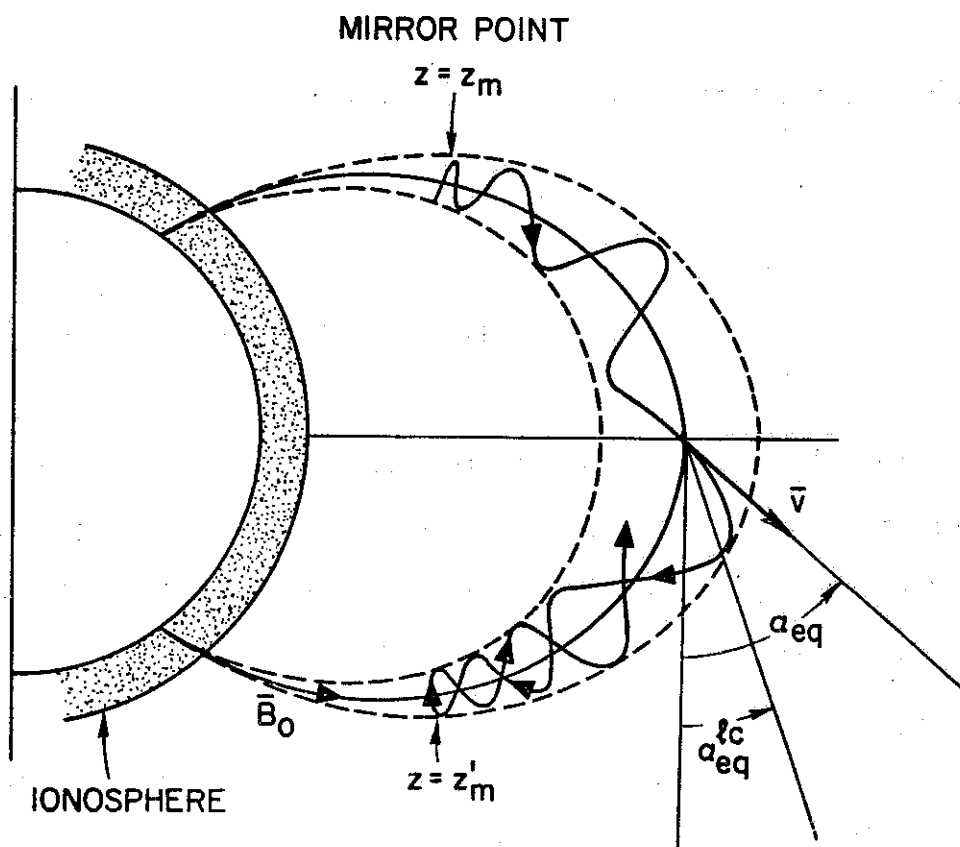


FIGURE 2.3 THE TRAJECTORY OF AN ENERGETIC PARTICLE TRAPPED IN THE EARTH'S FIELD.

$$v_{\parallel}(z) = v \left[1 - \frac{B(z)}{B_m} \right]^{1/2} \quad (2.12)$$

substituting in (2.10), we obtain

$$\tau_B = \frac{2}{v} \int_{z_m}^{z'_m} \frac{dz}{\left[1 - \frac{B(z)}{B_m} \right]^{1/2}} \quad (2.13)$$

This integral can be expressed as [Liemohn, 1961; Hess, 1968; Roederer, 1970]:

$$\tau_B = \frac{4R_0 L}{v} \int_0^{\lambda_m(\alpha_{eq})} \frac{\cos \lambda [1+3\sin^2 \lambda]^{1/2} d\lambda}{\left\{ 1 - \frac{\sin^2 \alpha_{eq} [1+3\sin^2 \lambda]^{1/2}}{\cos^6 \lambda} \right\}^{1/2}} = \frac{4R_0 L}{v} f(\alpha_{eq}) \quad (2.14)$$

where λ is the latitude. Equation (2.14) can be obtained from (2.13) using the dipole geometry and (2.7) and (2.9). The integrand $f(\alpha_{eq})$ has an integrable square root singularity at $\lambda = \lambda(\alpha_{eq})$ and has been evaluated numerically [Liemohn, 1961]. Its value varies from 0.75 for $\alpha_{eq} = 90^\circ$ to 1.4 for $\alpha_{eq} = 0^\circ$. A good approximation for $40^\circ \leq \alpha_{eq} < 90^\circ$ is

$$f(\alpha_{eq}) \approx 1.30 - 0.56 \sin \alpha_{eq} \quad (2.15)$$

The bounce periods for the radiation belt particles range from one tenth of a second to a few seconds. The gyroperiods of these particles are of the order of 10^{-5} to 10^{-3} seconds. Hence the cyclotron (gyro) and bounce motions of these particles have widely different periods and are almost completely separable. This is the basis of the 'adiabatic approximation' the result of which is the expression (2.7).

Particle precipitation and the loss cone:

As mentioned above, the particle's mirror point is uniquely determined by α_{eq} . If the mirror point is lowered to atmospheric altitudes (below ~200 km) the particle may collide with the atmospheric neutral constituents and be absorbed. In that case the particle does not bounce back along the field line and is described as being 'precipitated' out of the radiation belts.

At the equator, one can define a minimum value α_{eq}^{lc} such that for $\alpha_{eq} < \alpha_{eq}^{lc}$ the particle mirror point would be below some height h_m

where it will very likely be absorbed by the atmosphere. The pitch angle α_{eq}^{1c} is called the equatorial 'loss cone' pitch angle and h_m is called the lowest mirror height. Defining a normalized lowest mirror geocentric radius as

$$\xi_m = \frac{R_o + h_m}{R_o} \quad (2.16)$$

and using the dipole relations (2.1) through (2.3) and (2.9) we obtain

$$\sin(\alpha_{eq}^{1c}) = \left[\frac{\xi_m^3}{L^2 \sqrt{4L^2 - 3\xi_m L}} \right]^{1/2} \quad (2.17)$$

It is clear that α_{eq}^{1c} depends strongly on the particular field line of concern as indicated by the L-value dependence in (2.17). The equatorial loss cone angle as a function of L value for $h_m = 100$ km and $h_m = 0$ is given below.

L	2	3	4	5	
$\alpha_{eq}^{1c}(\text{deg})$	16.77°	8.62°	5.47°	3.87°	$h_m = 100$ km
	16.33°	8.41°	5.34°	3.78°	$h_m = 0$

As seen above the loss cone angle does not strongly depend on h_m .

In the absence of forces which may alter the equatorial pitch angle the particle will remain trapped in the magnetic field until its azimuthal cross field motion causes it to drift across the field lines toward the sunlit side of the magnetosphere where some particles can become detrapped because of the solar wind induced distortion of the field lines. The cross field drift motion is briefly explained below. This motion is much slower than the bounce motion of the particles. Typical

lifetimes for trapped particles range from an hour to a few days, while some particles may be stably trapped [Roederer, 1970]. Even without any cross-field drifts, a particle's α_{eq} may be altered by wave-particle interactions,* sometimes causing the particle to precipitate. Precipitation induced by wave particle interactions is one of the major loss processes for the radiation belt particles. This report describes precipitation due to one such wave particle interaction, namely the cyclotron resonant interaction involving coherent whistler mode waves.

Drift across field lines.

In addition to the gyro and bounce motions the energetic particles execute azimuthal and radial drift motions across the field lines. This is depicted in Fig. 2.4 which shows a geomagnetic equatorial cross section of the earth and the inner magnetosphere.

The important kinds of azimuthal drifts are the gradient-curvature and the $\bar{E} \times \bar{B}$ drifts. The gradient-curvature drift is caused by the inhomogeneity of the magnetic field and the curvature of the field lines. In the earth's dipole field this drift is eastward for electrons and westward for protons. The drift periods at $L = 4$ range from ~5 days for 10 keV electrons to ~15 minutes for 1 MeV electrons. The proton drift periods are smaller than those for the electron but not by more than a factor of 2. The $\bar{E} \times \bar{B}$ drift is caused by radial electric fields. This drift is in the same direction for both electrons and protons.

* In a wave particle interaction α_{eq} is modified either because of transfer of energy to (or from) the wave through the wave's electric field, which may change $v_{||}$ or v_{\perp} or because the wave's magnetic field changes the direction of momentum of the particle without much energy transfer.

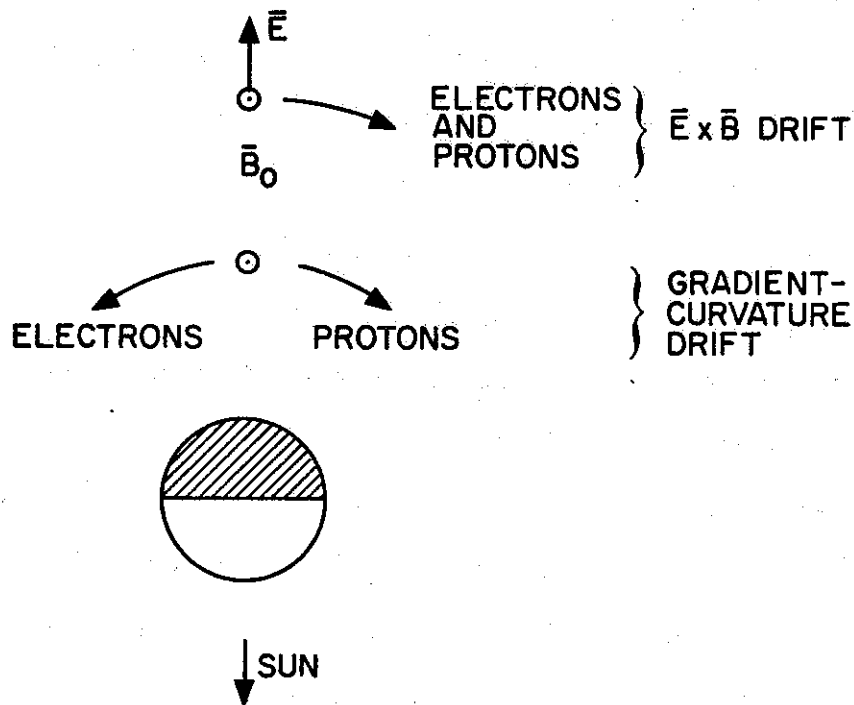


FIGURE 2.4 CROSS FIELD DRIFTS.

Radial drifts are mainly $\bar{E} \times \bar{B}$ drifts caused by azimuthal electric fields [Carpenter and Seely, 1976]. The drift could be inward or outward depending on the direction of the electric field. Usually radial drifts are slower than azimuthal drifts.

For a more detailed discussion of cross field drifts, the reader is referred to Hess [1968] and Roederer [1970].

C. COHERENT VLF WHISTLER MODE WAVES IN THE MAGNETOSPHERE

The Whistler Mode of Propagation:

This report deals with the cyclotron resonance interaction between energetic radiation belt particles and very low frequency waves which propagate through the magnetospheric plasma in what is commonly known as the "whistler mode." This mode has been discussed in detail by a number of workers [Storey, 1953; Helliwell, 1965]. The plane-wave dispersion relation which describes the mode has been known for many years, having originally been published by Appleton [1927], who in his paper generalized some earlier work on the same topic by Lorentz [1909].

This mode can be identified in the following way. In a cold, collisionless, homogeneous, infinite plasma immersed in a homogeneous static magnetic field, \vec{B}_0 , two characteristic electromagnetic waves exist at frequencies below the electron gyrofrequency. In general these characteristic waves are elliptically polarized, the sense of rotation of the wave magnetic vector of one wave being the same as, and the other wave being opposite to, the sense of rotation of the electrons about the static magnetic field lines. The dispersion relation and the polarization for these waves are given by [Ratcliffe, 1959; Budden, 1961; Stix, 1962].

$$n^2 = 1 - \frac{(f_p^2/f^2)}{1 + \frac{f_H^2 \sin^2 \theta}{2(f_p^2 - f^2)} \mp \left[\left(\frac{f_H^2 \sin^2 \theta}{2(f_p^2 - f^2)} \right)^2 + \frac{f_H^2}{f^2} \cos^2 \theta \right]^{1/2}} \quad (2.18)$$

$$\delta = i \left(\frac{f_H}{f} \cos \theta \right)^{-1} \left\{ \pm \left[\frac{f_H^2}{f^2} \cos^2 \theta + \left(\frac{f_H^2 \sin^2 \theta}{2(f_p^2 - f^2)} \right)^2 \right]^{1/2} - \frac{f_H^2 \sin^2 \theta}{2(f_p^2 - f^2)} \right\} \quad (2.19)$$

where $n = \frac{kc}{\omega}$ is the refractive index, k being the wave number, δ is the wave polarization, θ is the angle between the wave normal and the magnetic field B_0 , f is the wave frequency, f_H is the electron gyrofrequency, $f_p = \frac{1}{2\pi} \sqrt{\frac{n_e e^2}{m \epsilon_0}}$ is the electron plasma frequency with n_e being the cold plasma density and ϵ_0 being the permittivity of free space and $i = \sqrt{-1}$.

In the above equations the choice of the upper sign preceding the radical describes the dispersion of the characteristic wave whose rotational sense is the same as that of the electrons about the field lines, while the choice of the lower sign describes the dispersion of the characteristic wave whose rotational sense is the opposite to that of the electrons.

It is possible to demonstrate that when the square of the plasma frequency is larger than the product of the wave frequency and the sum of the wave and gyrofrequencies, i.e.

$$f_p^2 > f(f_H + f) \quad (2.20)$$

then the characteristic wave whose rotation is in the opposite sense to that of the gyrating electrons is nonpropagating. In the earth's magnetosphere for $f < f_H$ the condition (2.20) holds in general and the only propagating wave is one whose sense of rotation is the same as that of the electrons. Under these conditions that characteristic wave is

called the 'whistler mode', the dispersive aspects of which are described by (2.18) with the choice of the upper sign before the radical.

It can be shown that due to condition (2.20), the whistler-mode waves have phase and group velocities that are always less than the velocity of light in vacuum. This is a very important property since it means that such waves can achieve cyclotron or longitudinal resonances with the energetic particles. From (2.18) it can be seen that the phase velocity $[v_p = \frac{\omega}{k}]$, where $k = \frac{n\omega}{c}$ varies with the direction in the plasma indicated by θ ; thus the presence of a static magnetic field causes the medium to be anisotropic. Also the phase velocity (and the group velocity, $v_g = \frac{d\omega}{dk}$) depends on the wave frequency ω as well as the wave normal k . This means that waves of different frequencies travel with different velocities, i.e. the medium is dispersive.

Equation (2.18) is derived for a homogeneous medium. The magnetosphere is an inhomogeneous medium since both f_p and f_H vary in space. However the refractive index generally changes only a small amount in the space of one wavelength. A characteristic wave launched into such a medium exhibits characteristics at a given point that are approximately the same as those of a wave traveling in a homogeneous medium having the same refractive index. A medium having this property is called 'slowly varying'. The corresponding propagation analysis is called 'ray' theory, and the wave functions are called the W.K.B. solutions [Budden, 1961]. Such a slowly varying medium is analogous to a tapered transmission line or waveguide. In order to follow the 'phase path' and 'group path' of a signal propagating in the magnetosphere one needs to use ray tracing.

Equation (2.18) was originally derived for the extremely idealized case of a cold, infinite, collisionless, homogeneous plasma. It is a tribute to the magneto-ionic theory that this equation, together with the W.K.B. solution, has been found to describe quite well the propagation and dispersion of whistlers in the magnetosphere.

Whistlers and Other Coherent VLF Waves

Whistlers are a class of naturally occurring narrow band, audio-frequency electromagnetic radiations. They occur in the frequency range 300 Hz to 30 kHz and are readily detectable at middle and high latitudes by means of an audio amplifier attached to an antenna. These signals are characterized by distinctive variations of frequency with time which will generate at the amplifier a whistling sound, hence the name 'whistler'.

Whistlers result from the dispersion of impulse radiation from lightning strokes in one hemisphere which penetrate the lower ionosphere and travel through the magnetosphere along the earth's magnetic field lines. For frequencies higher than the proton gyrofrequency the dispersion of the original impulsive signal is governed to first order by (2.18) and the impulse is slowly transformed along the path into a smoothly descending (and/or rising) tone, i.e. a whistler, which is received in the conjugate hemisphere.

A portion of the energy of the lightning stroke which causes the whistler may travel in the earth-ionosphere wave guide to the receiver in the conjugate hemisphere. This energy is registered as an impulsive signal and is called the causative atmospheric or 'spheric'.

The frequency-time spectrum of a typical whistler event is shown in the top panel of Fig. 2.5. The time origin of the causative spheric is also shown. The spherics are seen as vertical lines while the several traces of the whistler are seen as quasi-parabolic curves. All traces originate from the same spheric. Three of the traces are sketched in the middle panel. The different traces have propagated on different paths as shown in the bottom panel. Each trace in itself is a narrow-band signal of smoothly changing frequency. Natural whistlers are widely used as a diagnostic tool of the magnetosphere. The frequency of minimum time delay, f_n , gives the L value of the path, while, the minimum time delay itself, t_n is a measure of the equatorial cold plasma density [Helliwell, 1965].

The observed dispersion of natural whistlers was found to agree closely with that predicted by using (2.18) along with the W.K.B. approximation [Helliwell, 1965]. This provides strong evidence that the dispersion characteristics of whistler mode waves in the magnetosphere is largely determined by the cold plasma. The energetic plasma can at times cause the waves to be amplified or damped through various instability mechanisms, but their overall effect on the propagation characteristics is negligible.

Whistlers propagate along field-aligned density enhancements in the magnetosphere. These density enhancements are called 'ducts'. The propagation in the ducts is called the 'ducted' mode. The theory of ducted propagation is well developed [Helliwell, 1965]. The presence of the density enhancement provides a variable refractive index in the transverse direction which confines the wave normal to small angles with re-

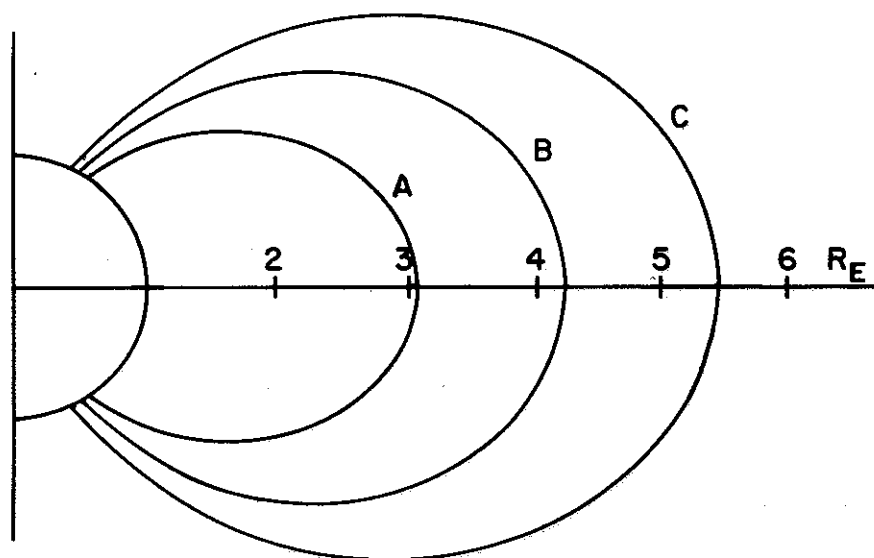
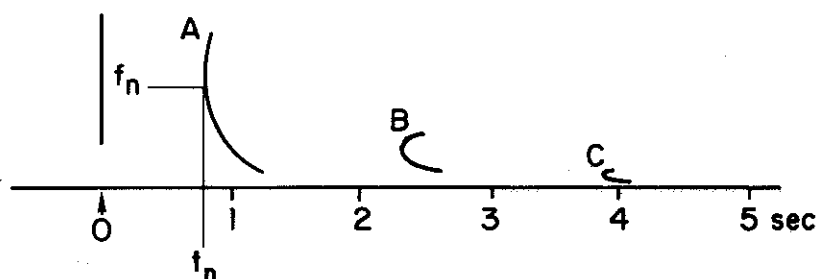
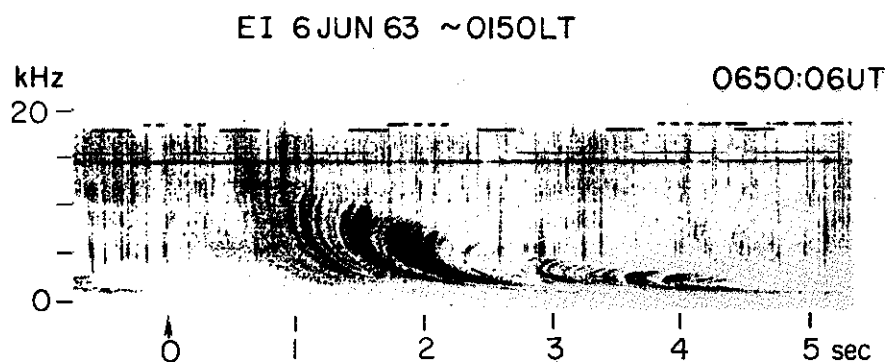


FIGURE 2.5 A TYPICAL WHISTLER EVENT. This event was observed at Eights (EI), Antarctica, on 6 June 1963 at 0150 Local Time (LT). This time corresponds to 0650:06 Universal Time (UT). The top panel shows the frequency time spectrogram. The middle panel is a sketch of the 'spheric' and three of the many individual traces of the whistler. The lower panel shows the magnetospheric paths traveled by the three traces [Park, 1972].

spect to the static magnetic field. As a result the wave energy is trapped in the duct much like light waves trapped in an optical fiber. Since their wave normal stays close to the magnetic field, ducted waves can penetrate the lower ionospheric boundary and be observed on the ground. For this reason these waves can be studied using receivers or transmitters on the ground. Many passive and active experiments of this kind have been carried out with successive results in the last two decades [Helliwell, 1965; Helliwell and Katsufrakis, 1974; Park and Carpenter, 1977; Park et al., 1977].

Ducts occupy only a small fraction of the inner magnetosphere. Most magnetospheric signals propagate in the 'non-ducted' mode. Nonducted waves do not generally propagate along the static magnetic field, and are not generally received on the ground. They have been seen on various satellites and their study has helped formulate propagation theories in plasmas. Nonducted waves with frequencies below 3 kHz are greatly affected by the presence of various ions in the ionosphere and the magnetosphere. Their dispersion is not simply described by (2.18). The refractive index diagrams are much more complicated, with two possible modes of propagation when the wave frequency lies below the proton gyrofrequency. The study of nonducted VLF and ELF waves on numerous satellites has verified the many cutoffs, resonances and cross overs predicted by the multiple-ion plasma wave propagation theory [Smith and Brice, 1964].

Both ducted and nonducted propagation have been extensively studied using ray tracing. A VLF ray tracing program incorporating multiple-ion plasma wave propagation theory has been developed over the years at

Stanford University [Walter, 1969; Burtis, 1974] and has been successfully used to explain many observed magnetospheric phenomena [Kimura, 1966; Smith and Angerami, 1968; Scarabucci, 1969; Walter, 1969; Angerami, 1970; Edgar, 1972; Inan et al., 1977b]. One recent application of ray tracing showed that the large density gradients of the plasmapause (see Fig. 1.2) can guide VLF waves in a manner very similar to normal ducting [Inan and Bell, 1977].

The success in the last two decades of the passive studies of the natural whistler events has led to active probing of the magnetosphere involving VLF wave-injection experiments using ground transmitters such as that at Siple Station, Antarctica [Helliwell and Katsufrakis, 1974]. This experiment involves a 100 kW VLF transmitter at Siple and a VLF receiver at the conjugate point in Roberval, Canada. In Figs. 2.6, 2.7, and 2.8 we show coherent VLF waves injected into the magnetosphere by the Siple VLF transmitter. Detailed explanations are given in the figure captions. Note that these signals are all coherent narrow-band signals with bandwidths less than ~50 Hz.

Another source of coherent VLF waves in the magnetosphere is the harmonic radiation from large scale power grids [Helliwell et al., 1975; Park, 1976]. These signals propagate in the magnetosphere and are received at the conjugate point. Figure 2.9 shows an example of these signals.

In addition to the examples of coherent VLF waves just discussed, the magnetosphere contains various kinds of 'incoherent' noise, usually called hiss because of the hissing sound they generate when applied to an audio amplifier. Figure 2.10 shows an observation on the OGO-4 satel-

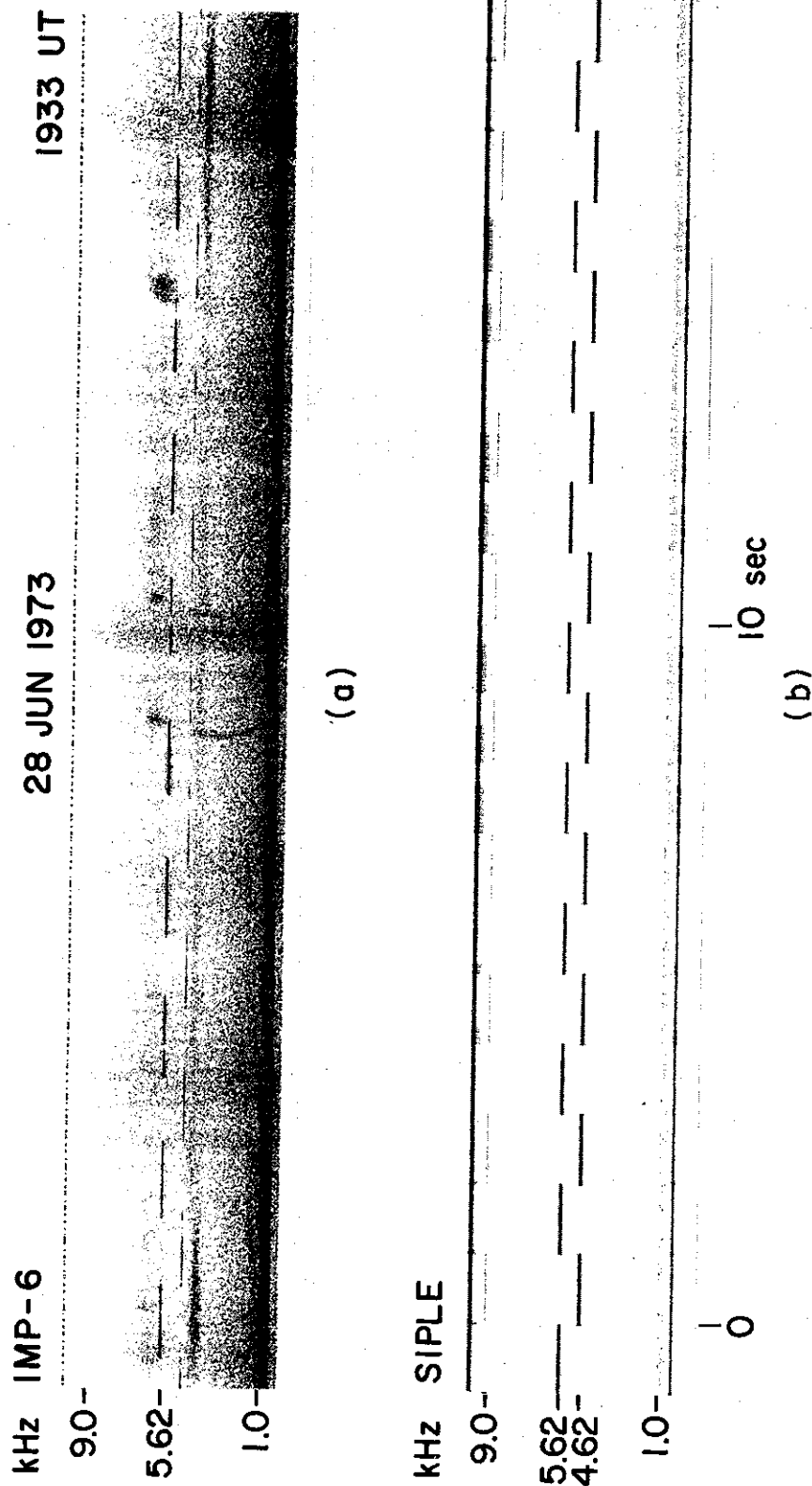


FIGURE 2.6 OBSERVATIONS OF TRANSMITTER SIGNALS ON THE IMP-6 SATELLITE [Inan et al., 1977a]. The bottom panel shows the format of transmissions as they are recorded at the transmitter site at Siple, Antarctica. The format in this case is frequency shift keying (FSK) with one-second long pulses at two frequencies. The top panel shows the reception on the satellite. Note the time delay of ~0.3 seconds. Also note the reception of a whistler trace in the middle.

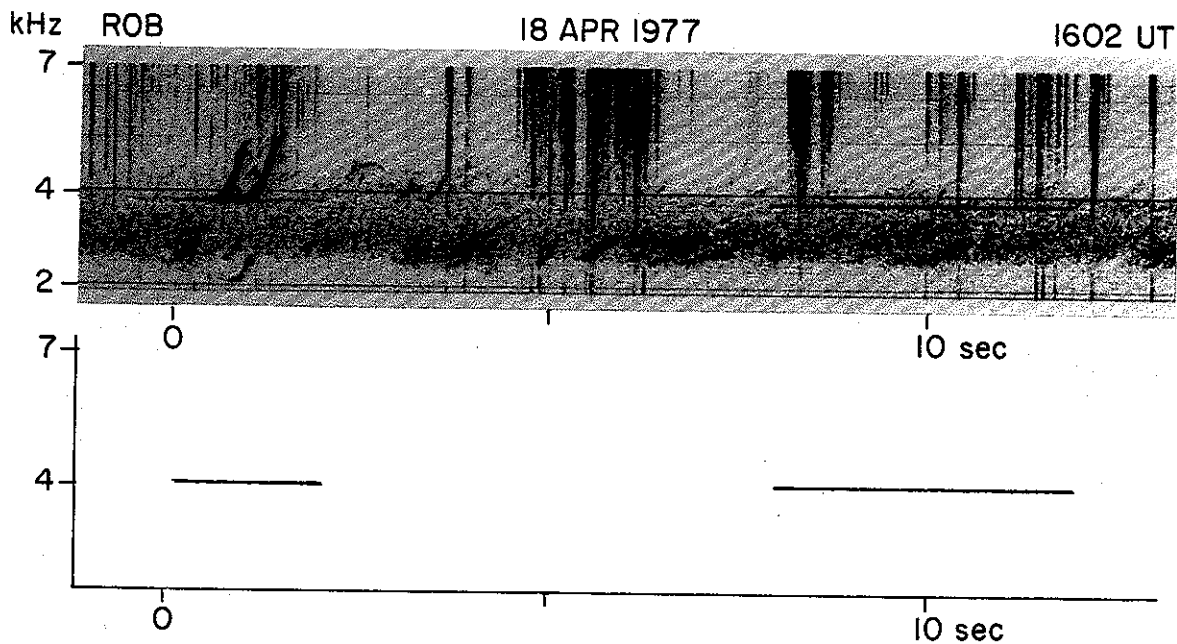


FIGURE 2.7 TRANSMITTER SIGNALS RECEIVED AT THE CONJUGATE POINT AT ROBERVAL, CANADA. The transmitter format is shown below. Note that the first 2-second long pulse has triggered strong emissions. The theory of triggered VLF emissions is not fully understood, although it is thought that the changing frequency is caused by the inhomogeneity of the magnetic field [Helliwell, 1967, 1970]. Note that although the emissions change frequency with time, they are still quite narrowband and coherent signals. The second pulse (4-second long) has not triggered emissions and it does not show any large amplification. For the parameters used in our computations, a 4-second pulse is approximately equivalent to a CW.

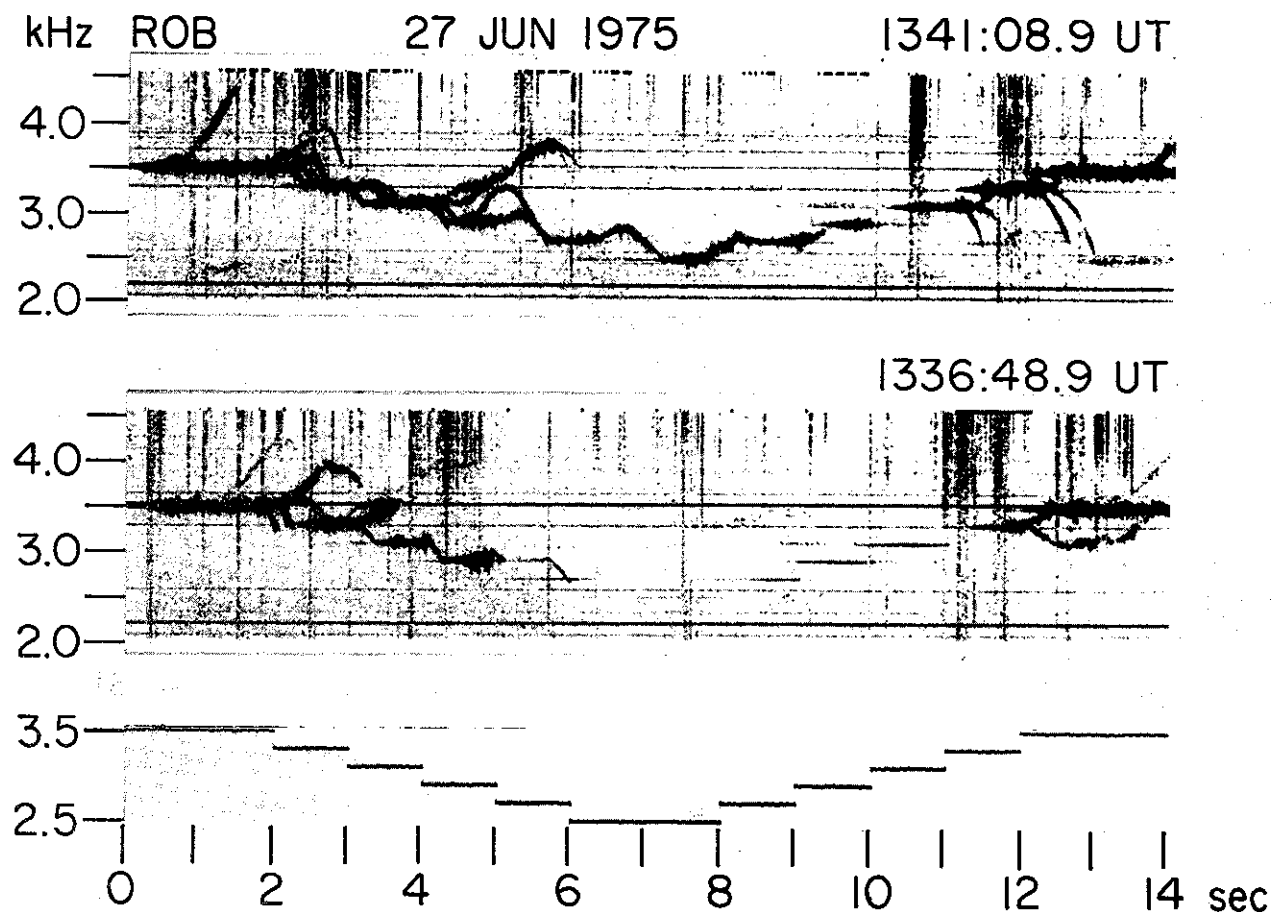


FIGURE 2.8 RECEPTION OF TRANSMITTER SIGNALS [Helliwell and Katsufrakis, 1977]. The bottom panel shows the transmitted format which in this case is a staircase pattern. The receptions at Roberval at two different times are given. Note that the transmitter signals trigger falling and inverted hook emissions [Helliwell, 1965], that are entrained by the next pulse. Also note the amplification of the pulses before triggering. The pulses in the last portion of the middle panel do not show any triggering.

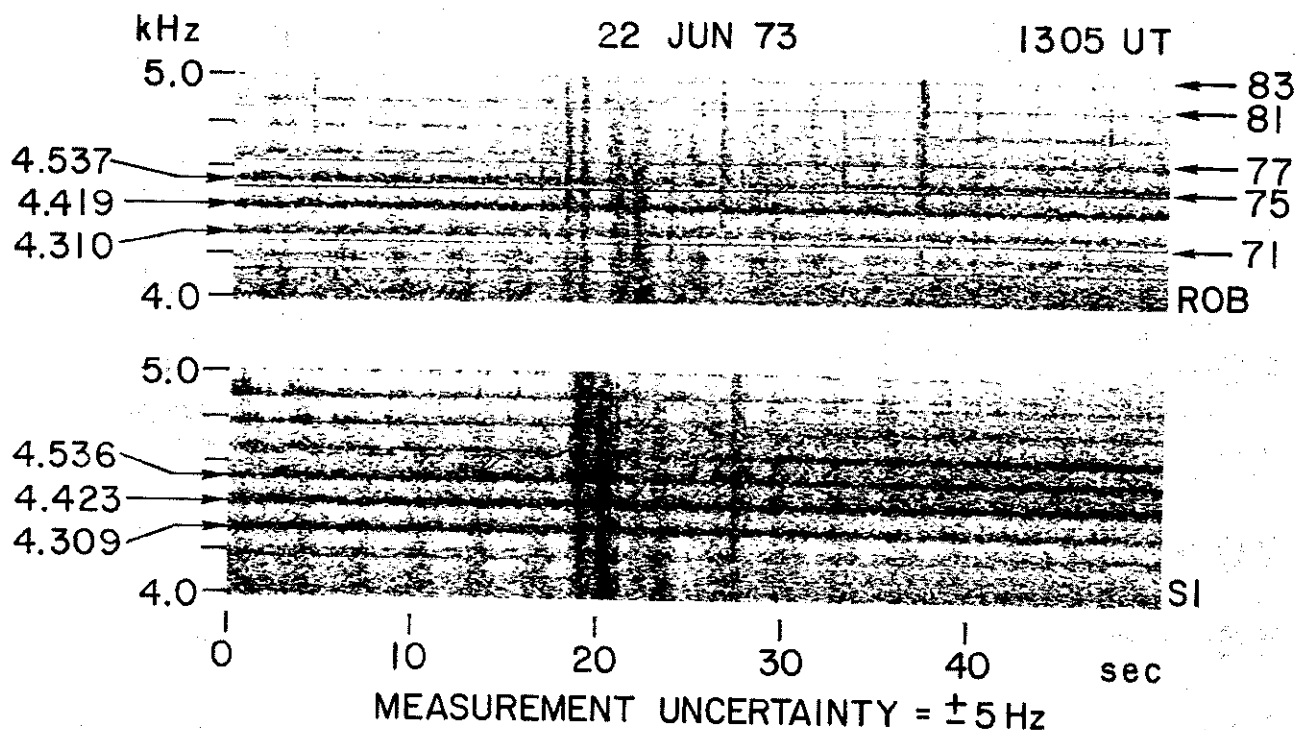


FIGURE 2.9 EXAMPLE OF POWER LINE RADIATION INTO THE MAGNETOSPHERE [Helliwell et al., 1975]. Simultaneous spectra from the conjugate stations Siple and Roberval are given. The broad horizontal lines on the spectra are spaced roughly 120 Hz apart and are closely associated with the relatively thin induction lines shown on the spectrum from Roberval. Some of these induction lines are identified on the right hand side by their harmonic order. Note that these are due to the Canadian power grid and therefore they are harmonics of 60 Hz. Note that the induction lines are not present at Siple although the magnetospheric lines radiated by the power grid are. The small separation between the magnetospheric lines and the induction lines is thought to result from the triggering of rising emissions by the actual power line harmonic component. These emissions form a somewhat irregular band just above the induction power lines.

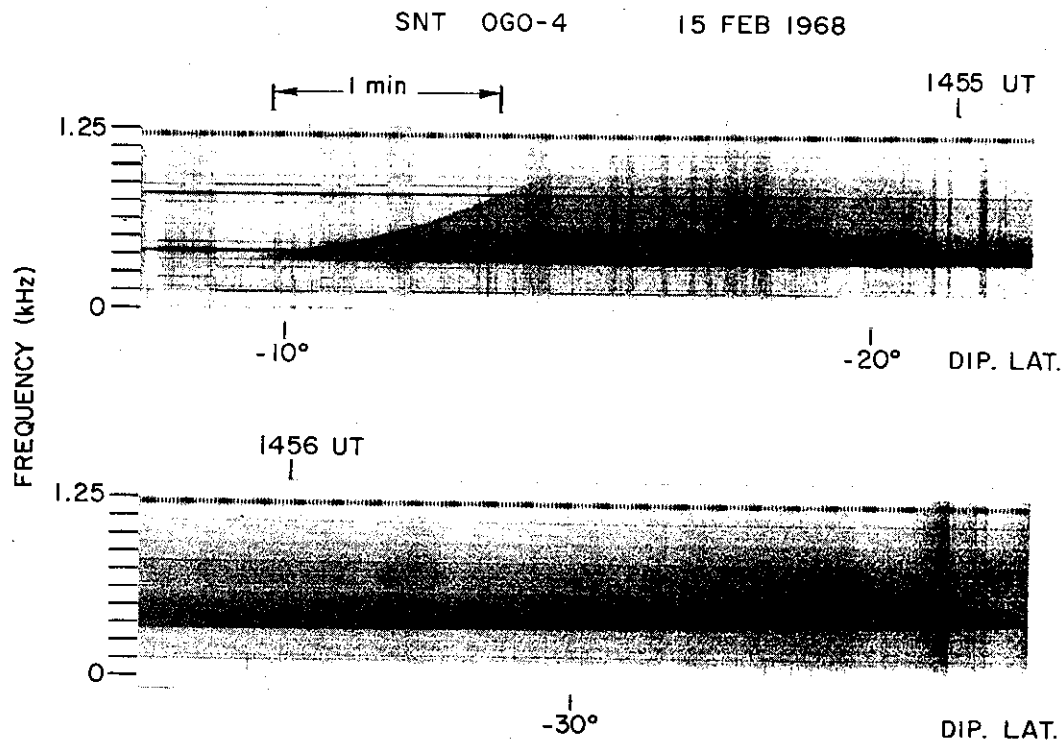


FIGURE 2.10 SPECTROGRAM OF A TYPICAL EXAMPLE OF OBSERVATION OF ELF HISS ON THE OGO-4 SATELLITE [Muzzio, 1971]. The reception as the satellite moves from -5° to beyond -30° dipole latitude is shown. Note that the hiss is an incoherent, broadband signal with a well defined lower cutoff frequency. Note from the upper panel that the upper cutoff varies from ~ 400 Hz to ~ 800 Hz in one minute corresponding to a latitude range of $\sim 3.5^\circ$.

lite of ELF hiss as an example of such a signal. The details are described in the figure caption.

Longitudinal Whistler Mode Waves

In our simulation of the cyclotron resonance wave particle interaction we will consider the case of the wave propagation directly along the ambient magnetic field lines, i.e. $\vec{k} \parallel \vec{B}_0$. Exact longitudinal propagation is unlikely to occur, of course, but in light of the duct theory of whistler propagation [Smith, 1961], it is a reasonable approximation. This assumption considerably simplifies the equations of motion.

For $\vec{k} \parallel \vec{B}_0$, i.e. $\theta = 0$, Eqs. (2.18) and (2.19) reduce to

$$n^2 = 1 - \frac{f_p^2}{f(f \pm f_H)} \quad (2.21)$$

and

$$\delta = \pm i \quad (2.22)$$

In the inner magnetosphere $f_p^2 \gg f_H^2$, and for $f < f_H$ the choice of the lower sign in (2.21) results in $n^2 < 0$, i.e. a nonpropagating wave. In light of this and using $f_p^2 \gg f_H^2$ we can rewrite the refractive index and wave polarization for longitudinal whistler mode waves in the earth's magnetosphere

$$n = \frac{kc}{2\pi f} \approx f_p \left[\frac{1}{f(f_H - f)} \right]^{1/2} \quad (2.23)$$

and

$$\delta = +i \quad (2.24)$$

where c is the speed of light and k is the wave number in the medium. Other useful expressions that can be derived from (2.23) are given below

$$k = \frac{2\pi f_p}{c} \left(\frac{f}{f_H - f} \right)^{1/2} \quad (2.25)$$

$$v_p = \frac{\omega}{k} = c \frac{f^{1/2} (f_H - f)^{1/2}}{f_p} \quad (2.26)$$

$$v_g = \frac{d\omega}{dk} = 2c \frac{f^{1/2} (f_H - f)^{3/2}}{f_p f_H} \quad (2.27)$$

where v_g is the group velocity which is equal to signal propagation velocity for longitudinal propagation.

Equation (2.24) indicates that these waves are right hand circularly polarized, i.e. the wave vectors rotate in the same sense as electrons about the field lines. Both the wave electric and magnetic fields are transverse to \bar{B}_0 . The wave vectors traverse a helix in space as shown in Fig. 2.11. Since $\bar{E}_w \cdot \bar{k}$, $\bar{k} \cdot \bar{E}_w = 0$ and we have $\rho_s = 0$, which means that the wave will propagate without space-charge. The plasma manifests itself via currents which flow in planes normal to \bar{k} and \bar{B}_0 .

The expressions for \bar{E}_w and \bar{B}_w given in Fig. 2.7 are for propagation in a homogeneous medium. Although the magnetospheric medium is inhomogeneous the variations in ω_H and ω_p within the space of one wavelength are negligible. Therefore, the W.K.B. approximation [Budden, 1961] can be used and the wave fields can still be expressed as progressive waves as follows:

$$\bar{B}_w = B_w \left[\bar{a}_x \cos(\omega t - \int_0^z k dz) + \bar{a}_y \sin(\omega t - \int_0^z k dz) \right] \quad (2.28)$$

$$\bar{E}_w = \frac{\omega}{k} B_w \left[\bar{a}_x \sin(\omega t - \int_0^z k dz) - \bar{a}_y \cos(\omega t - \int_0^z k dz) \right]$$

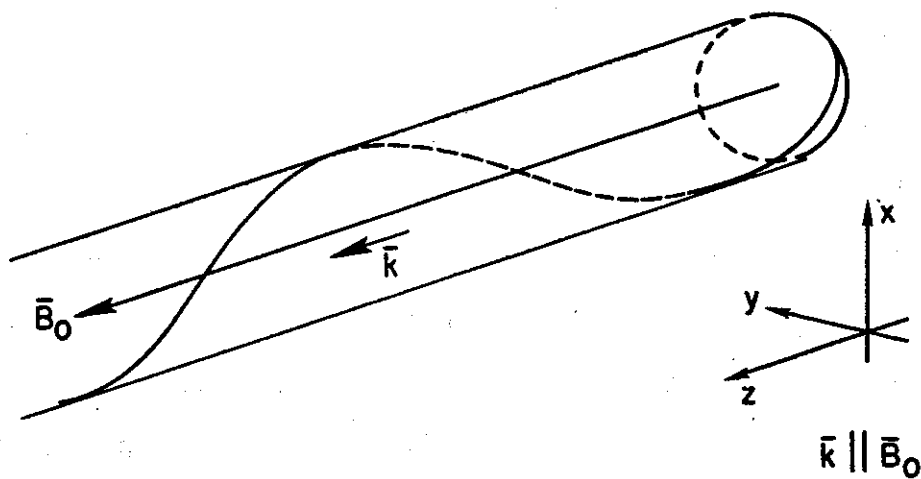


FIGURE 2.11 LONGITUDINAL WHISTLER-MODE WAVE FIELDS. Helical[⊙] locus of the wave magnetic field is shown. The corresponding wave electric field locus is a similar helix but 90° out of phase such that at each point $\vec{E}_w \times \vec{B}_w$ is in the direction of \vec{k} . The wave fields can be expressed as:

$$\vec{B}_w = B_w [\vec{a}_x \cos(\omega t - kz) + \vec{a}_y \sin(\omega t - kz)]$$

and

$$\vec{E}_w = E_w [\vec{a}_x \sin(\omega t - kz) - \vec{a}_y \cos(\omega t - kz)]$$

In the next section we develop the equations of motion for energetic particles in a longitudinal whistler mode wave as described above.

D. EQUATIONS OF MOTION

In this section we shall derive and discuss the equations that govern the motion of an energetic particle in a longitudinal whistler mode wave.

The basic assumption that has been experimentally verified as mentioned in previous sections is that the energetic particle motions often do not significantly affect the propagation of the wave or each other. This assumption is justified by the fact that the total density of the energetic particles is much less than the cold plasma density. The wave's dispersion and propagation characteristics are governed entirely by the 'cold' plasma which can be safely assumed to be collisionless. The refractive index, n , is then given by (2.23) and the cold plasma acts only as a slow wave structure for the whistler mode, similar to slow wave structures in microwave tubes. The energetic particles can then be considered as a separate 'beam' of electrons, again similar to electron beams in microwave tubes. The problem is more complex because of the transverse gyration as well as longitudinal motions of both the wave vectors and the electron beam. On the other hand there is no significant space-charge bunching involved in the longitudinal cyclotron resonance mechanism.

In order for the wave to induce cumulative energy and/or momentum changes in the particle the wave vectors as 'seen' by the particle must be approximately stationary for a significant length of time. This means that the doppler shifted frequency as 'seen' by the particle must be

approximately equal to its gyrofrequency, i.e.

$$\omega - \bar{\mathbf{k}} \cdot \bar{\mathbf{v}} \approx \omega_H \quad (2.29)$$

This is the cyclotron (or gyro) resonance condition. For the whistler mode, where $\omega < \omega_H$, (2.29) can be satisfied only if $\bar{\mathbf{k}} \cdot \bar{\mathbf{v}} < 0$ or when the resonant electrons and the wave travel in opposite directions. We can then rewrite (2.29) as

$$\omega + kv_{\parallel} \approx \omega_H \quad (2.30)$$

where v_{\parallel} is the particle velocity along $-\bar{\mathbf{B}}_0$ as shown in Fig. 2.12.

In the absence of the wave the energetic particles are trapped along a given field line and their unperturbed motion, neglecting the small azimuthal drift, can be described by the following relations which can be derived from the adiabatic invariant relation (2.7):

$$\begin{aligned} \left(\frac{dv_{\parallel}}{dt} \right)_u &= - \frac{v_{\perp}^2}{2B_0} \frac{dB_0}{dz} \\ \left(\frac{dv_{\perp}}{dt} \right)_u &= + \frac{v_{\parallel} v_{\perp}}{2B_0} \frac{dB_0}{dz} \end{aligned} \quad (2.31)$$

The coordinate system and the variables are defined in Fig. 2.12.

The force $\bar{\mathbf{F}}$ applied to a particle by the wave is given by

$$\bar{\mathbf{F}} = q(\bar{\mathbf{E}}_w + \bar{\mathbf{v}} \times \bar{\mathbf{B}}_w) \quad (2.32)$$

where $\bar{\mathbf{v}} = \bar{v}_{\parallel} + \bar{v}_{\perp}$ is the total particle velocity. Separating $\bar{\mathbf{F}}$ into its components parallel and perpendicular to $\bar{\mathbf{B}}_0$ we have

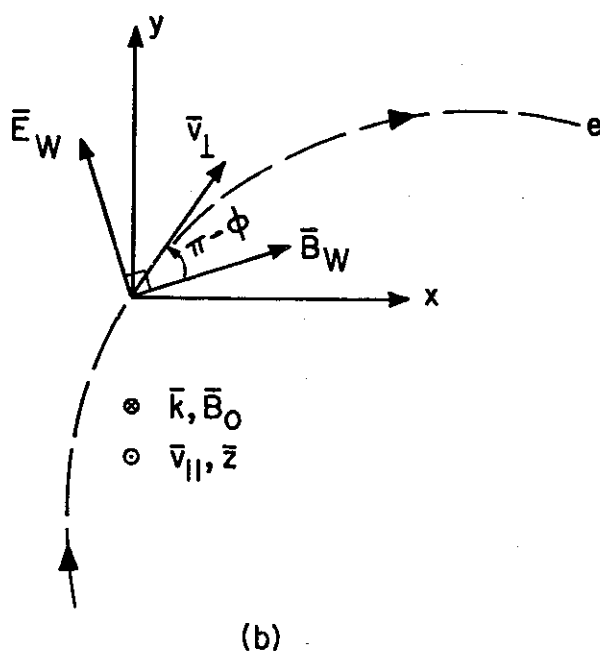
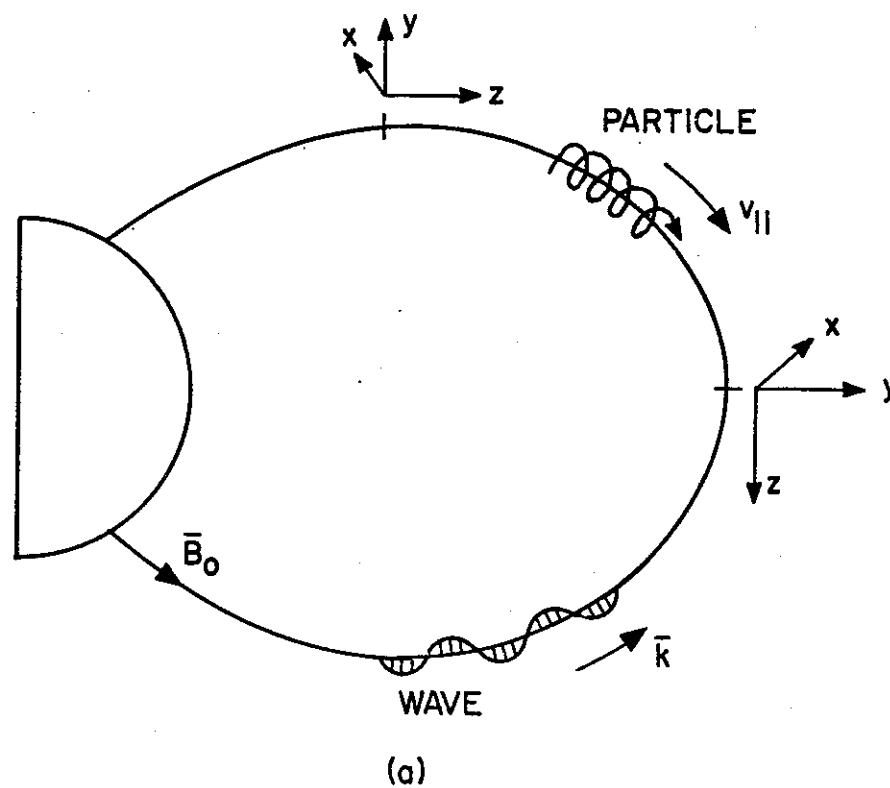


FIGURE 2.12 COORDINATE SYSTEM FOR THE EQUATIONS OF MOTION. Note that the z -axis is everywhere aligned with the magnetic field line. Shown in dashed lines is the orbit of the electron in the x - y plane.

$$\vec{F} = \vec{F}_{\parallel} + \vec{F}_{\perp} = -e[\vec{E}_w + \vec{v}_{\parallel} \times \vec{B}_w + \vec{v}_{\perp} \times \vec{B}_w] \quad (2.33)$$

Since both \vec{E}_w and \vec{B}_w are perpendicular to \vec{k} and \vec{B}_0 (2.33) can be expressed as

$$\vec{F}_{\parallel} = -e \vec{v}_{\perp} \times \vec{B}_w \quad (2.34a)$$

$$\vec{F}_{\perp} = -e \vec{E}_w - e \vec{v}_{\parallel} \times \vec{B}_w \quad (2.34b)$$

The force \vec{F}_{\parallel} provides an acceleration along \vec{v}_{\parallel} , whereas \vec{F}_{\perp} is in general in the same plane but at some angle with \vec{v}_{\perp} . With the coordinate system as given in Fig. 2.12 and using (2.34a,b) we can write the wave induced accelerations along \vec{v}_{\parallel} and \vec{v}_{\perp} as:

$$\left(\frac{dv_{\parallel}}{dt}\right)_{\text{wave}} = -\frac{e}{m} |\vec{v}_{\perp}| |\vec{B}_w| \sin\phi = \left(\frac{eB_w}{m}\right) v_{\perp} \sin\phi \quad (2.35a)$$

$$\left(\frac{dv_{\perp}}{dt}\right)_{\text{wave}} = -\frac{e}{m} |\vec{E}_w| \sin\phi - \frac{e}{m} |\vec{v}_{\parallel}| |\vec{B}_w| \sin\phi = -\left(\frac{eE_w}{m}\right) \sin\phi - \left(\frac{eB_w}{m}\right) v_{\parallel} \sin\phi \quad (2.35b)$$

where ϕ is the angle between \vec{v}_{\perp} and $-\vec{B}_w$ as shown in Fig. 2.12.

Note that the differential equations (2.35), when integrated properly completely describe the wave's effect on the particle velocity components v_{\parallel} and v_{\perp} . Note also that both $\frac{dv_{\parallel}}{dt}$ and $\frac{dv_{\perp}}{dt}$ are proportional to $\sin\phi$, meaning that whether or not there is any integrated cumulative change in v_{\parallel} and v_{\perp} depends on the variation of ϕ . The rate of change of ϕ is given by

$$\frac{d\phi}{dt} = (\omega_H - \omega - kv_{\parallel}) - \left(\frac{eB_w}{m}\right) v_{\parallel} \frac{\cos\phi}{v_{\perp}} - \left(\frac{eE_w}{m}\right) \frac{\cos\phi}{v_{\perp}} \quad (2.35c)$$

The first term on the right hand side of the above represents the difference between the doppler shifted wave frequency seen by the particle and its own gyrofrequency, which by definition is the rate of change of ϕ to first order. The last two terms give the phase change due to centripetal acceleration of the particle resulting from $\vec{v}_{\parallel} \times \vec{B}_w$ and \vec{E}_w forces. This centripetal acceleration modifies the particle motion about its guiding center so that the angular frequency of oscillation about the static magnetic field deviates slightly from the gyrofrequency, ω_H .

Equations (2.35a,b) give only the wave induced variations in v_{\parallel} and v_{\perp} . However these quantities also vary due to the inhomogeneity of the ambient field as given by (2.7) and (2.31). Superimposing these on (2.35a,b), using $|E_w| = \left|\frac{\omega}{k} B_w\right|$ and combining terms we obtain the equations of motion,

$$\dot{v}_{\parallel} = \left(\frac{eB_w}{m}\right) v_{\perp} \sin\phi - \frac{v_{\perp}}{2\omega_H} \frac{d\omega_H}{dz} \quad (2.36a)$$

$$\dot{v}_{\perp} = - \left(\frac{eB_w}{m}\right) \left(v_{\parallel} + \frac{\omega}{k}\right) \sin\phi + \frac{v_{\perp} v_{\parallel}}{2\omega_H} \frac{d\omega_H}{dz} \quad (2.36b)$$

$$\dot{\phi} = \overset{\uparrow}{\omega_H - \omega - kv_{\parallel}} - \left(\frac{eB_w}{m}\right) \left(v_{\parallel} + \frac{\omega}{k}\right) \frac{\cos\phi}{v_{\perp}} \quad (2.36c)$$

where the "." represents the derivative with respect to time. Since the medium is inhomogeneous the quantities ω_H and k are functions of z , the distance along the field line. Equations (2.36) are written in the laboratory frame, with the coordinate system as described in Fig.

2.12. For our purposes no important simplification results by trans-

forming to either the wave or the particle frames.

Equations (2.36) in whole or in part have been used to study VLF wave particle interactions by many authors [Bell, 1964; Brice, 1964; Bell, 1965; Helliwell, 1967, 1970; Dysthe, 1971; Nunn, 1971, 1974; Palmadesso and Schmidt, 1971, 1972; Matsumoto, 1972; Ashour-Abdalla, 1972; Bud'ko et al., 1972; Crystal, 1973; Helliwell and Crystal, 1973; Roux and Pellat, 1976; Karpman et al., 1974a,b]. Dysthe [1971] was the first to include the adiabatic terms in Eqs. (2.36a) and (2.36b).

The entire physics of the interaction is embodied in Eqs. (2.36a,b and c). For this reason a brief discussion of the importance of different terms in (2.36) is in order. The first terms in Eqs. (2.36a) and (2.36b) are due to the wave induced longitudinal and transverse forces $\bar{v}_\perp \times \bar{B}_w$ and $(\bar{v}_\parallel \times \bar{B}_w + \bar{E}_w)$ respectively. Also both of these equations have an additional term which gives the adiabatic variations of v_\parallel and v_\perp that are superimposed on the wave perturbations. It should be noted that although the presence of field aligned wave forces violates the assumptions underlying the first adiabatic invariant [Roederer, 1970], the changes in v_\parallel and v_\perp due to changing static magnetic field intensity can still be described by the differential adiabatic theory at each point during the interaction. In other words, Eqs. (2.36) are differential equations valid at each point along the field line.

Since the wave terms in Eqs. (2.36a) and (2.36b) are proportional to $\sin\phi$ it is apparent that the interaction is strongly controlled by the third equation (2.36c) which gives the variation of ϕ . Cumulative changes in v_\parallel and v_\perp will only result when $\dot{\phi}$ (and $\ddot{\phi}$) is small. The wave term in Eq. (2.36c) (last term on the r.h.s.) gives the phase

change due to the centripetal acceleration of the particle resulting from the $(\vec{v}_{\parallel} \times \vec{B}_w + \vec{E}_w)$ force. We have found that for most magnetospheric parameters the effect of this term is negligible, especially for large pitch angles (large v_{\perp}) and/or small wave amplitudes. However, even for small wave intensities this wave term becomes dominant as soon as the pitch angle falls below 1 or 2 degrees. Note that individual particles that have somewhat larger initial pitch angles could still be scattered down to these low pitch angles during the interaction. At that time this term must be present in the equations in order to correctly describe the physics.

The Eqs. (2.36) define the motion of each individual electron. For a particle with initial velocities of $v_{\parallel 0}$ and $v_{\perp 0}$ and an initial phase of ϕ_0 , these equations, when properly integrated over time, give the resulting Δv_{\parallel} and Δv_{\perp} for that particle. In other words

$$\begin{aligned}\Delta v_{\parallel} &= \int_0^{T_I} \dot{v}_{\parallel} dt \\ \Delta v_{\perp} &= \int_0^{T_I} \dot{v}_{\perp} dt\end{aligned}\tag{2.37}$$

where T_I is the interaction time. In principle, the integration must be carried out for $T_I \rightarrow \infty$. However because of the changing ω_H due to the inhomogeneity of the field the resonance condition (2.30) can be satisfied only over a limited region along the field line for any given particle. When (2.30) is not satisfied, it is apparent from Eq. (2.36c) that $|\dot{\phi}|$ would be large and the wave contributions to \dot{v}_{\parallel} and \dot{v}_{\perp} will be noncumulative. Therefore a time T_I can be defined over which

the wave induced perturbations are significant.

As a result of its encounter with the wave, the particles v_{\parallel} and v_{\perp} changes. These changes Δv_{\parallel} and Δv_{\perp} can be viewed as a scattering in velocity space and are hereafter referred to as "scattering."

As is apparent from the differential equations (2.36) the point-to-point scatterings (and therefore the integrated total scatterings) depend on $v_{\parallel 0}$ and $v_{\perp 0}$, as well as on the initial phase ϕ_0 between v_{\perp} and $-B_w$ at the time of encounter between the wave and the particle. The scattering also depends on wave parameters B_w , ω and k and medium parameters ω_H and $\frac{\partial \omega_H}{\partial z}$. In general when the resonance occurs away from the equator, for constant frequency, the cumulative interaction time is shortened (since $\frac{\partial \omega_H}{\partial z}$ is larger) and the total scattering is smaller. The quantity $\frac{\partial \omega_H}{\partial z}$ is the principal factor which determines the interaction time T_I .

In order to clearly see the effect of $\frac{\partial \omega_H}{\partial z}$ we follow a procedure similar to that used by Dysthe [1971]. Neglecting the wave terms on the r.h.s. of Eq. (2.36c) we can rewrite it as:

$$\dot{\phi} = \omega_H - \omega - kv_{\parallel} = k(v_R - v_{\parallel}) \quad (2.38)$$

where $v_R = \frac{\omega_H - \omega}{k}$ is the resonance velocity obtained from (2.30). Differentiating the above we obtain

$$\ddot{\phi} = k(\dot{v}_R - \dot{v}_{\parallel}) + \dot{k}(v_R - v_{\parallel}) \quad (2.39)$$

for monochromatic waves ($\dot{\omega}=0$). Since we are concerned with resonant or closely resonant particles, $v_{\parallel} \approx v_R$ and to a good approximation (2.39) reduces to

$$\ddot{\phi} = k(\dot{v}_R - \dot{v}_{||}) \quad (2.40)$$

Substituting $\dot{v}_{||}$ from Eq. (2.36a) we have

$$\ddot{\phi} = k\dot{v}_R - k \left(\frac{eB_w}{m} \right) v_{\perp} \sin\phi + \frac{kv_{\perp}^2}{2\omega_H} \frac{\partial\omega_H}{\partial z} \quad (2.41)$$

We have

$$\dot{v}_R = \frac{d}{dt} \left[\frac{\omega_H - \omega}{k} \right] = \frac{\dot{\omega}_H k - (\omega_H - \omega) \dot{k}}{k^2} \quad (2.42)$$

Rewriting Eq. (2.25) for k ,

$$k = \frac{\omega_p \omega^{1/2}}{c} (\omega_H - \omega)^{-1/2} \quad (2.43)$$

In a diffusive equilibrium model of the cold plasma, such as the one used in this report, the plasma frequency ω_p is approximately constant along the field line. Hence $\dot{\omega}_p \approx 0$, and we obtain

$$\dot{k} = \left(-\frac{1}{2} \right) \frac{\omega_p \omega^{1/2}}{c} (\omega_H - \omega)^{-3/2} \dot{\omega}_H = -\frac{k}{2(\omega_H - \omega)} \dot{\omega}_H = -\frac{kv_{||}}{2(\omega_H - \omega)} \frac{\partial\omega_H}{\partial z} \quad (2.44)$$

Substituting in (2.42) and then (2.41) and rearranging terms we obtain

$$\ddot{\phi} + k \left(\frac{eB_w}{m} \right) v_{\perp} \sin\phi = \left[\frac{3}{2} v_{||} + \frac{kv_{\perp}}{2\omega_H} \right] \frac{\partial\omega_H}{\partial z} \quad (2.45)$$

Equation (2.45) is a type of 'pendulum' equation which gives the variation of the phase ϕ . The forcing function of this equation is proportional to $\frac{\partial\omega_H}{\partial z}$, hence demonstrating the influence of the term $\frac{\partial\omega_H}{\partial z}$, i.e. the inhomogeneity force, in controlling the interaction. The total interaction time T_I is determined by the relative magnitudes of this forcing function and the restoring 'force' (the wave force) of the pendulum which is proportional to $k \left(\frac{eB_w}{m} \right) v_{\perp}$.

E. ENERGY AND MOMENTUM TRANSFER

Equations (2.36) are in terms of the velocity components v_{\parallel} and v_{\perp} . This formulation is useful, since the resonance condition (2.30) is in terms of v_{\parallel} . However, in order to see the energy and pitch angle changes of the particle more clearly it is convenient to express the equations of motion in terms of v and α .

Using $v_{\parallel} = v \cos \alpha$ and $v_{\perp} = v \sin \alpha$ and Eqs. (2.7), (2.31) and (2.36) we obtain

$$\frac{dv}{dt} = -\left(\frac{eE_w}{m_w}\right) \sin \alpha \sin \phi \quad (2.46a)$$

$$\frac{d\alpha}{dt} = -\left(\frac{eB_w}{m_w}\right) \sin \phi - \left(\frac{eE_w}{m_w}\right) \frac{\cos \alpha}{v} \sin \phi + \frac{v \sin \alpha}{\omega_H} \frac{d\omega_H}{dz} \quad (2.46b)$$

$$\frac{d\phi}{dt} = \omega_H - \omega - kv \cos \alpha - \left(\frac{eB_w}{m_w}\right) \frac{\cos \alpha}{\sin \alpha} \cos \phi - \left(\frac{eE_w}{m_w}\right) \frac{\cos \alpha}{v \sin \alpha} \cos \phi \quad (2.46c)$$

In the above, the last term in (2.46b) is the equivalent of the last terms in (2.36a,b). Note that Eq. (2.46a) directly gives the energy change of the particle, since the total particle kinetic energy is $K_E = 1/2 mv^2$. The energy exchange can only occur through the electric field of the wave since magnetic forces are always perpendicular to the direction of motion. Since the E_w for our case is purely transverse, energy exchange can only occur through v_{\perp} . For this reason any energy exchange will also result in pitch angle change as shown by the E_w term in Eq. (2.46b). Although B_w cannot induce energy change, it is apparent from (2.46b) that it causes a pitch angle change. The pitch angle change is in essence a change in the direction of momentum (or velocity) of the particle.

Considering only the wave perturbations, i.e. neglecting the adiabatic term in Eq. (2.46b) and using $E_w = \frac{\omega}{k} B_w$ we find from (2.46a,b) that

$$\frac{d\alpha}{dv} = \frac{\left[\frac{k}{\omega} + \frac{\cos\alpha}{v} \right]}{\sin\alpha} \quad (2.47)$$

In order to compare normalized pitch angle changes to normalized changes in energy we can form the following ratio using (2.47)

$$\eta = \frac{\frac{d\alpha}{\alpha}}{\frac{dK_E}{K_E}} = \frac{\left[\frac{v_{\parallel}}{v_p} + \cos^2\alpha \right]}{\alpha \sin 2\alpha} \quad (2.48)$$

where v_p is the wave phase velocity.

Since only the particles at or close to resonance with the wave will suffer significant scattering we use (2.30) in conjunction with (2.25) and (2.26) to obtain

$$\frac{v_{\parallel}}{v_p} = \frac{f_H - f}{f} \quad (2.49)$$

Substituting this in (2.48) we have

$$\eta = \frac{\frac{d\alpha}{\alpha}}{\frac{dK_E}{K_E}} = \frac{\left[\frac{f_H - f}{f} + \cos^2\alpha \right]}{\alpha \sin 2\alpha} \quad (2.50)$$

In (2.50) η is independent of the plasma frequency f_p . We have plotted (2.50) against pitch angle for typical values of $f_H = 13.65$ kHz at the equator on the $L = 4$ field line) and a few different typical values of wave frequency f in Fig. 2.13. Since we have used the value of f_H at the equator the results shown are only for resonances at the

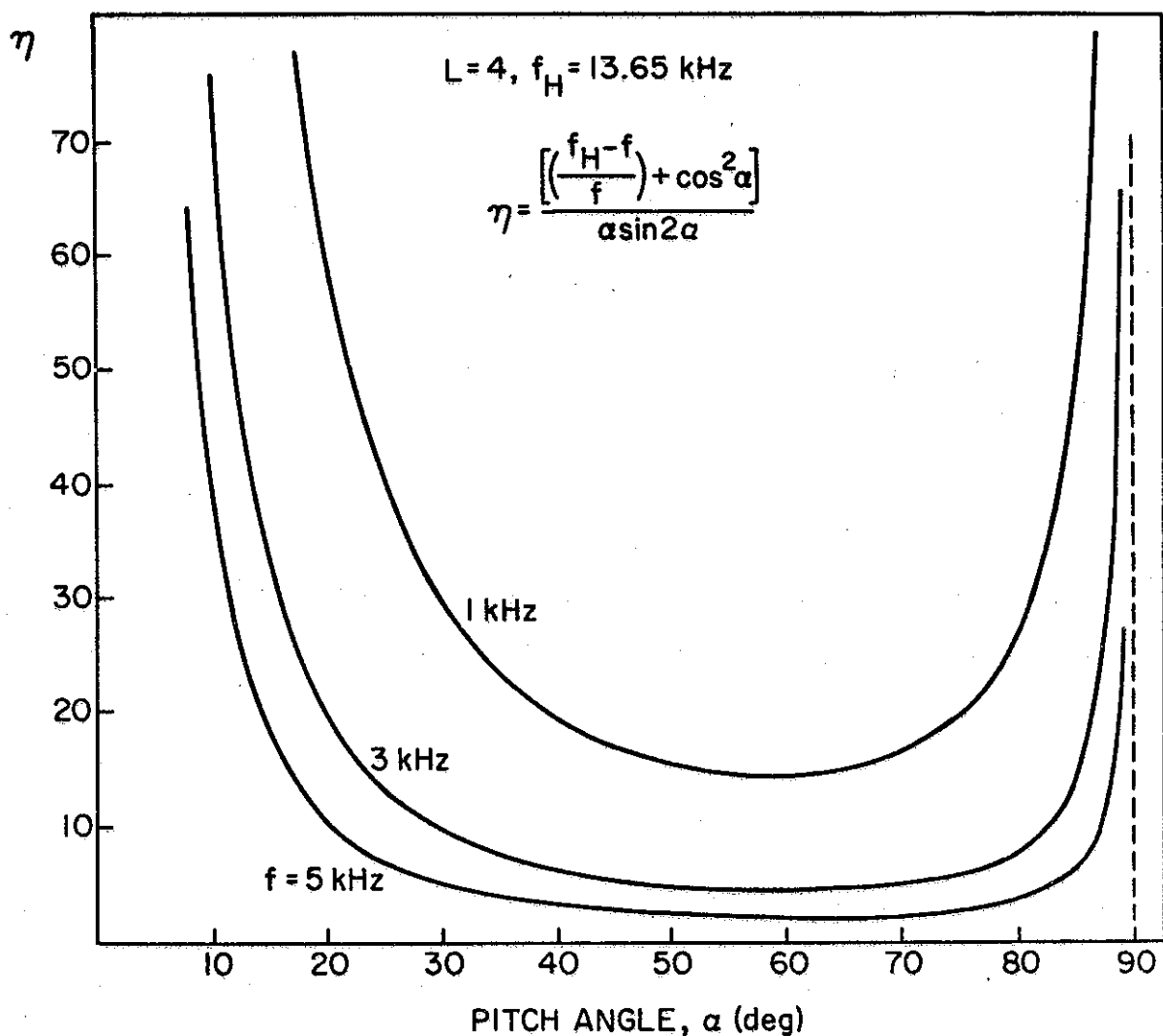


FIGURE 2.13 THE QUANTITY, η , DEFINED AS THE RATIO OF PERCENTAGE PITCH ANGLE CHANGE TO PERCENTAGE ENERGY CHANGE AS A FUNCTION OF PITCH ANGLE. The results plotted are for $f_H = 13.65 \text{ kHz}$ corresponding to equator on the $L = 4$ field line. A few different typical values for the wave frequency is used.

equator. For off-equatorial resonances f_H is larger and therefore η would be even higher. Figure 2.13 shows that $\eta \gg 1$ for most cases and $\eta > 1$ for all cases considered. This means that large percentage pitch angle changes can be induced without much energy transfer. Hence even a weak wave could produce significant pitch angle perturbations. Note for example that the loss cone at $L = 4$ is about 5.5° wide. Therefore to precipitate a particle with $\alpha = 10^\circ$ into the loss cone requires ~50% pitch angle change. Since $\eta \approx 40$ from Fig. 2.13, this requires only a 1.2% change in energy.

It will be shown in the last sections of this report that, consistent with the arguments above, the total precipitated energy flux is 50 dB higher than the wave input energy. The wave induced precipitation occurs through change of direction of momentum of the particles rather than through energy exchanges. In this particular gyroresonant wave-particle interaction where the whistler mode wave involved is a 'slow' wave with $v_p \approx 0.01c-0.1c$, wave magnetic field effects upon particle motion are generally more important than the wave electric field effects. The wave magnetic field cannot induce energy exchange, but it can change the particle pitch angle, i.e. direction of momentum.

F. LINEAR THEORY

Later in this report, we will be comparing our results with linear theory which has been used by previous workers in this field. In Chapter 4 we derive a quantitative criterion for determining the applicability of linear theory under given conditions. For these reasons we devote this section to a brief discussion of linear theory.

The basic problem is the integration of Eqs. (2.36a,b) in order to obtain the perturbed values of v_{\parallel} and v_{\perp} . One common approach is to use linear theory [Das, 1971; Ashour-Abdalla, 1972]. According to this theory the wave induced scatterings, Δv_{\parallel} and Δv_{\perp} , are computed by using wave field components at the position of the particle as given by the unperturbed ($B_w = 0$) motion. In other words it is assumed that the wave effects are so small that the variation of ϕ (as given by (2.36c)) is very close to what it would have been for $B_w = 0$. In that case, the starting point is

$$\dot{\phi} = \omega_H - \omega - kv_{\parallel} = f(t) \quad (2.51)$$

where $f(t)$ is some function of t which is defined by the variation of ω_H and v_{\parallel} along the particle trajectory. Then

$$\phi = \phi_u = F(t) + \phi_0 \quad (2.52)$$

where $F(t) = \int_0^t f(t') dt'$. The function $F(t)$ does not depend on wave intensity and is independent only on ω_H , $\frac{\partial \omega_H}{\partial z}$, k and pitch angle. Equation (2.52) thus gives the unperturbed (ϕ_u) variation of the phase. Using analytical models for $\omega_H(z)$ and $k(z)$ it is possible to find an expression for ϕ_u [Hellwells, 1970].

When this unperturbed variation for ϕ is used the integration of (2.36a,b) becomes relatively easy. The linear theory calculation of Δv_{\parallel} and Δv_{\perp} then proceeds by substituting ϕ_u into Eq. (2.36a,b) and integrating

$$\Delta v_{\parallel} = \int_0^{\infty} \left(\frac{eB_w}{m} \right) v_{\perp} \sin[F(t) + \phi_0] dt \approx \left(\frac{eB_w}{m} \right) v_{\perp} \int_0^{\infty} \sin[F(t) + \phi_0] dt \quad (2.53a)$$

$$\Delta v_{\perp} = - \int_0^{\infty} \left(\frac{eB_w}{m} \right) \left(v_{\parallel} + \frac{\omega}{k} \right) \sin[F(t) + \phi_0] dt \approx - \left(\frac{eB_w}{m} \right) \left(v_{\parallel} + \frac{\omega}{k} \right) \int_0^{\infty} \sin[F(t) + \phi_0] dt \quad (2.53b)$$

where the adiabatic terms in (2.36a,b) have been dropped. In the above equations Δv_{\parallel} and Δv_{\perp} are the total changes in v_{\parallel} and v_{\perp} . In moving v_{\perp} and $(v_{\parallel} + \frac{\omega}{k})$ out of the integral in (2.53a) and (2.53b) respectively, we have used the linear theory assumption that the adiabatic variations in v_{\perp} and v_{\parallel} are small during the time the particle is close to resonance, and that $\Delta v_{\perp} \ll v_{\perp}$ and $\Delta v_{\parallel} \ll v_{\parallel}$. The former assumption is valid unless the initial pitch angle is very large or the resonance point is at high latitudes. The latter is a requirement of linear theory and is consistent with the small wave intensities that justify the application of this theory.

With certain simplifying assumptions the integrations in (2.53a) and (2.53b) can be carried out and analytical expressions for Δv_{\parallel} and Δv_{\perp} can be obtained [Ashour-Abdalla, 1972].

Although it is generally agreed that linear theory is applicable for sufficiently low wave intensities, none of the authors who have employed this theory in their analyses has given quantitative criteria to justify their assumptions. In Chapter 4 we develop a simple quantitative criteria that can be used to determine the applicability of linear theory under given conditions. Qualitatively, when the wave intensity is large, the wave induced variations in v_{\parallel} are significant. This couples to $\dot{\phi}$

through $v_{||}$ in Eq. (2.36c) and causes $\phi(t)$ to deviate from ϕ_u . Therefore linear theory cannot be used and a complete integration of the coupled equations (2.36) must be carried out.

Integration of these highly nonlinear equations is best done on a digital computer. In the next chapter we describe our computer simulation of the equations of motion.

III. DESCRIPTION OF THE SIMULATION

A. INTRODUCTION

In this chapter we describe the method of solution employed in this report to compute the wave induced perturbations of the energetic particles. The approach used is a test particle simulation of the wave particle interaction. The perturbation of a full particle distribution is calculated by considering the effect of the wave on a sufficiently large number of test particles that are appropriately distributed in the phase space. With this point of view the problem becomes one of classical Newtonian mechanics. Namely, given a wave structure, the task is to simulate the equations of motion for the individual test particles. With the computer simulation approach it is possible to use the full equations of motion and to test quantitatively the relative importance of different terms. The need for restrictive simplifying assumptions is also greatly reduced.

The modeling of a full particle distribution is described in Chapter 5. In this chapter we describe in detail the computation of the trajectory of a given particle in the distribution.

A simplified version of the computer program used in our calculation are given in Appendix D. In the following we describe the general formulation of the problem.

B. COMPUTATION OF THE MEDIUM PARAMETERS

The computer simulation employs a centered dipole model for the static magnetic field described by Eq. (2.1) and a diffusive equilibrium model described by Eq. (2.4) for the cold plasma density. The computa-

tion of the medium parameters is separated from the simulation of the interaction. For this reason any other cold plasma model can be used without difficulty.

The necessary input to this portion of the program consists of wave frequency ω , specification of the field line by its L value and the equatorial cold plasma density n_{eq} , on that line. Another input is a latitude range, YLAMAX, which defines the portion of the field line within which the calculation is to be limited. For any given parameters a value of YLAMAX can be found such that for gyroresonant interactions at latitudes greater than YLAMAX the particle perturbations are negligible or below the resolution of the computations. The simulation is then limited to within \pm YLAMAX of the equator. Another input to this portion of the program is an integer value M. This value specifies the number of grid points that is to be taken along one half of the field line. With these inputs specified the program then computes ω_H , ω_p and k and stores the values $\omega_H(z)$ and $k(z)$ at M points equally spaced in latitude between -YLAMAX and zero degrees (equator) latitude. This is illustrated in Fig. 3.1. Hence, the output of this portion of the program is M triplets z , $\omega_H(z)$ and $k(z)$, where z is the distance along the field line as measured from the equator. Typical values used in our calculations are $YLAMAX = 20^\circ$ and $M = 10,000$.

These stored values of $\omega_H(z)$ and $k(z)$ are used later during the integration of the motion equations.

C. MAIN SIMULATION

Test particle identification

In a test particle simulation each particle must be identified with

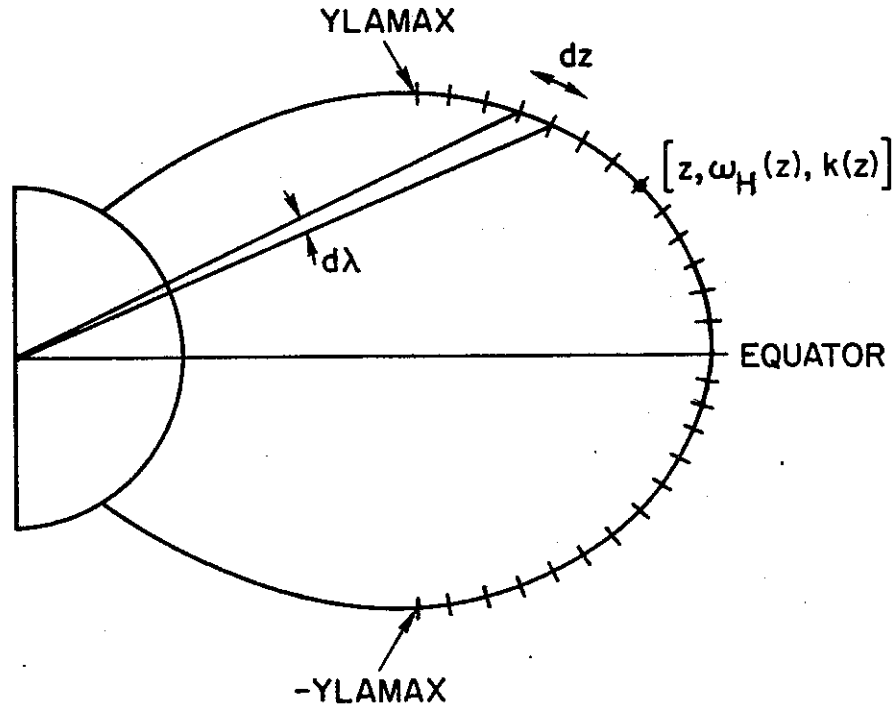


FIGURE 3.1 COMPUTATION OF THE MEDIUM. The portion of the field line to which the computation is limited is divided into mesh points equally spaced in latitude. For every mesh point the triplet $z, \omega_H(z)$ and $k(z)$ is stored for use in the integration of the motion equations.

a set of unique parameters. For adiabatically trapped particles the equatorial pitch angle, α_{eq} , and equatorial parallel velocity $v_{\parallel eq}$ are one such set of quantities. Using the first adiabatic invariant (Eq. (2.7)) the local pitch angle α and parallel velocity v_{\parallel} at any other point $z = z_0$ can be readily obtained from α_{eq} and $v_{\parallel eq}$.

$$\sin \alpha = \sqrt{\frac{B(z_0)}{B_{eq}}} \sin \alpha_{eq} \quad (3.1)$$

$$v_{\parallel} = \sqrt{\frac{B(z_0)}{B_{eq}}} v_{\parallel eq} \frac{\tan \alpha_{eq}}{\tan \alpha} \quad (3.2)$$

where B_{eq} and $B(z_0)$ represent the equatorial and local values of the static magnetic field respectively.

In the absence of the wave a test particle described by α_{eq_0} and $v_{\parallel eq_0}$ will acquire the local pitch angle and parallel velocity as given by (3.1) and (3.2) as it moves along the field line. Significant cumulative interaction between the wave and the particle will occur only in the vicinity of the point where $v_{\parallel} \approx v_R$, v_R being the local resonant velocity, given by $v_R = \frac{\omega_H - \omega}{k}$. As indicated in Fig. 3.2a this condition will be satisfied in the vicinity of two locations along the field line, owing to the symmetry of the dipole field. Since the wave induced perturbations will be negligible outside these regions, the particle motion at locations other than these can still be described by (3.1) and (3.2). The encounter with the wave modifies the local v_{\parallel} and α , and through (3.1) and (3.2), the equatorial parameters α_{eq} and $v_{\parallel eq}$ to be associated with that particle.

Complete interaction

For a monochromatic CW signal traveling from south to north as shown in Fig. 3.2a, the complete interaction of each particle with the wave can be described as follows. As the particle travels south toward its point of resonance in the northern hemisphere the wave induced perturbations become more and more significant. When the particle moves past its resonance point after having been scattered in α_{eq} and $v_{\parallel eq}$ the perturbations get smaller until it reaches the equator. Past the

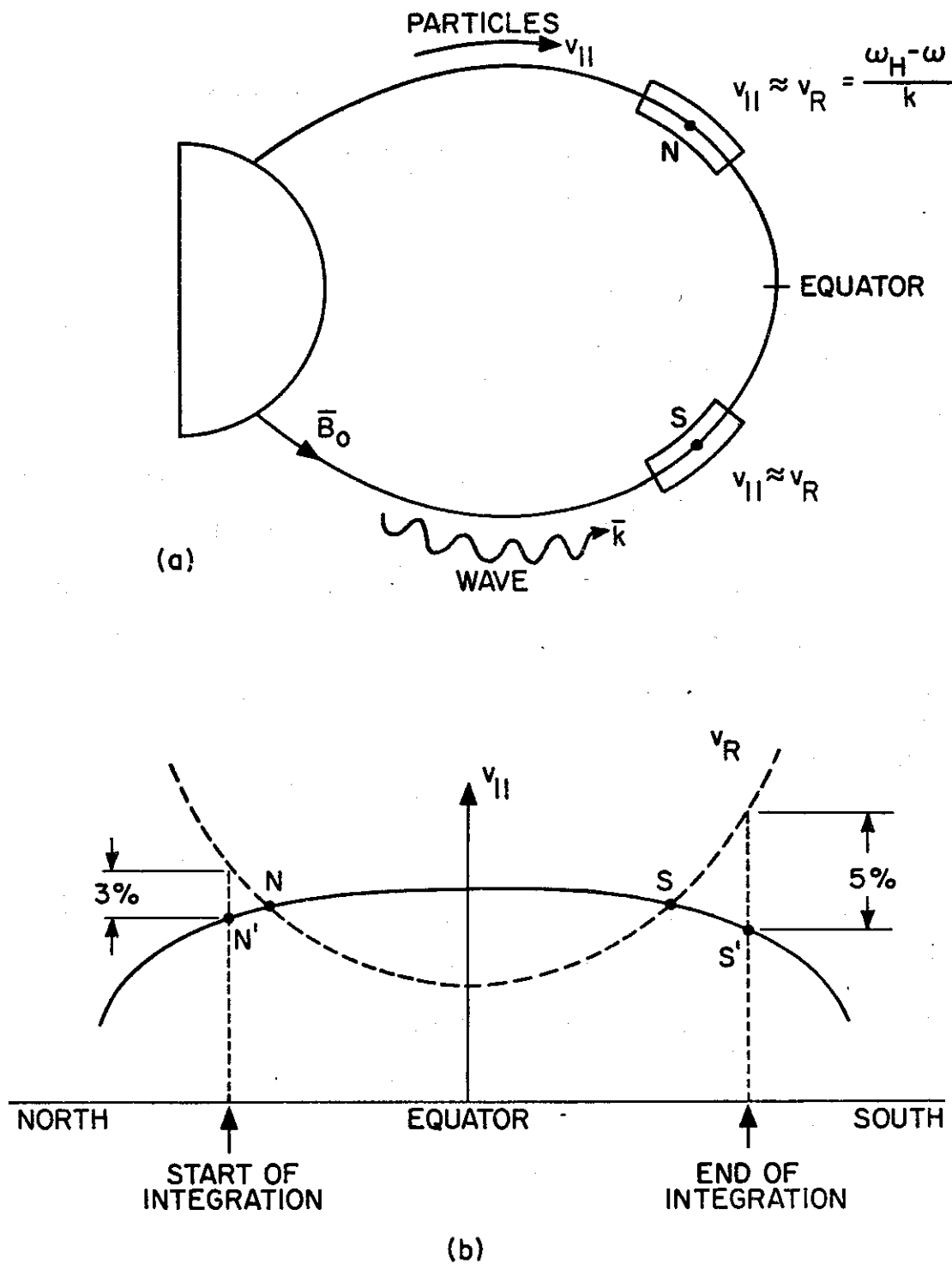


FIGURE 3.2 COMPLETE INTERACTION OF THE WAVE AND A TEST PARTICLE. (a) In general, the cyclotron resonance condition (2.30) will be satisfied at two locations N and S along the field line. (b) Adiabatic variation of the particle parallel velocity with distance from the equator. Shown in dotted lines is the resonance velocity v_R . The integration of the equations of motion is started at point N' and ended at S' for the simulation of the complete interaction.

equator, the particle approaches its second resonant point and is scattered again. Depending on the distance between the two resonance points the two encounters with the wave may or may not be in phase with each other.

To simulate this complete interaction, the equations of motion must be integrated from the time the particle is close enough (usually within 2-3% in v_{\parallel}) to its first resonance point to experience significant perturbations to the time at which the particle has passed significantly beyond its second resonance point so that the wave perturbations become insignificant. To continue the integration outside the resonance region would be useless since the changes in α_{eq} or $v_{\parallel eq}$ are negligible.

Figure 3.2b shows the adiabatic variation of the particle parallel velocity along the field line. Shown in dotted lines is the local resonance velocity v_R . The input to the main simulation part of the program is a set of values α_{eq_0} , $v_{\parallel eq_0}$ and an initial phase ϕ_0 . With these parameters specified, the program transfers α_{eq} and $v_{\parallel eq}$ into local values α and v_{\parallel} using (3.1) and (3.2), going progressively away from the equator, and at each point checking $|v_{\parallel} - v_R|$ in order to locate the vicinity of the resonance point N. The integration is started at a point where v_{\parallel} is within some percentage of the resonance velocity of the northern resonance point. We have found that when the particle is more than 3% or so away from local resonance the wave induced perturbations are not significant. This value is used in our computations as indicated in Fig. 3.2b.

The motion equations are integrated using spatial steps as opposed to temporal steps. The step size used for integration is a fraction of

the step size used for the computation of the medium parameters $\omega_H(z)$ and $k(z)$, so that these stored values can be used during the integration either directly or by linear interpolation between two adjacent values. This procedure allows us to avoid the computation of the medium and wave related quantities separately for each test particle. The integration is carried out until the time where $\epsilon = \left| \frac{v_{\parallel} - v_R}{v_R} \right| > 0.05$ and $d\phi > 2\pi$. Both these criteria are very conservative and were established by examining single particle trajectories. If the complete interaction is to be simulated, the integration is carried out until the particle passes its resonance point S in the southern hemisphere even if ϵ gets to be greater than 0.05 in between its first and second resonances.

At the end of the integration the local pitch angle α_F (F for final) and parallel velocity $v_{\parallel F}$ at the point where the integration is stopped is found. These values are then transformed through (3.1) and (3.2) to equatorial values α_{eq_F} and v_{eq_F} for that particle. The difference $\alpha_{eq_F} - \alpha_{eq_0} = \Delta\alpha_{eq}$ gives the total pitch angle scattering suffered by the particle.

Figure 3.3a,b shows sample trajectories of two particles both with $\alpha_{eq_0} = 7^\circ$, but (a) $v_{\parallel eq_0}$ is such that it resonates in the vicinity of $\pm 1^\circ$ latitude, and (b) $v_{\parallel eq}$ is such that it resonates in the vicinity of $\pm 3^\circ$ latitude.

We have shown equatorial pitch angle α_{eq} , and the off resonance factor ϵ versus time and latitude along the field line. It is clear that as the particle approaches resonance the wave induced pitch angle changes become more and more cumulative. Note that for $B_w = 0$, α_{eq} is constant with distance along the field line. As the particle moves away

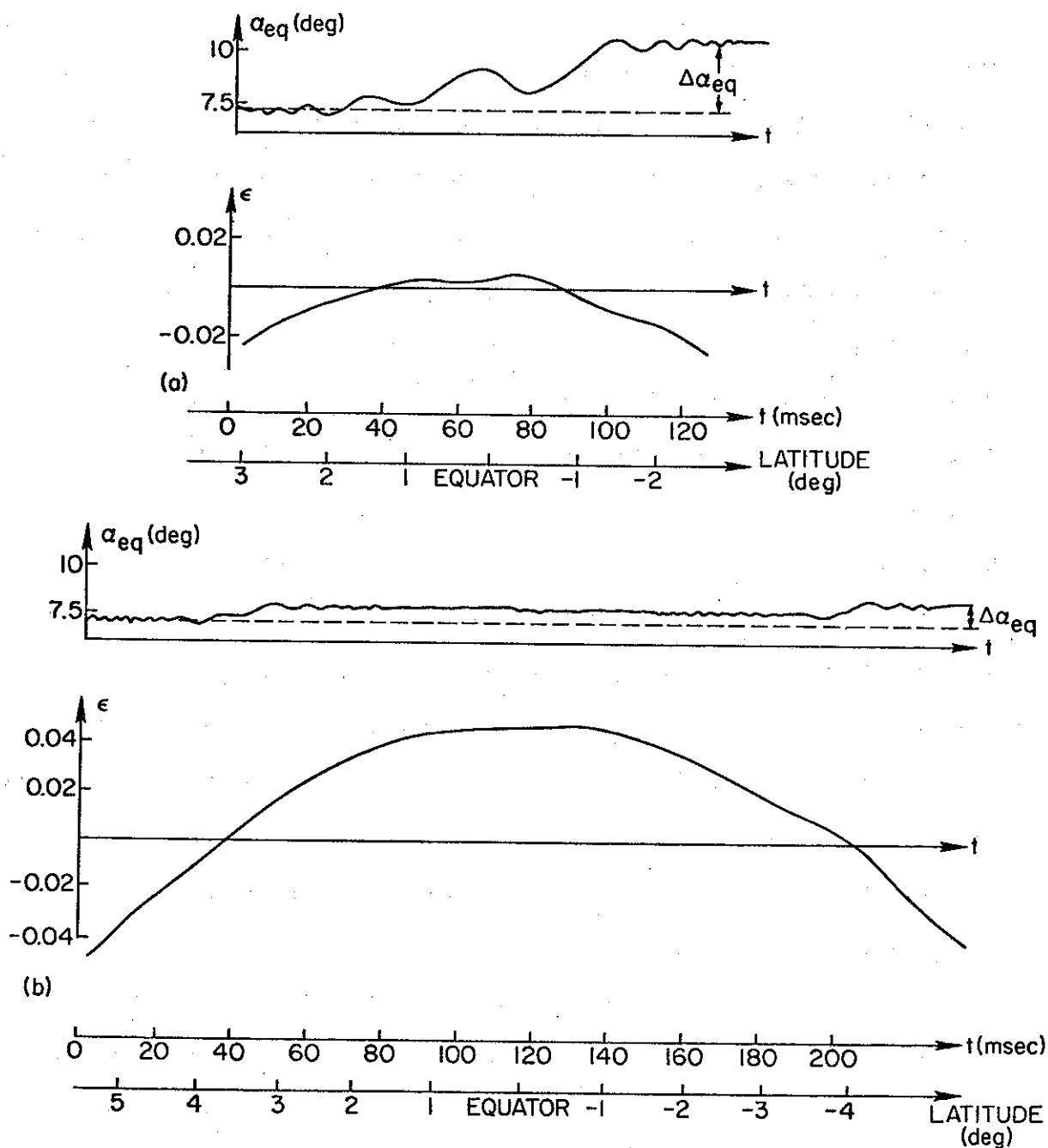


FIGURE 3.3 SAMPLE PARTICLE TRAJECTORIES. Both equatorial pitch angle α_{eq} and off resonance factor $\epsilon = \left| \frac{v_{||} - v_R}{v_R} \right|$ is shown. (a) $\alpha_{eq0} = 7^\circ$, $v_{||eq0}$ such that it resonates at $\pm 1^\circ$ latitude. (b) a particle with $\alpha_{eq0} = 7^\circ$, $v_{||eq0}$ such that it resonates at approximately $\pm 3.5^\circ$.

from resonance the changes in α_{eq} become noncumulative. Note that at the end of the interaction the particle has attained a new pitch angle

α_{eq_F} .

In addition to simulating the complete interaction of each test particle with the wave, as is necessary for the full distribution computations, the computer code can also be used for studies of different portions of the interaction. This is done in the next chapter where we study the scattering of particles that are initially resonant with the wave at the equator.

IV. STUDY OF THE INTERACTION

A. SCATTERING OF A SINGLE RESONANT SHEET

Our purpose in this section is to give a clear presentation of the different aspects of the physics of the nonlinear gyroresonance interaction.

Although the full distribution calculations give useful measurable quantities, such as the precipitated flux, they are not very helpful in understanding the physics of the interaction. The behavior of single particles and sheets provides much better insight, clarifying the effect of various parameters such as B_w , α_{eq} , n_{eq} , L , and initial phase, ϕ_0 . We study the case of a sheet of electrons, uniformly distributed in ϕ and moving away from the equator. The interaction starts at the equator as depicted in Fig. 4.1. The use of initially resonant sheets enables us to present clearly the initial phase dependence. The equator is chosen because the inhomogeneity there is a minimum, thus enabling us to see the effect of the wave forces to their full extent. We must emphasize at this point that this choice is made only to simplify the presentation and not the physics. The physics, i.e. the effect and relative importance of different parameters, is unaffected. In a distribution of particles interacting with a wave at any instant of time, there will be particles with many values of α_{eq} and $v_{||eq}$ located at all points along the field line. In our presentation of the single sheet results, we look at a sheet of electrons that meets the wave at the equator with specified α_{eq} and $v_{||eq}$ values. The results are qualitatively representative of those for most other sheets in the distribution, although the amount of scattering will in general be smaller for interactions

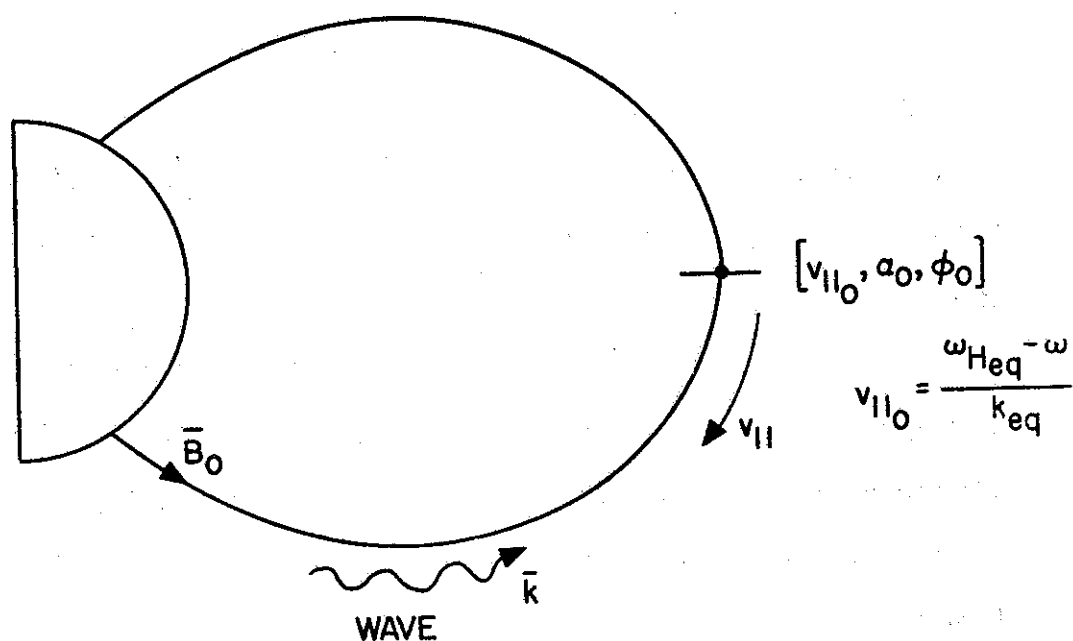


FIGURE 4.1 DESCRIPTION OF THE INTERACTION STUDIED IN THIS SECTION.
Single particles or sheets of particles that are resonant at the equator are considered.

away from the equator or for non-resonant sheets.

The parameter values used for most of our calculations are given in Table 1; they represent a realistic magnetospheric case. $L = 4$ is chosen because it is close to the location of the VLF transmitter at Siple, Antarctica, from which much of the experimental data have come. A wave frequency of 5 kHz is chosen, a frequency often used in the Siple wave injection experiments.

We first consider particles with an equatorial pitch angle $\alpha_{eq_0} = 10^\circ$ and a wave amplitude of $B_w = 10 \text{ m}\gamma$. Figure 4.2 shows the computed trajectories for six particles distributed in initial phase ϕ_0 . We

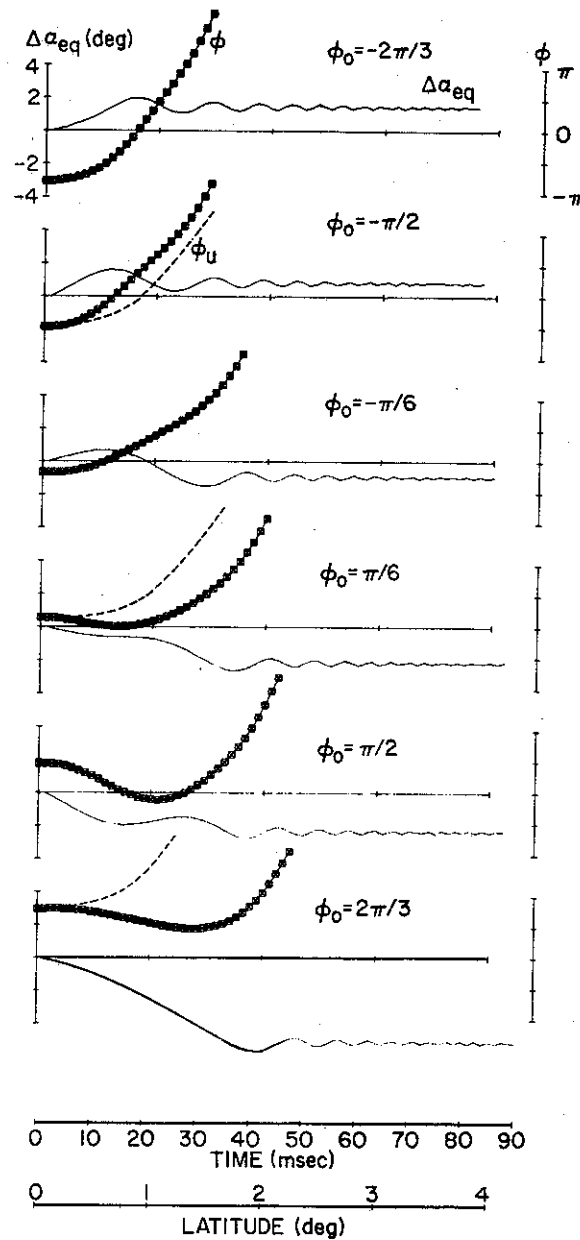


FIGURE 4.2 SINGLE PARTICLE TRAJECTORIES FOR $B_w = 10 m\gamma$. Both the total scattering $\Delta\alpha_{eq}$ (solid lines) and the phase ϕ (squared points) are shown as a function of time. All particles start at resonance at the equator (see Fig. 4.1) and move southward into the wave. Particle trajectories for 6 different initial phases are shown. The phases are chosen to illustrate typical trajectories. The dashed lines are the unperturbed phase (ϕ_u) variation for the case of $B_w = 0$. For all trajectories $\alpha_{eq} = 10^\circ$.

TABLE I. PARAMETER VALUES FOR THE EXAMPLE CASE

Field line	$L = 4$
Equatorial gyrofrequency	$f_{\text{Heq}} = 13.65 \text{ kHz}$
Equatorial cold plasma density	$n_{\text{eq}} = 400 \text{ el/cc}$
Wave frequency	$f = 5 \text{ kHz}$
Equatorial parallel resonance velocity	$v_{\text{uR}} = 1.899 \times 10^7 \text{ m/sec}$
Equatorial parallel resonant energy	$E \approx 1 \text{ keV}$
Refractive index at the equator	$n \approx 40$
Wavelength at the equator	$\lambda_w \approx 2.2 \text{ km}$

have plotted both $\Delta\alpha_{\text{eq}}$ and the phase ϕ at each step of the interaction. The resonant interaction starts at the equator for all particles.

Consider for example the particle with $\phi_0 = -2\pi/3$. As this particle moves away from the equator it suffers a positive $\Delta\alpha_{\text{eq}}$, and as $\dot{\phi}$ increases (the particle gyrating faster with respect to the wave) the changes in $\Delta\alpha_{\text{eq}}$ become smaller and smaller. Eventually the oscillations become insignificant and the particle leaves the interaction region with a net change in equatorial pitch angle. Note that α_{eq} of each of the six particles in Fig. 4.2 can be considered unaffected by the wave after about 70 msec (3° latitude). Beyond this point the wave induced particle scatterings are not cumulative.

Also shown in Fig. 4.2 is the unperturbed phase variation ϕ_u (i.e. the phase variation for negligible wave intensity) for some initial phases. The ϕ_u variation for other phases is exactly the same in form

but shifted up or down depending on ϕ_0 (see section 2.F).

For particles starting at resonance (i.e. v_{\parallel} satisfies Eq. (2.30)) $\dot{\phi}_0 \approx 0$. For $B_w \approx 0$, as the particle moves away from the equator ω_H increases, therefore increasing $\dot{\phi}$, which causes ϕ to increase as seen from the ϕ_u variation in Fig. 4.2. In other words, $\ddot{\phi}_0 = \ddot{\phi}_u > 0$. For $B_w \neq 0$ the interaction can be studied qualitatively as follows:

1) For negative ϕ_0 , $\dot{v}_{\parallel 0} < 0$. (See Eq. (2.36a).) Hence v_{\parallel} decreases while ω_H increases as the particles move away from the equator. Therefore $\ddot{\phi}_0 > \ddot{\phi}_u$ and the time for which the particle stays within resonance is shortened. Also since the initial wave induced \dot{v}_{\parallel} is negative, the local pitch angle of the particle increases, which in turn through (3.1) transforms into an increase in the equatorial pitch angle. As ϕ increases to the point where $\sin\phi$ changes sign (in this case becomes positive) \dot{v}_{\parallel} becomes positive and tends to decrease ϕ . Since ω_H keeps increasing, the wave forces offset the effects of the inhomogeneity at this stage of the interaction. However, there already is a large $\dot{\phi}$ and the particle is no longer near resonance. Therefore if the wave amplitude is not strong enough to cause an oscillation (or reversal) in phase (i.e. trapping) the phase angle ϕ continues to increase. When ϕ comes to the point where $\sin\phi$ again changes sign, \dot{v}_{\parallel} again becomes negative. The periodic changes of sign of \dot{v}_{\parallel} lead to oscillations in $\Delta\alpha_{eq}$. This behavior is most clearly illustrated by the case of larger wave amplitudes, as in Fig. 4.3. Since ω_H continuously increases as the particle moves away from the equator the period of these oscillations decreases as the particle moves away from resonance. Eventually the particle acquires a net pitch angle change $\Delta\alpha_{eq}$. Typical trajectories

for the negative initial phase case are shown in Fig. 4.2.

2) For positive ϕ_0 , $\dot{v}_{\parallel 0} > 0$, and the wave forces offset the effects of the inhomogeneity. Therefore $\ddot{\phi} < \ddot{\phi}_u$ and the time during which particle stays within resonance is increased, hence allowing more scattering due to more exposure to cumulative interaction. For the case of $B_w = 10 m\gamma$, given in Fig. 4.2, we see that final scatterings for $\phi_0 > 0$ are generally larger than those for $\phi_0 < 0$, although the final scattering depends, as we shall later see, on a wide variety of parameters. Note in Fig. 4.2 that although the initial \dot{v}_{\parallel} is a maximum for $\phi_0 = \pi/2$, the final scattering is the largest for $\phi_0 = 2\pi/3$. This occurs because for $\phi_0 = 2\pi/3$ the wave and inhomogeneity forces balance each other over a longer distance and hence $\ddot{\phi}$ stays very close to zero, therefore increasing the time spent within resonance.

For an initial pitch angle of 10° , a wave amplitude of $10 m\gamma$ is not large enough to cause more than one oscillation in phase ϕ . That is, it cannot trap the particles for long in the wave's potential well. In Fig. 4.3 we give the trajectories of seven particles for $B_w = 50 m\gamma$. In comparing Figs. 4.2 and 4.3 we make the following observations:

1) The oscillations in $\Delta\alpha_{eq}$ as the particle moves away from resonance are larger in amplitude for $B_w = 50 m\gamma$ than for $B_w = 10 m\gamma$. This is expected since the scattering at each point is proportional to B_w .

2) For some of the phases ($\phi_0 = -\pi/2, -\pi/3, 0, \pi/3$) the particle phase $\phi(t)$ makes more than one oscillation. Hence the particle is phase trapped, although only for a short while. The most strongly trapped particle is the one with $\phi_0 = 0$.

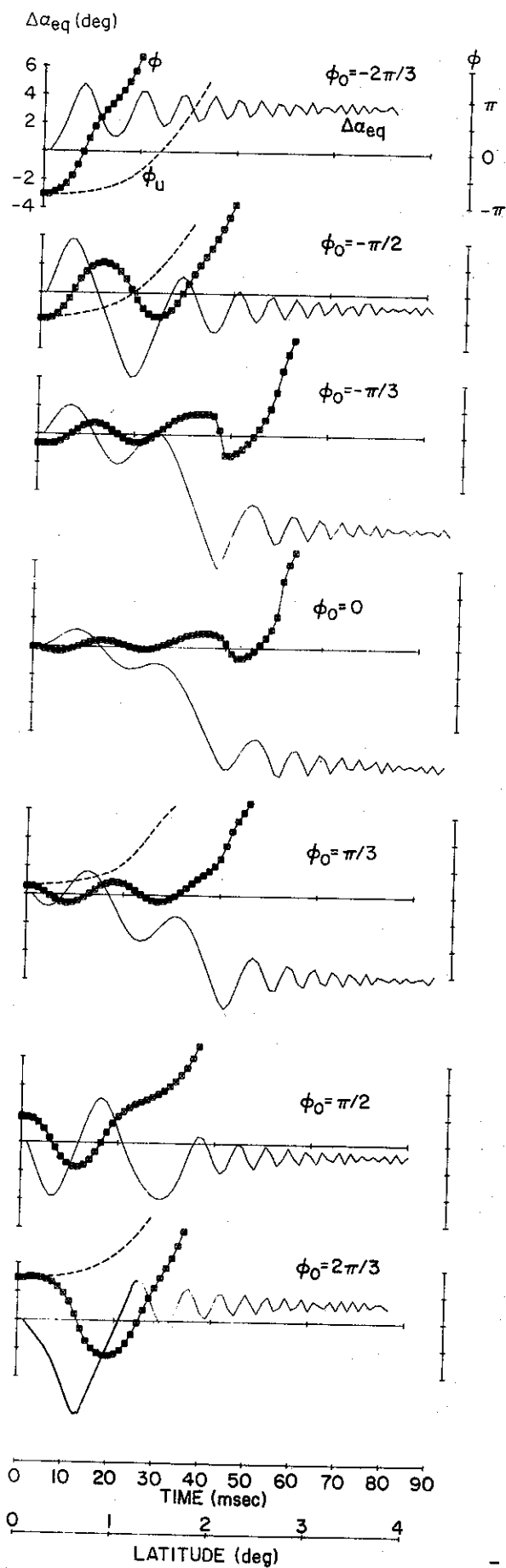


FIGURE 4.3 SINGLE PARTICLE TRAJEC-
TORIES FOR $B_w = 50 m\gamma$.
The format is the same as Fig. 4.2.
For all trajectories, $\alpha_{eq_0} = 10^\circ$.

3) All the trapped particles end up with a negative $\Delta\alpha_{eq}$. This is because for trapped particles $v_{\parallel} \approx v_R = \frac{\omega_H - \omega}{k}$ and $\dot{v}_{\parallel} \approx \dot{v}_R$. Since $\dot{v}_R > 0$ when moving southward from the equator, $\dot{v}_{\parallel} > 0$ and, from Eq. (2.36b), $\dot{v}_{\perp} < 0$. Thus the pitch angle must decrease for all trapped particles as they move away from the equator.

4) Consider the trajectory for the $\phi_0 = -\pi/3$ particle. The second minimum of $\Delta\alpha_{eq}$ (at $t \approx 43$ ms) seems much sharper than for other cases. Note that the particles shown in Fig. 4.3 have an equatorial pitch angle of $\alpha_{eq} = 10^\circ$. The second minimum in $\Delta\alpha_{eq}$ for $\phi_0 = -\pi/3$ is at about $\Delta\alpha_{eq} = 9.5^\circ$. In other words, as the pitch angle continuously decreases it has reached a point where it is very close to zero. At those low pitch angles v_{\perp} is very small and therefore the wave term ($\propto \frac{\cos\phi}{v_{\perp}}$) in Eq. (2.36c) becomes significant, causing a large change in phase which prevents the pitch angle from reaching zero. This effect is called the 'loss cone reflection' effect and is discussed in Appendix B. This example shows the importance of not deleting this term in the computations. Without this term the pitch angle would have gone negative. At the third minimum of $\Delta\alpha_{eq}$ for $\phi_0 = 0$ we have the same effect, again clearly seen by an abrupt change in ϕ .

After this discussion of the single particle trajectories, it is further enlightening to study the collective motions of sheets of particles. As our tool for this study we consider the variation of the final scattering $\Delta\alpha_{eq}$ versus initial phase. We have found that the nature of the interaction and the effects of different parameters are most clearly presented in such a format. Below, we give results of our computations for a sheet of 24 electrons equally distributed in initial

phase ϕ_0 . We consider different cases to isolate the effects of parameters such as B_w , α_{eq} , n_{eq} , position of resonance, etc. The results are obtained by integrating the full equations of motion for each of the 24 electrons in the sheet to obtain the total final scattering $\Delta\alpha_{eq}$. We then plot $\Delta\alpha_{eq}$ vs. initial phase ϕ_0 , and discuss each result qualitatively.

a) Effect of the Wave Amplitude

Figure 4.4a shows $\Delta\alpha_{eq}$ vs. ϕ_0 for the parameters as given in Table 1 and for $\alpha_{eq_0} = 10^\circ$. We have given results for a range of wave amplitudes from $B_w = 1 m_Y$ to $B_w = 50 m_Y$. For low wave amplitudes such as $B_w = 1 m_Y$ and $3 m_Y$ we have 'linear' scattering. In other words, for these cases the inhomogeneity is the dominant factor in controlling $\phi(t)$ rather than the wave forces. Therefore $\phi(t) \approx \phi_u(t)$ and linear theory can be applied. That the shape of the $\Delta\alpha_{eq}$ vs. ϕ_0 curves is approximately sinusoidal for these cases is shown in Appendix A. In the rest of this report the interaction will be termed to be in the 'linear' mode whenever $\Delta\alpha_{eq}$ vs. ϕ_0 is approximately sinusoidal.

For $B_w > 7 m_Y$ the curves start to change shape. For $B_w = 50 m_Y$ we have what we call the 'trapped' mode. The trapped mode is one in which the wave forces play the dominant role in controlling $\ddot{\phi}$. The phase ϕ in this case goes through more than one oscillation due to sign changes of $\ddot{\phi}$. As discussed above in connection with Fig. 4.3 the trapped particles end up with a net negative change in pitch angle, thus producing a $\Delta\alpha_{eq}$ vs. ϕ_0 variation as shown in Fig. 4.4a for the $B_w = 50 m_Y$ case. Note that only particles in a range around $\phi_0 = 0$ are trapped, the initial phases of other particles are not appropriate

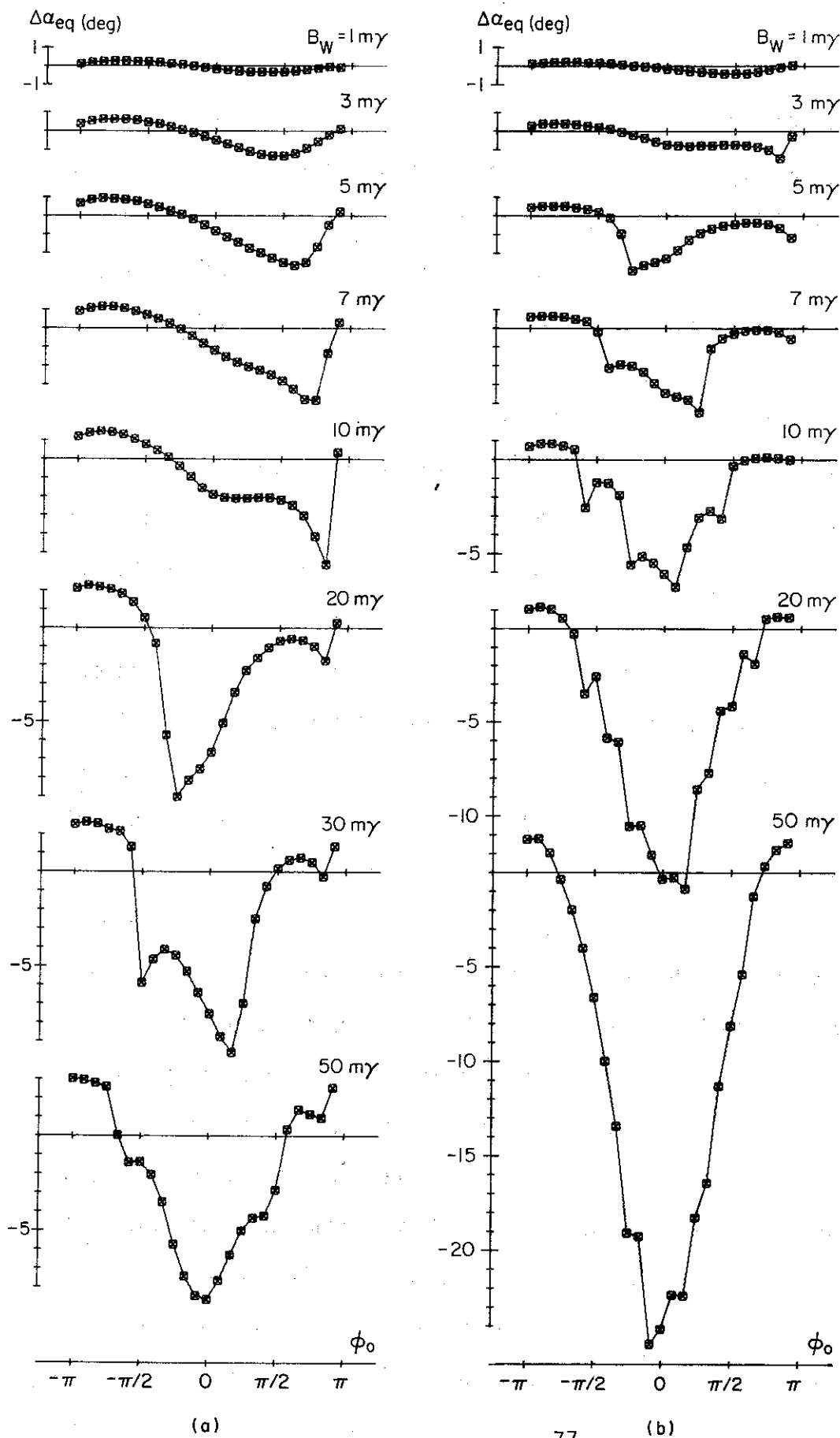


FIGURE 4.4 TOTAL SCATTERING, $\Delta\alpha_{eq}$, VERSUS INITIAL PHASE FOR DIFFERENT WAVE AMPLITUDES, FOR $L = 4$ AND $n_{eq} = 400 \text{ el/cc}$. (a) $\alpha_{eq0} = 10^\circ$. (b) $\alpha_{eq0} = 30^\circ$. Each square in the figures shows the scattering of an individual test particle. 24 particles, uniformly distributed in ϕ_0 , are used in each sheet.

for trapping. This is also seen in Fig. 4.3.

Figure 4.4 gives only the final net scatterings. No time parameter is involved. For each case, the equations have been integrated for each electron in the sheet until the particle is no longer significantly affected by the wave. The total pitch angle change $\Delta\alpha_{eq}$ is then plotted against ϕ_0 . Note that for $7 m\gamma < B_w < 50 m\gamma$ the $\Delta\alpha$ vs ϕ_0 curves resemble neither the linear nor the trapped mode. This is because for these transition values neither the wave force nor the inhomogeneity is clearly dominant. For $B_w = 3 m\gamma$ and $5 m\gamma$ we observe from Fig. 4.4a that there is an asymmetry between scattering for negative and positive initial phases. This comes about because, although for all ϕ_0 the inhomogeneity is the dominant factor, for positive ϕ_0 the wave forces offset the effects of the inhomogeneity whereas for negative ϕ_0 the wave force adds to the effect of the inhomogeneity. Therefore for positive ϕ_0 the particle stays in resonance for a longer time and hence experiences larger scattering.

For $B_w = 50 m\gamma$ Fig. 4.4 shows that the maximum negative scattering for $\alpha_{eq_0} = 10^\circ$ is about $\Delta\alpha_{eq} = 9^\circ$. Thus the absolute pitch angle for these particles is reduced nearly to zero. Similarly for $\alpha_{eq} = 30^\circ$ the maximum negative scattering is 24° , bringing this particle to the edge of the loss cone.

One important point that must be kept in mind is the following: Figure 4.4a shows results for a single sheet traveling away from the equator. Consider the case of a sheet traveling towards the equator.

By studying Eq. (2.36c) we see that $\Delta\alpha_{eq}$ vs. ϕ_0 variations would be approximately a mirror image of the result for the $B_w = 50 m\gamma$, with the trapped particles having a net positive pitch angle change. Therefore one should not try to make predictions about the precipitated flux or other full distribution quantities using only these results. The single sheet results given in this section are intended only as an aid to understanding the interaction, and sorting out the dependence of $\Delta\alpha_{eq}$ on various parameters.

For higher α_{eq_0} , one would expect the deviation from the linear mode to start at lower amplitudes. In Fig. 4.4b we show the results for $\alpha_{eq_0} = 30^\circ$ in the same format as Fig. 4.4a. We see that the case of $B_w = 3 m\gamma$ is as much away from the linear mode as the case of $B_w = 10 m\gamma$ for $\alpha_{eq_0} = 10^\circ$. This is explained by the fact that the wave induced $\dot{v}_{||}$ is proportional to $v_{\perp} B_w$, and therefore to $\tan\alpha_{eq_0}$. As B_w is increased further we again have a similar kind of transition to the trapped mode. However the minima of $\Delta\alpha_{eq}$ are much deeper than the $\alpha_{eq_0} = 10^\circ$ case. For $B_w = 50 m\gamma$, for example, the most stably trapped particle ($\phi_0 = 0$) undergoes a net scattering of almost 24° . The behavior in Figs. 4.2, 4.3 and 4.4a,b also clearly shows the difference between coherent and incoherent interactions. In the coherent interaction the particle can be phase locked with the wave and lost almost all of its perpendicular energy in a single encounter with the wave. On the contrary, in an incoherent interaction, the scatterings suffered by the particle at each instant are random in direction and magnitude. As a result the particles execute a random walk in pitch angle space and a diffusion in the average direction of the field results. Therefore the

net total scatterings at each encounter with the wave are generally much smaller.

b) Comparison with the Linear Theory

At this point we are ready to compare quantitatively the results of our full analysis with those of linear theory. For purposes of comparison we have arranged our computer program to integrate the motion equations using linear theory if desired. Figure 4.5 shows a comparison of the linear and nonlinear analyses for $\alpha_{eq} = 10^\circ$. For the linear case the $\Delta\alpha_{eq}$ vs. ϕ_0 variation is proportional to $B_w \sin(\phi_0 + \beta)$, where β is defined in Appendix A. We see from Fig. 4.5 that the difference between the linear and the nonlinear results becomes apparent for $B_w \gtrsim 5 m_Y$. Even for $B_w = 3 m_Y$ the asymmetry between the scatterings for positive and negative ϕ_0 is apparent for the nonlinear case. Note that for higher α_{eq_0} the deviation from linear theory occurs at lower wave intensities. For instance, for $\alpha_{eq_0} = 30^\circ$ and $B_w = 3 m_Y$ the interaction is clearly nonlinear as can be seen from Fig. 4.4b. Note also that for the linear case the phase variation is the same for all 24 particles in the sheet. Therefore they all spend the same amount of time in resonance.

Figure 4.6a,b compares the linear and nonlinear root mean square scattering (i.e. $\sqrt{\langle \Delta\alpha^2 \rangle}$ where $\langle \rangle$ denotes averaging over the initial phases) and the mean value (i.e. $\langle \Delta\alpha \rangle$) of the $\Delta\alpha_{eq}$ vs. ϕ_0 curves for both $\alpha_{eq_0} = 10^\circ$ and 30° cases. We see that as the wave amplitude is increased there is an increasing mean value for the nonlinear cases whereas the mean value for the linear case is zero for all wave amplitudes. For $\alpha_{eq_0} = 10^\circ$ and for small wave fields of up to $5 m_Y$ the rms scattering for both cases is about the same. However as the wave amplitude

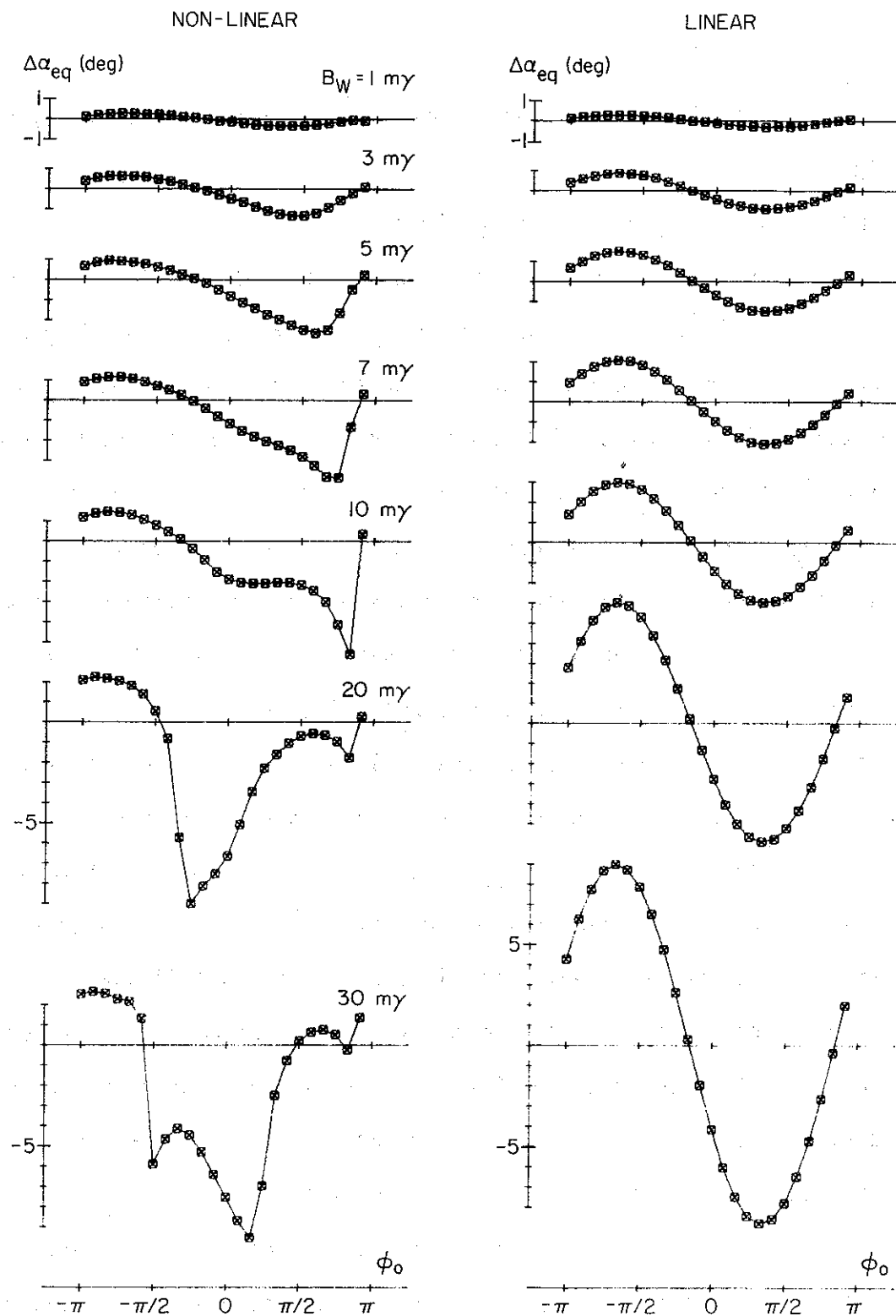


FIGURE 4.5 COMPARISON OF RESULTS OF LINEAR THEORY AND THE FULL NON-LINEAR ANALYSIS. The total scattering vs. ϕ_0 is given for $\alpha_{eq} = 10^\circ$ and for different wave amplitudes. The format is very similar to that of Fig. 4.4.

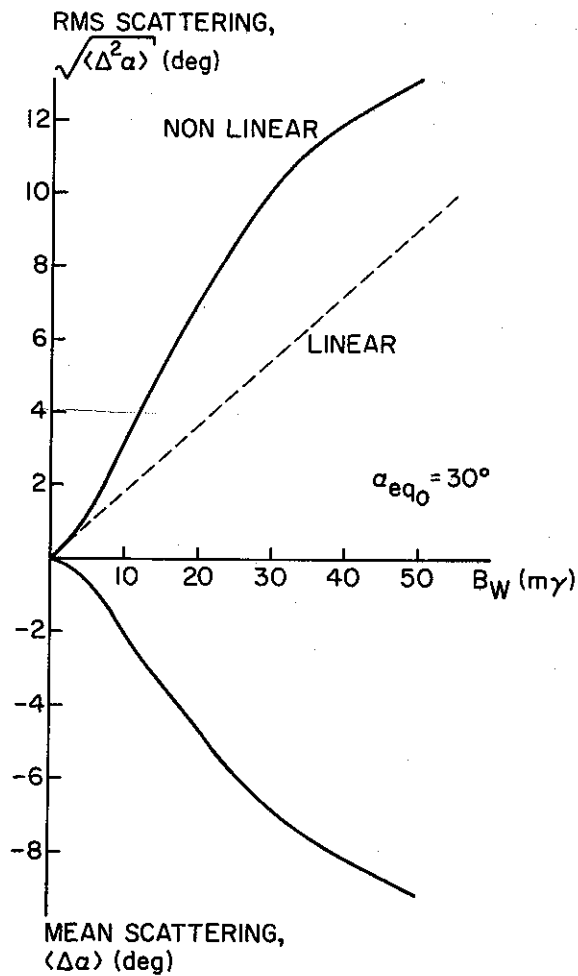
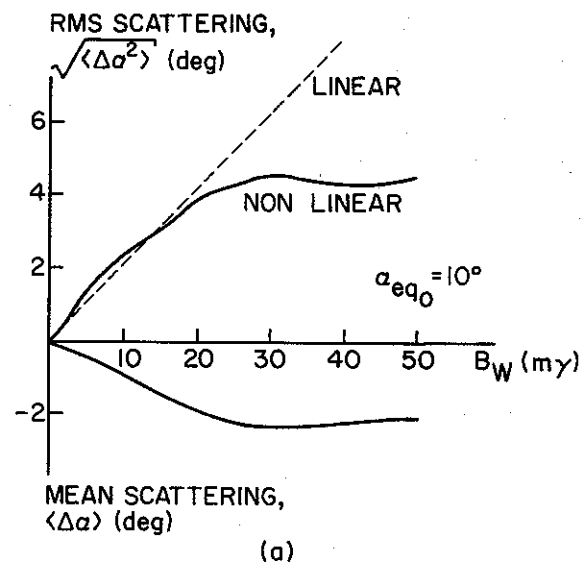


FIGURE 4.6 RMS AND MEAN SCATTERING FOR LINEAR AND NONLINEAR ANALYSES AS A FUNCTION OF WAVE AMPLITUDE. The mean scatterings for the linear case is zero. (a) $\alpha_{eq0} = 10^\circ$. (b) $\alpha_{eq0} = 30^\circ$.

is increased the rms scattering for the nonlinear case deviates from the linear case in which the rms scattering is directly proportional to B_w . Therefore the use of linear theory when $B_w > 3 m_Y$ causes an error in both mean and rms scatterings.

Since for $B_w \geq 40 m_Y$, $\Delta\alpha_{eq} \approx \alpha_{eq_0}$, the rms scattering saturates for the $\alpha_{eq_0} = 10^\circ$ case; however for the higher initial pitch angle ($\alpha_{eq_0} = 30^\circ$) case we see that the rms scattering is considerably larger than the linear one over a wide range of wave amplitudes. The scattering is larger because the nonlinear formulation takes particle trapping into account and this effect considerably increases the length of the interaction region over which scattering takes place.

Since the $\Delta\alpha_{eq}$ vs ϕ_0 curve for the linear case is found to have a sinusoidal shape (see Appendix A) it is possible to readily identify linear or trapped behavior by qualitatively examining the $\Delta\alpha_{eq}$ vs ϕ_0 curves. For example, for the case of Fig. 4.4a we see that deviation from a sinusoidal shape starts around $B_w = 5 m_Y$ and hence linear theory should be applicable only for $B_w < 5 m_Y$. In the following cases we shall use this concept to study our results.

c) Dependence on Equatorial Pitch Angle

To isolate the effect of the initial equatorial pitch angle we hold the wave amplitude constant at $B_w = 10 m_Y$ and for the parameters of Table 1 compute the scatterings for different α_{eq_0} . Figure 4.7 shows $\Delta\alpha_{eq}$ vs ϕ_0 curves parameterized in α_{eq_0} . A wide range of pitch angles $3^\circ \leq \alpha_{eq_0} \leq 85^\circ$ is covered. Since the wave induced \dot{v}_\parallel is proportional to v_\perp and hence to $\tan\alpha_{eq_0}$, for small enough pitch angles a linear $\Delta\alpha_{eq}$ vs ϕ_0 variation is expected. Indeed from Fig. 4.7 we

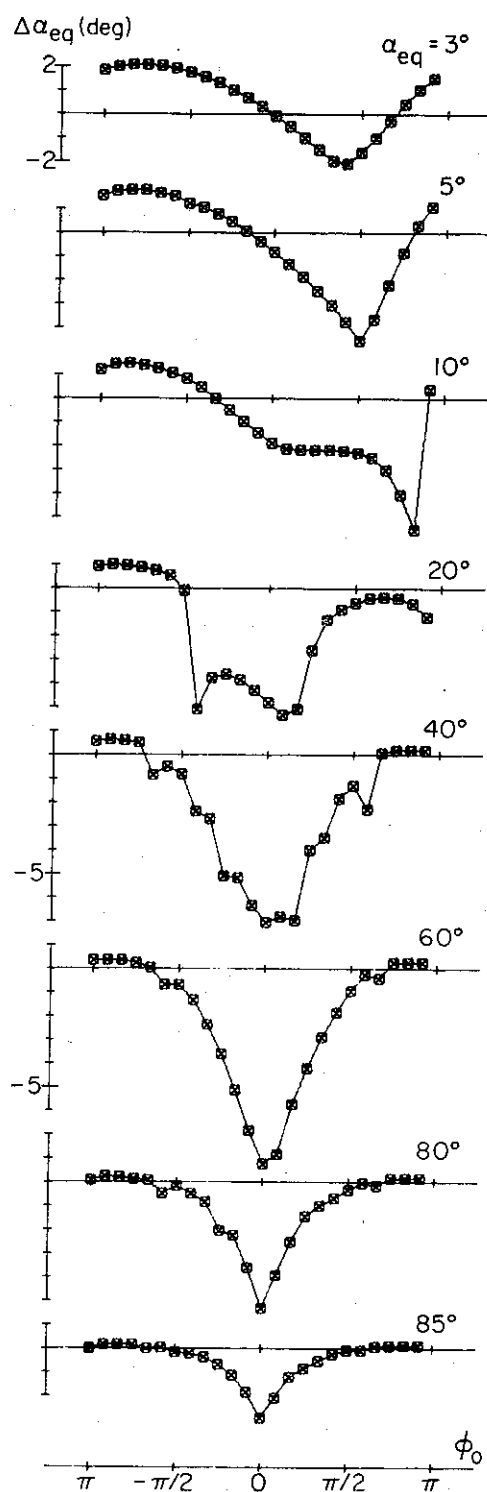


FIGURE 4.7 INITIAL PITCH ANGLE DEPENDENCE OF THE TOTAL SCATTERING VS. ϕ_0 FOR $n_{eq} = 400 \text{ e1/cc}$ AND $B_w = 10 \text{ m}\gamma$. The format is the same as that of Fig. 4.5.

see that the variation for $\alpha_{eq_0} = 3^\circ$ is essentially linear. The deviation from linearity increases as α_{eq_0} is increased and we have the trapped mode for $\alpha_{eq_0} > 40^\circ$. The transition from the linear to the trapped mode is similar to that shown in Fig. 4.4a.

For $\alpha_{eq_0} > 60^\circ$, the minimum of the $\Delta\alpha_{eq}$ vs. ϕ_0 curves starts to contract. Although the shape of $\Delta\alpha_{eq}$ vs. ϕ_0 stays in the trapped mode, the total scattering for each particle continuously decreases. The reason for this is that for these high values of α_{eq_0} the variation in the particles' v_{\parallel} and v_{\perp} due to the adiabatic mirror forces (second terms on the r.h.s. in Eqs. (2.36a,b) becomes more and more rapid, therefore decreasing the time spent in resonance and resulting in smaller scattering.

d) Dependence on the Equatorial Cold Plasma Density

One other parameter which defines the properties of the medium and the wave is n_{eq} , the equatorial cold plasma density. The wave number k is proportional to n_{eq} (see (2.25)). In Fig. 4.8 we give results for a $B_w = 50$ m γ wave and $\alpha_{eq_0} = 10^\circ$ particles at $L = 4$. We show $\Delta\alpha_{eq}$ vs. ϕ_0 curves for different n_{eq} values, ranging from 400 el/cc (inside the plasmopause) to 1 el/cc (outside the plasmopause).

Figure 4.8 shows that for $n_{eq} = 400$ el/cc a trapped mode exists. Decreasing n_{eq} results in a transition similar to those seen before, to a linear mode for $n_{eq} = 1$ el/cc. This result shows clearly that interactions outside the plasmopause result in less scattering than those inside the plasmopause. This interesting result can be understood as follows: As n_{eq} decreases the wave phase velocity increases and the parallel resonant velocity becomes higher. Higher energy particles move

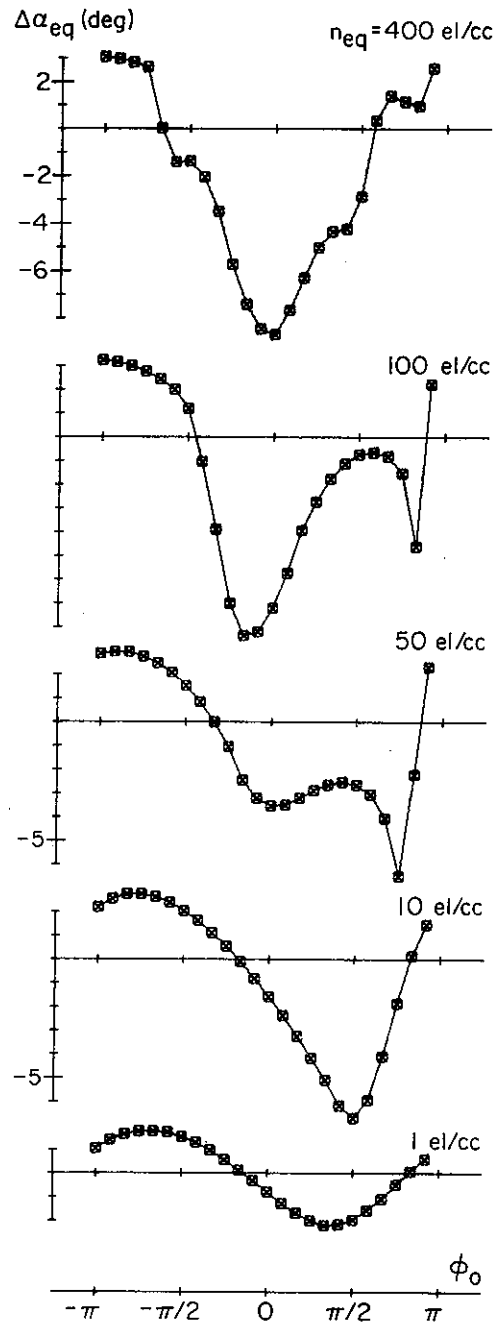


FIGURE 4.8 VARIATION OF TOTAL SCATTERING WITH EQUATORIAL COLD PLASMA DENSITY, n_{eq} . For all cases $L = 4$, $f = 5$ kHz, $B_w = 50$ mG, and $\alpha_{eq_0} = 10^\circ$. Note that for $n_{eq} = 1$ el/cc the parallel resonant particle velocity is in the relativistic range. We have not accounted for the relativistic correction in our calculation. However this correction will only vary the amplitude of the scattering. Our main concern in this section is the shape of the $\Delta\alpha_{eq}$ vs. ϕ_0 curves which will not be affected by that correction.

more quickly through the wave and hence have less time in which to be scattered. Note that although the equatorial parallel resonant energy is about 1 keV for $n_{eq} = 400$ el/cc it is approximately 40 keV for $n_{eq} = 10$ el/cc.

e) Dependence on the Geomagnetic Latitude Around Which the Resonance Occurs

Figure 4.9 shows $\Delta\alpha_{eq}$ vs. ϕ_0 for $B_w = 50$ m γ and $\alpha_{eq_0} = 10^\circ$. The curves in this case are parametric in the location of resonance. Hence the first sheet starts from the equator at resonance, the next starts at resonance at 2° latitude south of the equator and the last sheet starts at resonance at 10° latitude. All sheets travel southward away from the equator. We observe that for resonance at the equator we have a trapped mode, but as the resonance latitude is increased to 10° there is a transition to the linear mode. This is expected since the gradient of the earth's magnetic field increases with distance from the equator and for high enough latitudes the effects of inhomogeneity can no longer be offset by the wave forces. Because the inhomogeneity becomes the controlling factor at higher latitudes the shape of $\Delta\alpha_{eq}$ vs. ϕ_0 returns to the linear form. Note that this behavior is limited to constant frequency waves. For waves of changing frequency, maximum interaction may occur off the equator, as suggested by Helliwell [1967, 1970].

B. QUANTITATIVE CRITERIA FOR DETERMINING THE APPLICABILITY OF THE LINEAR THEORY

The linear theory procedure for computing the wave induced scatterings v_{\parallel} and v_{\perp} was described in section 2.F. A unique feature of

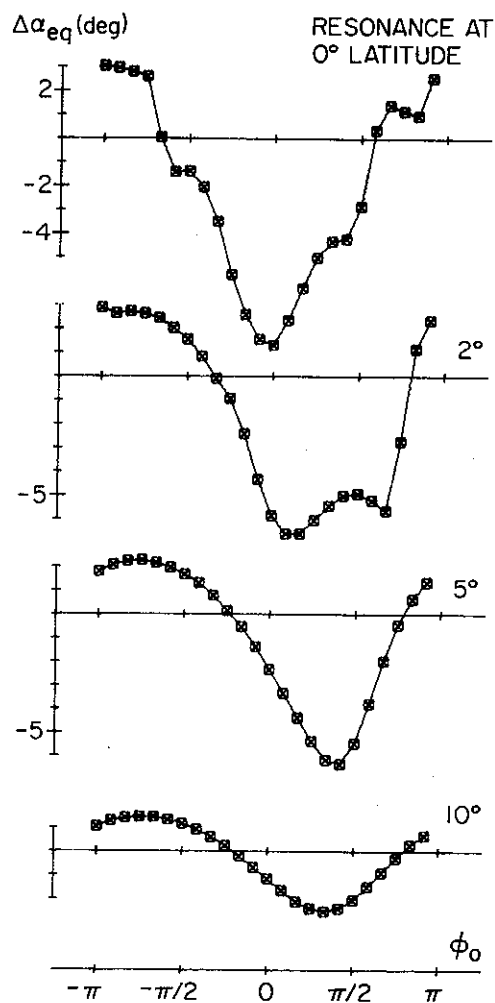


FIGURE 4.9 TOTAL SCATTERING AS A FUNCTION RESONANCE POINT ALONG THE FIELD LINE. For all cases, $L = 4$, $f = 5$ kHz, $B_w = 50$ mV, $\alpha_{eq_0} = 10^\circ$ and $n_{eq} = 400$ el/cc.

linear theory is that the path length over which resonance occurs is independent of wave amplitude. For instance if an electron is at resonance ($\phi=0$) with the wave at some point z_1 along the magnetic field line, linear theory predicts that resonance will effectively terminate at a point z_2 , defined implicitly by the approximate relation

$$\Delta\phi \approx 1 \text{ radian} \approx \int_{z_1}^{z_2} [\omega_H - \omega - kv_{\parallel}] \frac{dz}{v_R} \quad (4.1)$$

where ω_H is the electron gyrofrequency at the resonance point z_1 , and $v_R = \frac{\omega_H - \omega}{k}$. It can be seen that z_2 does not depend on B_w since in linear theory the wave induced changes in v_{\parallel} are ignored in integrating Eq. (2.36c). A rough method of establishing the validity of linear theory in any particular case involves the comparison of the time the particle spends in the linear resonance region $t_R = \frac{z_2 - z_1}{v_R}$, with the trapping time of the particle in the potential well of the wave, $t_T = 2\pi[(\frac{eB}{m})kv_{\parallel}]^{-1/2}$. When $t_R t_T^{-1} \ll 1$, it can be concluded that nonlinear effects will be negligible and that linear theory can be used, while if $t_R t_T^{-1} > 1$, it can be concluded that nonlinear effects must be included. The major problem with this criterion is that it cannot be clearly applied when $t_R t_T^{-1} \approx 1$, since the actual nonlinear resonance time will generally exceed t_R . In this case it is of interest to use our results to attempt to establish a more accurate method to determine the applicability of the linear theory.

The very similar behavior of the $\Delta\alpha_{eq}$ vs. ϕ_0 curves as displayed in Figs. 4.4 through 4.9 suggests that the nature of the interaction may be described by a single parameter which is a function of B_w , α_{eq_0} , n_{eq}

(or k) and $\frac{\partial \omega_H}{\partial z}$. The controlling factor in the interaction is the variation of phase, ϕ , as given by Eq. (2.36c). Note that for all sheets considered in Figs. 4.4 through 4.9 the set of values used for ϕ_0 is the same regardless of the values of the different parameters. For resonant particles $\dot{\phi}_0 \approx 0$, for nonresonant particles $\dot{\phi}_0$ is a non-zero constant. The different behavior of the sheets, whether they interact in the trapped or linear mode, is determined by the initial rate of change of $\dot{\phi}$, i.e. $\ddot{\phi}_0$. Neglecting the wave term in Eq. (2.36c) (the term proportional to $\frac{\cos \phi}{v}$) $\ddot{\phi}$ is given by Eq. (2.25). Rewriting that we have

$$\ddot{\phi} = \left[\frac{3}{2}v_{\parallel} + \frac{kv_{\perp}^2}{2\omega_H} \right] \frac{\partial \omega_H}{\partial z} - k \left(\frac{eB}{m} \right) v_{\perp} \sin \phi \quad (4.2)$$

The first and second terms on the r.h.s. in Eq. (4.2) represent the inhomogeneity and wave forces respectively. We now define a quantity ρ :

$$\rho = \frac{k \left(\frac{eB}{m} \right) v_{\perp}}{\left[\frac{3}{2}v_{\parallel} + k \frac{v_{\perp}^2}{2\omega_H} \right] \frac{\partial \omega_H}{\partial z}} \quad (4.3)$$

This quantity is the ratio of the maximum absolute values of the wave and inhomogeneity terms in Eq. (4.2). Hence the value of ρ is an indication of the relative effectiveness of these terms. Similar analyses to study the relative effects of the wave and inhomogeneity terms were used by previous authors [Dysthe, 1971; Nunn, 1974; Karpman, 1974; Roux and Pellat, 1976]. Here we carry this work a step forward:

We can rewrite ρ to obtain:

$$\rho = \frac{2k \left(\frac{eB_w}{m} \right) \tan \alpha}{\left[3 + \left(\frac{\omega_H - \omega}{\omega_H} \right) \tan^2 \alpha \right] \frac{\partial \omega_H}{\partial z}} \quad (4.4)$$

where we have used (2.30) to eliminate k in the denominator. Note that ρ is a dimensionless quantity dependent on B_w , α (local pitch angle), k and $\frac{\partial \omega_H}{\partial z}$.

We expect that ρ will be a useful quantity for differentiating between linear and nonlinear interactions. For instance linear theory predicts that for a particle that is resonant with the wave at some point z_1 along the magnetic field line the resonance will effectively terminate at a point z_2 defined by (4.1). If, for any particular case, we compute the quantity ρ at z_2 we can determine whether the resonance interaction will proceed significantly beyond z_2 . Thus if $\rho < 1$ at z_2 we can conclude that the wave forces are weaker than the inhomogeneity and that linear theory should apply. If $\rho > 1$ at z_2 we can conclude that the resonance interaction will proceed significantly beyond z_2 , that linear theory is not appropriate, and that a full nonlinear treatment should be employed.

In practice the evaluation of ρ is simplified by the fact that for the dipole model $\rho(z_1) \approx \rho(z_2)$, and thus ρ can generally be simply evaluated completely in terms of the initial conditions. A slight complication occurs when the initial resonance point approaches the magnetic equator, since then $\rho(z_1) \rightarrow \infty$ as $\frac{\partial \omega_H}{\partial z} \rightarrow 0$. In this case we must evaluate ρ at the point z_2 . An analytic expression for z_2 can be found

using (4.1) and (4.2) in the limit $B_w = 0$. From Eq. (4.2) we have

$$\ddot{\phi} = \left[\frac{3}{2v_{\parallel}} + \frac{kv_{\perp}^2}{2\omega_H} \right] \frac{\partial \omega_H}{\partial z} \quad (4.5)$$

or

$$\frac{d^2 \phi}{dz^2} = \frac{1}{2v_{\parallel}} \left[3 + \left(\frac{\omega_H - \omega}{\omega_H} \right) \tan^2 \alpha \right] \frac{\partial \omega_H}{\partial z} \quad (4.6)$$

where we have used (2.30) to eliminate k . In a dipole field, for locations close to the equator the variation of the gyrofrequency is very closely approximated by [Helliwell, 1970].

$$\omega_H = \omega_{H_0} \left[1 + \frac{9}{2} \left(\frac{z}{R} \right)^2 \right] \quad (4.7)$$

where ω_{H_0} is the angular electron gyrofrequency at the equatorial plane, R is the geocentric distance and z is the distance from the equator measured along the field line. Equation (4.6) can be twice integrated from $z = z_1 = 0$ to some point z by assuming that $v \approx v_R$ and $\omega_H \approx \omega_{H_0}$ and $\alpha \approx \alpha_0$ are constant. We obtain

$$\phi = \frac{\sigma}{v_R} \omega_{H_0} \frac{3}{2} \frac{z^3}{R^2} + \phi_0 \quad (4.8)$$

where $\sigma = \frac{1}{2} \left[3 + \frac{\omega_{H_0} - \omega}{\omega_{H_0}} \tan^2 \alpha_0 \right]$ and ϕ_0 is the initial phase. From (4.1) point z_2 is defined as that point at which $\Delta \phi \approx 1$ radian.

Therefore

$$z_2 = \left[\frac{2v_R R^2}{3\sigma \omega_{H_0}} \right]^{1/3} \quad (4.9)$$

Therefore for resonances at the equator ρ can be evaluated at point z_2 given by (4.9) using the value $\left. \frac{\partial \omega_H}{\partial z} \right|_{z_2} \approx 9\omega_{H_0} \left(\frac{z_2}{R^2} \right)$. For the parameters of Table 1,

$$z_2 \approx 576[3 + 0.63 \tan^2 \alpha_0]^{-1/3} \text{ km.} \quad (4.10)$$

and using these we obtain

$$\left. \frac{\partial \omega_H}{\partial z} \right|_{z_2} = 6.86 \times 10^{-1} [3 + 0.63 \tan^2 \alpha_0]^{-1/3} \text{ rad/km.} \quad (4.11)$$

The quantity $\rho(z_2)$ can be determined simply in terms of initial values by making use of the fact that $\omega_H(z_2) \approx \omega_{H_0}$ and $\alpha(z_2) \approx \alpha_0$. Thus two important features of the quantity ρ are: 1) its value can be used to determine when linear theory is appropriate, and 2) it can be evaluated simply in terms of the initial conditions alone.

In the following we demonstrate that the transitions from the linear to trapped mode in Figs. 4.4 through 4.9 occur at or near the $\rho \approx 1$ threshold.

In Table 2 we give the values of ρ for the cases covered in Figs. 4.4 through 4.9. First consider the wave amplitude dependence as illustrated in Fig. 4.4a for $\alpha_{eq_0} = 10^\circ$. Table 2a gives ρ for different B_w . From Figs. 4.4a we see that significant deviations of the $\Delta \alpha_{eq}$ vs ϕ_0 curves from a linear, near-sinusoidal, variation start at about $B_w = 7 \text{ mV}$. Since $\rho \approx 0.9$ for 7 mV we can loosely conclude that linear theory fails for $\rho > 1$.

Table 2b shows the corresponding values of ρ for the different wave amplitudes of Fig. 4.4b, for which $\alpha_{eq_0} = 30^\circ$. From that figure it is evident that a large deviation from the linear mode is seen for

TABLE II. VALUES OF ρ FOR DIFFERENT CASES

(a) $\alpha_{eq} = 10^\circ$, $L = 4$, $n_{eq} = 400$ el/cc.						
B_w (mY)	1	5	7	10	30	50
ρ	0.1	0.6	0.9	1.3	3.8	6.4
(b) $\alpha_{eq} = 30^\circ$, $L = 4$, $n_{eq} = 400$ el/cc.						
B_w (mY)	1	3	7	10	30	50
ρ	0.4	1.2	2.8	4.0	12.0	20.0
(c) $\alpha_{eq} = 10^\circ$, $B_w = 50$ mY, $L = 4$						
n_{eq} (el/cc)	400	200	50	10	5	1
ρ	6.4	4.5	2.3	1.0	0.7	0.3
(d) $B_w = 10$ mY, $L = 4$, $n_{eq} = 400$ el/cc						
α_{eq} (deg)	1	7	10	30	70	85
ρ	0.1	0.9	1.3	4.0	10.6	8.9

$B_w > 3$ mY compared to an almost linear result for $B_w = 1$ mY. Hence we can say that the deviation from linear theory starts at $B_w \approx 2-3$ mY. We see from Table 2b that $\rho \approx 1$ for these values. Therefore again $\rho = 1$ is a reasonably good indication of the point beyond which linear theory becomes inaccurate.

The value of ρ for the different n_{eq} values of Fig. 4.8 is given in Table 2c. We see from Fig. 4.8 that linear theory applies for

$n_{eq} \leq 10$ el/cc. Since $\rho = 1.0$ for $n_{eq} = 10$ el/cc we again see that linear theory threshold is at $\rho \approx 1$.

Figure 4.9 showed $\Delta\alpha_{eq}$ vs. ϕ_0 for different resonance points along the field line. It is evident from the figure that we have a well-defined linear mode for resonances at latitudes $\geq 10^\circ$. For particles resonant at 10° , $\rho(z_1) \approx \rho(z_2)$ and we can use $\partial\omega_H/\partial z$ at 10° latitude for computing ρ . This gives $\rho = 0.71$. Note that the $\Delta\alpha_{eq}$ vs. ϕ_0 curve for 10° latitude is very closely linear, whereas the one for 5° latitude is different from a linear mode. Here we have $\rho = 1.7$ for resonance at 5° and $\rho = 1.0$ at 7.5° latitude. Therefore we see that $\rho \approx 1$ is again a valid threshold point for determining linearity.

As a final test of our criterion we use the "experimental data" given in Fig. 4.7. Table 2d gives values of ρ for the α_{eq_0} values used in that figure. The deviation from the linear mode starts around $\alpha_{eq_0} = 7^\circ$ (which is not shown in Fig. 4.7) and $\rho \approx 0.9$ at that point, again very close to the $\rho \approx 1$ criteria which was established above. We would like to note here that the sharpness of the minima for $\alpha_{eq} = 5^\circ$ given in Fig. 4.7 is not so much due to the deviation from linearity as it is due to the wave term in Eq. (2.36c) since at that point

$$\Delta\alpha_{eq} \approx \alpha_{eq_0}.$$

As we examine Table 2d we see that ρ reaches a maximum at about $\alpha_{eq_0} = 50^\circ$. The pitch angle dependence of ρ is given from Eqs. (4.4) and (4.10) as:

$$\rho \propto \frac{\tan\alpha}{\left[3 + \left(\frac{\omega_H - \omega}{\omega_H}\right)\tan^2\alpha\right]^{2/3}} \quad (4.12)$$

The maximum of this function occurs when $(\frac{\omega_H - \omega}{\omega}) \tan^2 \alpha = 9$. For the parameters of Table 1, this maximum is at $\alpha \approx 75^\circ$. From Fig. 4.7 we see that for $\alpha_{eq_0} > 60^\circ$ the $\Delta\alpha_{eq}$ vs. ϕ_0 curves start to shrink while still staying in the trapped mode. This is readily explained by the fact that when the adiabatic accelerations \dot{v}_\parallel and \dot{v}_\perp are large the resonance time of the particle is decreased and this results in smaller scattering.

The correlation between Table 2d and Fig. 4.7, i.e., the fact that both ρ and the scattering curves reach a maximum for $\alpha \approx 65^\circ$ - 75° is very interesting. It indicates that not only is ρ useful as a threshold criteria for determining linearity, but also its absolute magnitude may be a direct indication of the amount of scattering. We have studied this question extensively and have determined that ρ can be successfully used as an empirical parameter for easy computation of the scattering coefficients for the trapped mode. This result is discussed in the next section, in connection with Fig. 4.19.

With the above results and comparisons we conclude the following:

- 1) The quantity ρ can be used to determine whether or not the linear theory is applicable for given interaction parameters.
- 2) For $\rho \ll 1$ ($\rho < 0.7$) linear theory results are close to those of the full nonlinear analysis.
- 3) For $\rho \gg 1$ ($\rho > 3$) we have a trapped mode and the linear theory is not applicable.
- 4) The linear theory results begin to deviate significantly from those of the full nonlinear analysis for $\rho > 1$.

Therefore we have a convenient and simple criteria for determining the applicability of the linear theory. The procedure is to compute ρ for the parameters of the problem at hand and decide according to the criteria cited above.

The criterion we have established above uses only the initial values of the parameters and variables. Therefore one need not computer the particle trajectories in order to use this criterion. This fact makes the method very useful in determining whether or not one can use a simple linear analysis for an interaction of a particle with a given pitch angle at any point along the field line with a wave of any frequency and wave amplitude.

Previous authors, e.g., Ashour-Abdalla [1972], have used linear theory without quantitative justification. For the parameters of Ashour-Abdalla [1972] and for equatorial interactions we compute $\rho = 0.6$ for $\alpha_{eq_0} = 10^\circ$, $\rho = 1.7$ for $\alpha_{eq_0} = 30^\circ$ and $\rho = 2.5$ for $\alpha_{eq_0} = 50^\circ$. Note that none of these values for ρ satisfy $\rho \ll 1$ which guarantees safe application of linear theory. Furthermore for $\alpha_{eq_0} > 30^\circ$, $\rho > 1$. For this reason we believe that the scattering coefficients given in that paper for resonances close to the equator (within 500-1000 km) are inaccurate for high pitch angles.

C. THE TRAPPED MODE

In this section we extend our study of the scattering of an initially resonant sheet starting at the equator and moving southward as depicted in Fig. 4.1. Here we consider the scattering for higher wave intensities and higher pitch angles emphasizing the cases for which $\rho > 1$ so that the interaction is in the trapped mode. The $\Delta\alpha_{eq}$ vs ϕ_0 curves for

this case have the shape shown in Fig. 4.10 for $\alpha_{eq_0} = 70^\circ$ and various values of B_w . As seen from this figure and Fig. 4.4 once the trapped mode is reached, further increase in B_w results in more scattering for all the trapped particles, while the general shape of the $\Delta\alpha_{eq}$ vs. ϕ_0 curve stays the same. Note that trapped particles are those for which ϕ makes more than one oscillation. For this case of poleward motion the trapped particles all suffer a decrease in pitch angle as described in section 2.A in connection with Figs. 4.3 and 4.4.

Owing to the characteristic shape of the $\Delta\alpha_{eq}$ vs. ϕ_0 curves it is conceivable that the behavior of the sheet could be studied by considering only one of the trapped particles, possibly the particle which is the most stably trapped, i.e. that for which $\phi_0 = 0$. To investigate this possibility we have plotted in Fig. 4.11 the total scattering $\Delta\alpha_{eq}$ for the $\phi_0 = 0$ particle versus the rms scattering $\sqrt{\langle \Delta\alpha^2 \rangle}$ where $\langle \rangle$ denotes averaging over all initial phases. We have shown results for initial pitch angles from 10° to 70° . For each pitch angle $\Delta\alpha_{eq}$ is varied by changing the wave intensity. We see from Fig. 4.11 that, within an error of less than 10%, the $\Delta\alpha_{eq}$ for $\phi_0 = 0^\circ$ particle and the rms scattering are linearly related with a proportionality constant of ~ 2 . This result means that for the trapped mode the scattering of the entire sheet of particles can be estimated by computing only the trajectory for the most stably trapped ($\phi_0 = 0$) particle. The slight deviation of some portion of the $\alpha_{eq_0} = 10^\circ$ curve from the others is due to the fact that the interaction is not entirely in the trapped mode for wave intensities corresponding to that portion (see Fig. 4.4a).

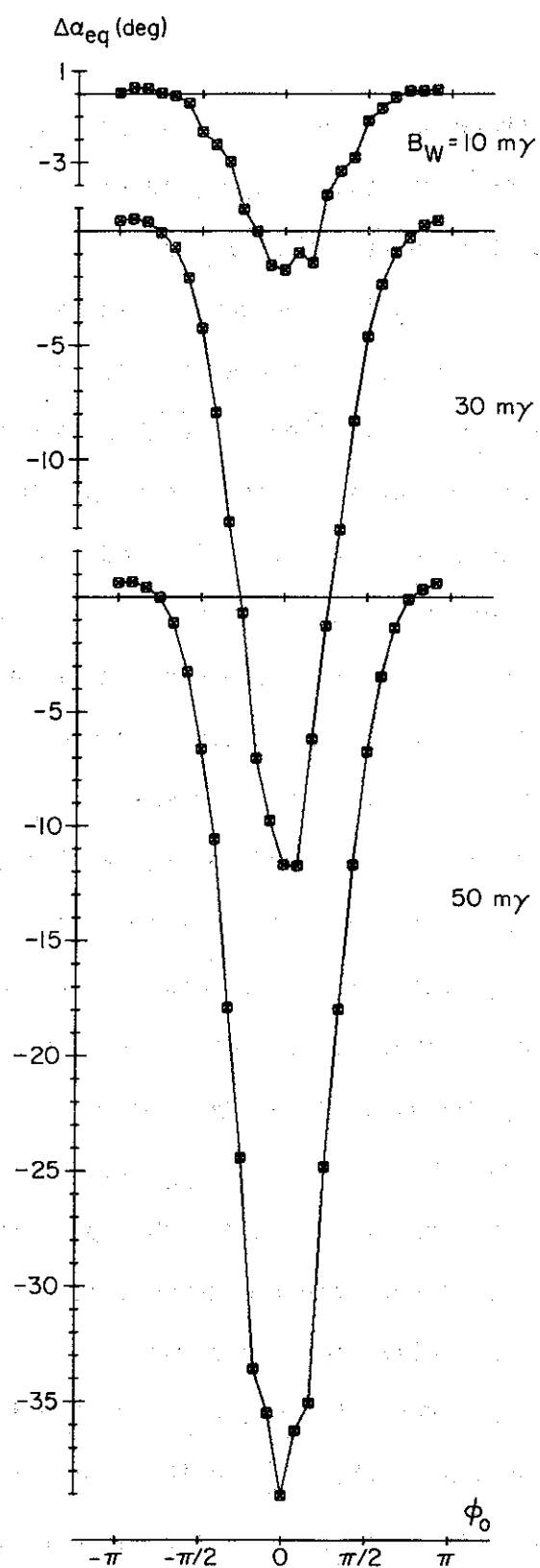


FIGURE 4.10 TOTAL SCATTERING AS A FUNCTION OF WAVE INTENSITY FOR $\alpha_{eq_0} = 70^\circ$. Other parameters have the values given in Table 1.

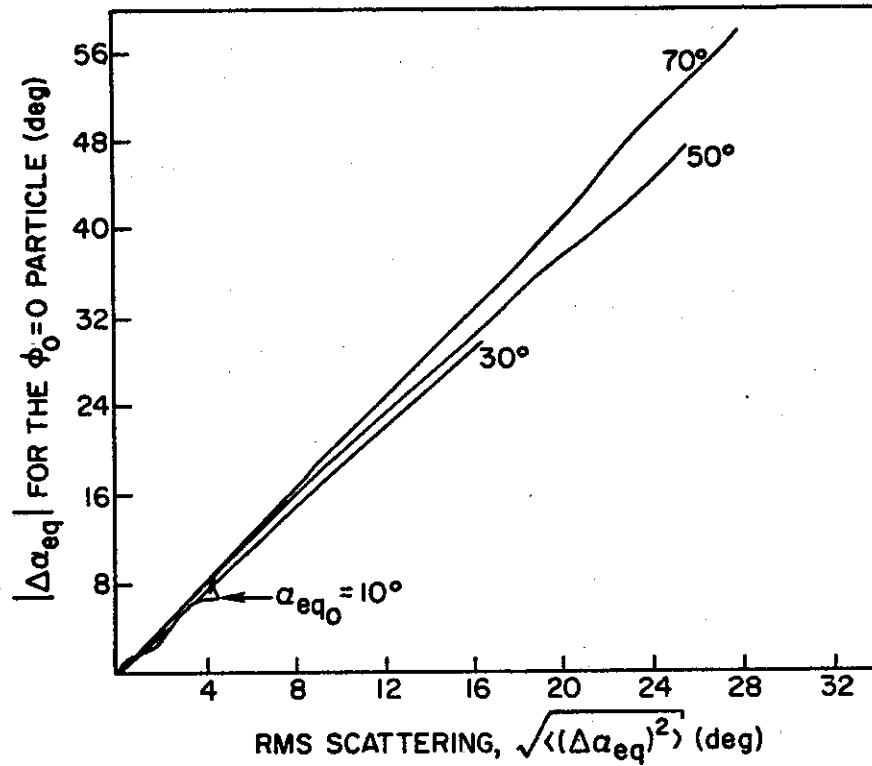


FIGURE 4.11 $|\Delta\alpha_{eq}|$ FOR THE MOST STABLY TRAPPED PARTICLE VERSUS RMS SCATTERING.

In the rest of this section, we give results for the scattering of the $\phi_0 = 0^\circ$ particle, denoting its total pitch angle change by $\Delta\alpha_{eq}$. In view of the result given in Fig. 4.11 the rms scattering should be $\sim 0.5 \Delta\alpha_{eq}$.

Figure 4.12 shows the phase ϕ and $\Delta\alpha_{eq}$ in a typical trajectory for the most stably trapped particle. For this case $B_w = 50 m\gamma$ and $\Delta\alpha_{eq_0} = 70^\circ$. The particle is strongly trapped in the potential well of the wave and the phase ϕ goes through many oscillations. As the par-

particle moves away from the equator the stable points around which oscillates slowly drifts upward (due to increasing ω_H) until it reaches $\pi/2$ at $t \approx 320$ msec at which time the particle becomes detrapped. During the time the particle is trapped, its pitch angle continuously decreases to a total net value of $\Delta\alpha_{eq} \approx 40^\circ$ at $t \approx 320$ msec.

The motion of the trapped particle can be understood by considering the 'pendulum' equation (2.45) rewritten as

$$\ddot{\phi} + k\left(\frac{eB}{m}\right)v_{\perp} \sin\phi = \left[\frac{3}{2}v_{\parallel}^2 + \frac{kv_{\perp}^2}{2\omega_H} \right] \frac{\partial\omega_H}{\partial z} \quad (4.13)$$

The forcing function of this equation is

$$G(z) = H(t) = \left[\frac{3}{2}v_{\parallel}^2 + \frac{kv_{\perp}^2}{2\omega_H} \right] \frac{\partial\omega_H}{\partial z} \quad (4.14)$$

For particles moving away from the equator $\frac{\partial\omega_H}{\partial z}$ continually increases so that $H(t)$ is an increasing function of time. In a dipole field, for locations close to the equator the variation of ω_H is approximated by (4.7). Using that we obtain

$$H(t) \approx \left[\frac{3}{2}v_{\parallel}^2 + \frac{kv_{\perp}^2}{2\omega_H} \right] \left(\frac{9\omega_{H_0} v_{\parallel}}{R^2} \right) t \quad (4.15)$$

The restoring force of the 'pendulum' is proportional to $k\left(\frac{eB}{m}\right)v_{\perp}$. If the forcing function $H(t) \approx 0$ (i.e. for a homogeneous field) the phase ϕ oscillates around $\phi = 0$ with a period of $t_T = 2\pi/(\bar{\omega})$ where $\bar{\omega}^2 = k\left(\frac{eB}{m}\right)v_{\perp}$. Since $\frac{dv}{dt}$ and $\frac{d\alpha}{dt}$ are both proportional to $\sin\phi$ (see Eq. (2.46a,b) the electron energy and pitch angle would also oscillate around $\phi = 0$ with the same period t_T .

In the inhomogeneous case, however, $\phi = 0$ is no longer an equilibrium value for ϕ . The equilibrium value $\bar{\phi}$, for which $\ddot{\phi} = 0$, is given by

$$\bar{\phi} = \frac{1}{\omega} \left[\frac{3}{2} v_{\parallel} + \frac{k v_{\perp}^2}{2 \omega_H} \right] \frac{\partial \omega_H}{\partial z} = \frac{H(t)}{\omega} \quad (4.16)$$

If the right hand side of (4.16) varies slowly compared to t_T , the phase ϕ oscillates around this new equilibrium value with a period $t_T' = 2\pi/(\omega \sqrt{\cos \bar{\phi}})$.

For particles moving away from the equator $\bar{\phi}$ slowly increases with time. Initially $\bar{\phi} \approx 0$ and therefore $t_T' = t_T$. Note that the particle is detrapped when $\phi = \pi/2$ which must occur before $\bar{\phi} = \pi/2$ because of the excursions of ϕ around $\bar{\phi}$. Since ϕ stays close to $\bar{\phi}$ for the trapped particles and $0 \leq \bar{\phi} < \pi/2$ all trapped particles decrease in energy (see Eq. (2.46a,b)) for this case. For particles moving toward the equator $\frac{\partial \omega_H}{\partial z} < 0$ and $-\pi/2 < \bar{\phi} \leq 0$, so that the trapped particles increase in energy and pitch angle.

Note that since v_{\perp} decreases (see Eq. (2.36b)) during the interaction the restoring force weakens. The oscillating frequency ω decreases in time, so that the period, t_T' varies not only because of varying $\bar{\phi}$ but also because of variation of ω .

Note that the problem of a strongly trapped particle is completely analogous to the case of a heavy pendulum with an applied torque $\tau(t)$ such that $\tau(t)$ is an increasing function. In that case the restoring force is gravity instead of the wave forces and the forcing function is $\tau(t)$ instead of $H(t)$. The analogy is depicted in Fig. 4.12 where we show the pendulum position at various places along the particle trajectory.

Accurate analytic treatment of the particle motion taking into account all of these effects is only possible when $\dot{H}(t)t_T' \ll H(t)$. For that case one can use an adiabatic approximation by averaging over one oscillation. The computer simulation of the basic equations of motion (2.36) accounts for all of the effects in the general case, even for cases when ϕ does not go through one oscillation. An example of this is the particle trajectories given in Fig. 4.2. Those particles are not trapped, but their motion is still described by (4.13) and the analogy with the pendulum is still valid. Note from Fig. 4.12 that all aspects discussed above, including the variation of t_T' due to changing v_\perp , are clearly visible from the computed trajectory.

With these insights into the physics of the trapped particle motion we now survey the pitch angle and energy scattering for different parameters using the $\phi_0 = 0$ particle as our standard for the complete sheet.

Figure 4.13 shows $\Delta\alpha_{eq}$ versus α_{eq_0} for different wave intensities. For any given wave intensity $\Delta\alpha_{eq}$ peaks around $\alpha_{eq_0} \approx 65^\circ$. The scattering for the $\alpha_{eq_0} = 80^\circ$ particle is less than that for $\alpha_{eq_0} = 70^\circ$ although at first thought one might have expected a larger $\Delta\alpha_{eq}$. This behavior can be understood with the aid of Eqs. (4.13) - (4.16), in connection with Eq. (2.46b). From Eq. (2.46b) we see the wave induced pitch angle changes are proportional to $\sin\phi$. Assuming many oscillations in the interaction region $\phi \approx \bar{\phi}$, where $\bar{\phi}$ is given by (4.16). Examining the two terms of $H(t)$ we find that for the parameters of Table 1,

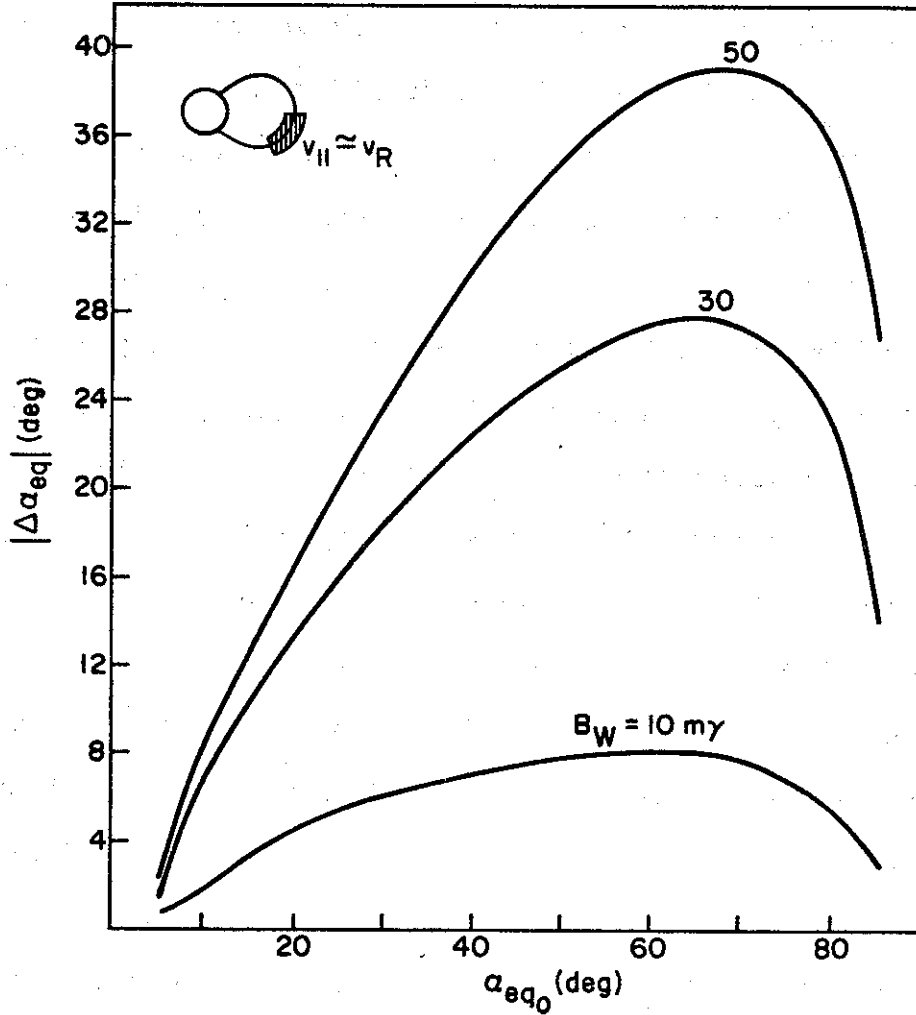


FIGURE 4.13 $|\Delta\alpha_{eq}|$ FOR THE $\phi_0 = 0$ PARTICLE VERSUS α_{eq0} FOR THREE DIFFERENT WAVE INTENSITIES. The figure in the upper left corner indicates that the interaction starts at resonance at equator and that the particle is trapped throughout the interaction region with $v_{||} \approx v_R$. Pitch angles from the loss cone ($\sim 5^\circ$) to 85° are considered. For $\alpha_{eq0} > 85^\circ$ the particle energies are in the relativistic range.

$$\frac{3}{2} v_{||} > \frac{kv_{\perp}^2}{2\omega_H} \quad \text{for } \alpha < 65^\circ$$

and

$$\frac{3}{2} v_{||} < \frac{kv_{\perp}^2}{2\omega_H} \quad \text{for } \alpha > 65^\circ$$

(4.17)

Therefore for $\alpha < 65^\circ$ we have

$$H(t) \approx \frac{3}{2} v_{\parallel} \frac{\partial \omega_H}{\partial z} \quad (4.18)$$

and

$$\frac{1}{\phi} \approx \frac{\frac{3}{2} v_{\parallel} \frac{\partial \omega_H}{\partial z}}{\omega^2} = \frac{\frac{3}{2} v_{\parallel} \frac{\partial \omega_H}{\partial z}}{\frac{eB}{k(\frac{w}{m})}} \left(\frac{1}{v_1} \right) \quad (4.19)$$

so that for $\alpha < 65^\circ$ $H(t)$ is approximately independent of pitch angle and ϕ decreases with increasing pitch angle. Therefore the distance from the equator to the point where $\phi \approx \pi/2$ (detrapping point) is increased, therefore increasing the interaction length, L_I . The interaction length L_I is defined as the distance from the equator to the point where $\phi \approx \pi$. The wave induced pitch angle scattering is given from (2.46b) as

$$d\alpha \approx \left[-\left(\frac{eB}{m}\right) \sin\phi - \left(\frac{e}{m} E_w\right) \frac{\cos\alpha}{v} \sin\phi \right] dt \quad (4.20)$$

and the total pitch angle change can be obtained by integrating (4.20),

$$\Delta\alpha \approx - \int_0^{T_I} \left[\left(\frac{eB}{m}\right) \sin\phi + \left(\frac{e}{m} E_w\right) \frac{\cos\alpha}{v} \sin\phi \right] dt \quad (4.21)$$

where T_I is the interaction time given approximately by $T_I = \int_0^{L_I} \frac{dz}{v_{\parallel}}$.

From (4.21) it is obvious that increased interaction length (or time)

should result in larger pitch angle changes. Therefore for $\alpha < 65^\circ$

$\Delta\alpha_{eq}$ increases with pitch angle. For $\alpha > 65^\circ$ we have

$$H(t) \approx \frac{kv_1}{2\omega_H} \frac{\partial \omega_H}{\partial z} \quad (4.22)$$

and

$$\bar{\phi} = \frac{\frac{kv_{\perp}^2}{2\omega_H} \frac{\partial \omega_H}{\partial z}}{\omega^2} = \frac{\frac{\partial \omega_H}{\partial z}}{2\omega_H \left(\frac{eB}{m}\right)} \cdot (v_{\perp}) \quad (4.23)$$

It is evident from (4.23) that for $\alpha > 65^\circ$ $\bar{\phi}$ at any point during the interaction is higher for higher pitch angles. Therefore $\bar{\phi}$ reaches $\pi/2$ quicker and the interaction length is shortened, resulting in smaller $\Delta\alpha_{eq}$.

Note that the above discussion is qualitative. The pitch angle and v_{\perp} change during the interaction so that the variation of $\bar{\phi}$ could go from that given by (4.23) to that given by (4.19), if the local pitch angle decreases below 65° . Also in (4.20) we have ignored the adiabatic variation in (2.46b). This is an additional complicating factor especially for high pitch angles. Furthermore the approximation (4.7) begins to break down when the interaction length becomes large. In that case $H(t)$ does not vary linearly in time. Therefore decreased (increased) $\bar{\phi}$ does not necessarily mean smaller (larger) scattering. One other factor that further complicates the problem can be seen from Eq. (2.46b). The pitch angle change due to \bar{E}_w is proportional to $\frac{\cos\alpha}{v}$. Since v_{\parallel} is fixed by (2.30), resonant particles at higher pitch angles have larger v . Since $\cos\alpha$ is smaller for higher pitch angles, this effect also contributes to the decreased $\Delta\alpha_{eq}$ at higher pitch angles. The results given in Fig. 4.13 and the following figures are taken directly from the computer simulation which accounts for all factors. The approximate analytical discussion given above is very useful, however, especially for the qualitative understanding of the results.

Figure 4.14 illustrates the B_w dependence of $\Delta\alpha_{eq}$ that is partially implicit in Fig. 4.13. For each α_{eq_0} the pitch angle change increases with wave intensity, until $\Delta\alpha_{eq} \approx \alpha_{eq_0}$. Shown in a dashed line is the extension of the variation for small wave intensities. For these low wave amplitudes the scattering is in the linear mode. Although the amplitude below which this occurs is dependent on α_{eq_0} , the differences are not noticeable on the scale of Fig. 4.14. Note from this figure that for $B_w \lesssim 5 m\gamma$, $\Delta\alpha_{eq}$ is again approximately proportional to B_w , although with much steeper slope than that for the linear mode. Also $\Delta\alpha_{eq}$ saturates when $\Delta\alpha_{eq} \approx \alpha_{eq_0}$. The distortion in the $\alpha_{eq_0} = 10^\circ$ one around $B_w \approx 10 m\gamma$ is due to the fact that this wave intensity is not sufficient to achieve a trapped mode (see Fig. 4.4a). The slow decrease of $\Delta\alpha_{eq}$ for $B_w > 40 m\gamma$ for the $\alpha_{eq_0} = 10^\circ$ particle is a real effect. This effect is due to the "loss cone reflection effect" explained in Appendix B. The sharp minimum of the $\phi_0 = 0$ curves of Fig. 4.3 were also attributed to this effect (see Section 2.A).

Figure 4.15 shows the interaction length L_I as a function of wave intensity for different α_{eq_0} . For $\alpha_{eq_0} \leq 70^\circ$ the interaction length increases with wave intensity in the same manner as $\Delta\alpha_{eq}$ shown in Fig. 4.14. For $B_w > 30 m\gamma$, L_I for $\alpha_{eq_0} = 80^\circ$ is less than that for $\alpha_{eq_0} = 70^\circ$, as expected from the discussion connected with (4.23). However for $B_w > 30 m\gamma$ the interaction length for $\alpha_{eq_0} = 80^\circ$ is larger than that for $\alpha_{eq_0} = 70^\circ$ although $\Delta\alpha_{eq}$ is smaller as seen from Fig. 4.13. This could result from the fact that for $B_w > 30 m\gamma$ the pitch angle changes (or changes in v_\perp) during the interaction could cause $\bar{\phi}$ to transform from a variation given by (4.23) to that given by (4.19).

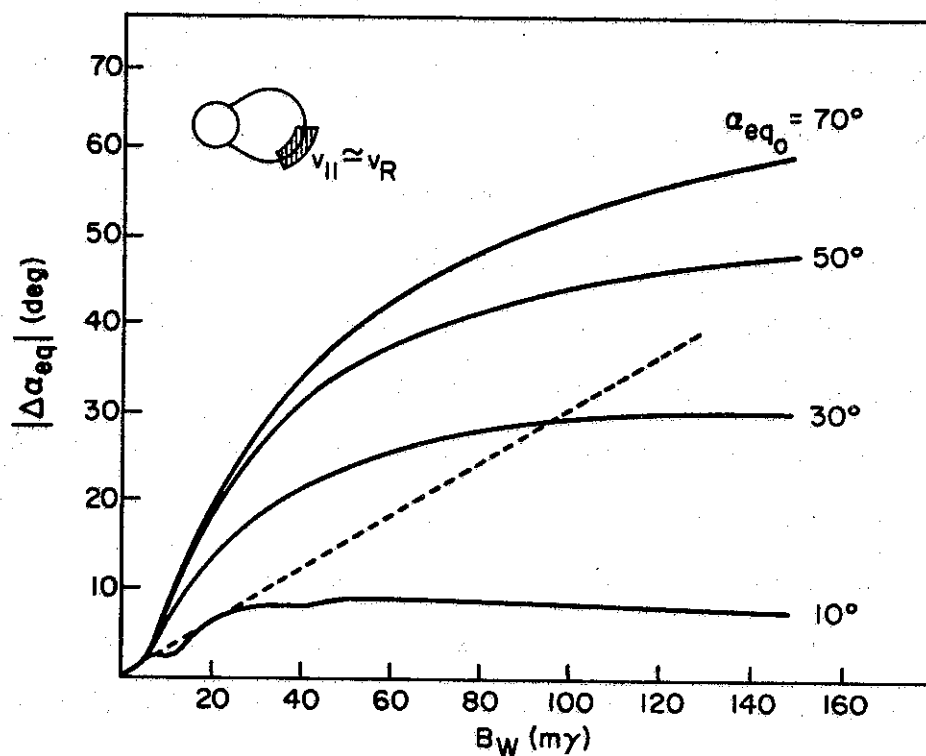


FIGURE 4.14. $|\Delta\alpha_{eq}|$ FOR THE $\phi_0 = 0$ PARTICLE VERSUS B_w FOR DIFFERENT α_{eq0} . The dashed line is an extension of the linear mode variation for small wave intensities.

Further evidence for this is the L_I variation for $\alpha_{eq0} = 85^\circ$. The crossover occurs at $B_w \approx 50 \text{ m}\gamma$ for this case as would be expected since for any given B_w , $\Delta\alpha_{eq}$ for $\alpha_{eq} = 85^\circ$ is less than that for $\alpha_{eq} = 80^\circ$ (see Fig. 4.13). Note that the interaction length for $B_w = 0$ is $\sim 600 \text{ km}$ for $\alpha_{eq0} = 10^\circ$ and 250 km for $\alpha_{eq0} = 85^\circ$ in accordance with a pitch angle dependence proportional to $[3 + 0.63 \tan^2 \alpha]^{-1/3}$ as can be seen from (4.10). Note that $L_I \neq z_2$, however L_I can be approximately calculated from Eq. (4.8) by setting $\Delta\phi \approx \pi$. The slight increases in L_I for $\alpha_{eq0} = 10^\circ$ at $B_w \approx 50 \text{ m}\gamma$ and $\alpha_{eq0} = 30^\circ$ at $B_w \approx 100 \text{ m}\gamma$ are due again to the "loss cone reflection effect" that is discussed in

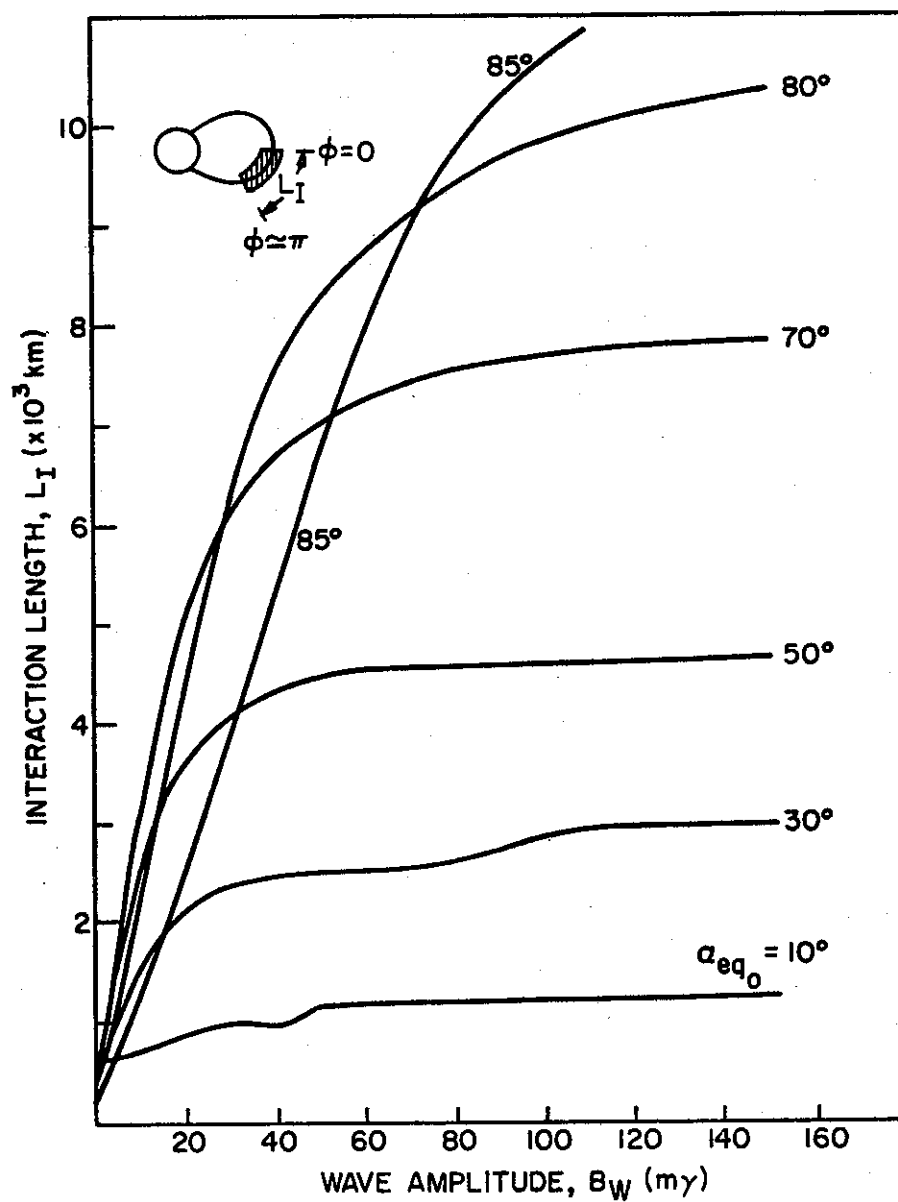


FIGURE 4.15 INTERACTION LENGTH, L_I , VERSUS B_W PLOTTED FOR DIFFERENT α_{eq_0} .

Appendix B.

The most important aspect of the result shown in Fig. 4.15 is the fact that for all α_{eq_0} , L_I stays constant beyond same wave intensity. This means that for wave intensities beyond that for which $\Delta\alpha_{eq} \approx \alpha_{eq_0}$ it is not possible to reach $\phi \approx \pi$ point any quicker. It is also not possible to have $\Delta\alpha_{eq}$ equal to α_{eq_0} in a shorter distance. This is at first surprising since it seems from (2.46b) that higher B_w should give larger $d\alpha$. However, with increased wave amplitude $\bar{\omega}$ is reduced, therefore reducing $\bar{\phi}$ through (4.16). Since $d\alpha$ in (2.46b) is proportional to $B_w \sin\phi$ the differential changes, initially, are about the same, resulting with the same interaction length and total scattering.

Figure 4.16 shows the percentage energy change (ΔK_E) versus α_{eq_0} for different wave intensities. The quantity ΔK_E is defined as

$$\Delta K_E = \left| \frac{K_E^O - K_E^F}{K_E^O} \right| \times 100$$

where K_E^O and K_E^F are the initial (before interaction) and final (after interaction) kinetic energies of the particle. We see that ΔK_E varies much the same way as $\Delta\alpha_{eq}$ shown in Fig. 4.13. The peak around $\alpha \approx 65^\circ$ could be qualitatively explained by using arguments similar to those used for that figure.

Note that although the percentage energy change decreases at higher pitch angles, the absolute value of energy change should continue to increase since energy exchange occurs only through v_\perp which is higher at higher pitch angles. This is illustrated in Fig. 4.17 where we plot

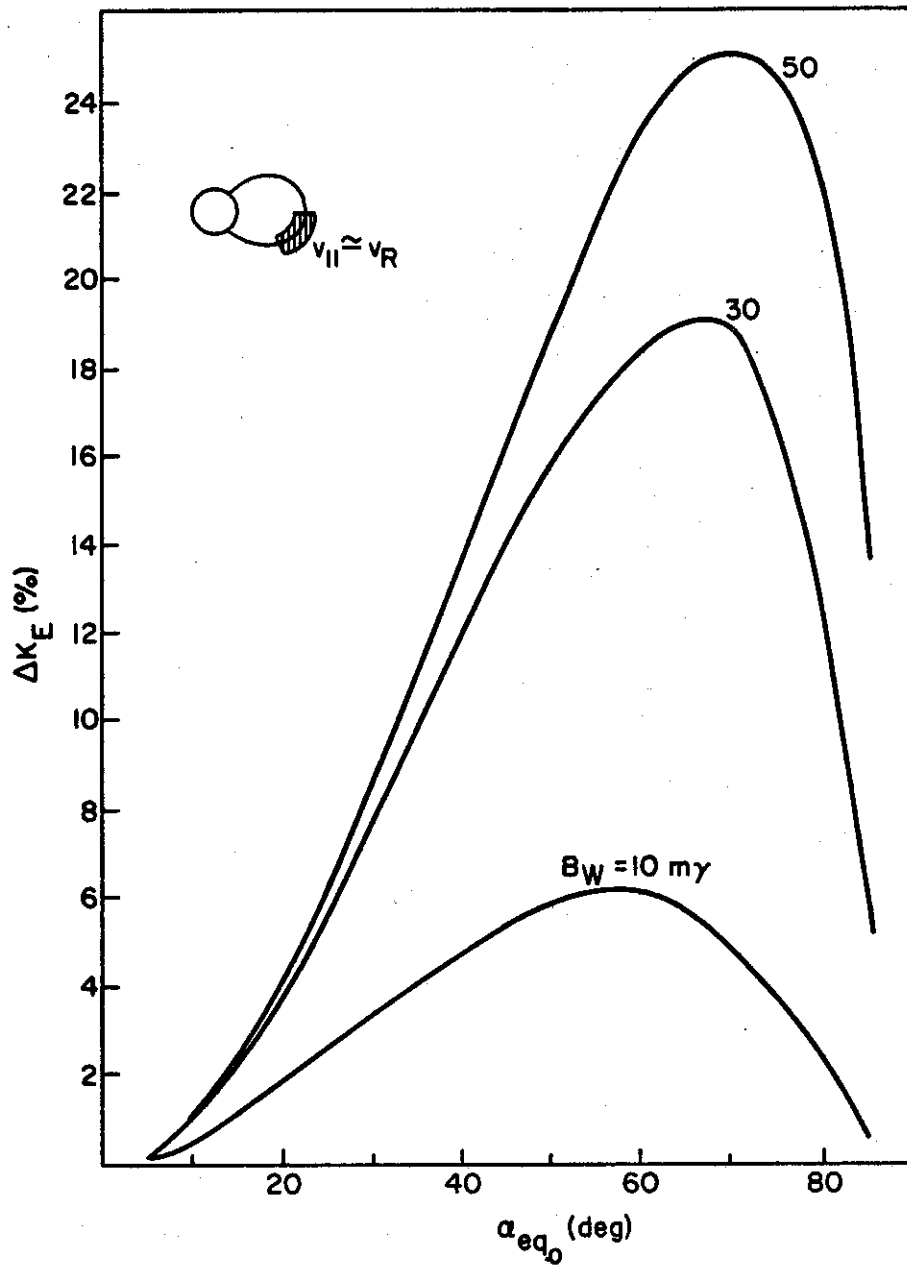


FIGURE 4.16 PERCENTAGE ENERGY CHANGE, ΔK_E , FOR THE $\phi_0 = 0$ PARTICLE VERSUS α_{eq_0} PLOTTED FOR DIFFERENT B_w .

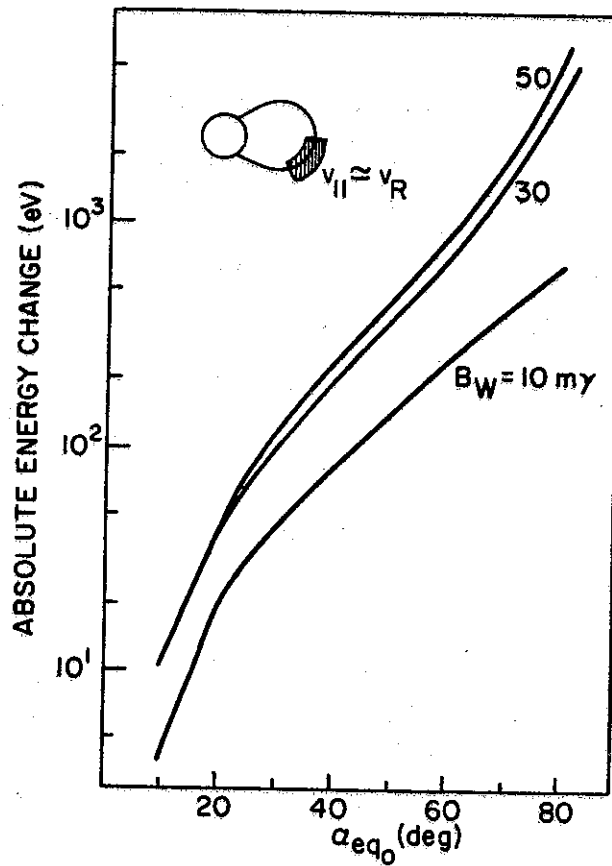


FIGURE 4.17 TOTAL ABSOLUTE ENERGY CHANGE IN ELECTRON VOLTS VERSUS α_{eq_0} PLOTTED FOR DIFFERENT B_w .

the total absolute energy change for the particle in electron volts (eV) versus α_{eq_0} for different values of B_w . We observe that total absolute energy change increases with both B_w and α_{eq_0} .

Finally in Fig. 4.18 we show the wave amplitude dependence of ΔK_E which is implicit in Fig. 4.16. We see that this variation is very similar to that of $\Delta \alpha_{eq}$ in Fig. 4.14.

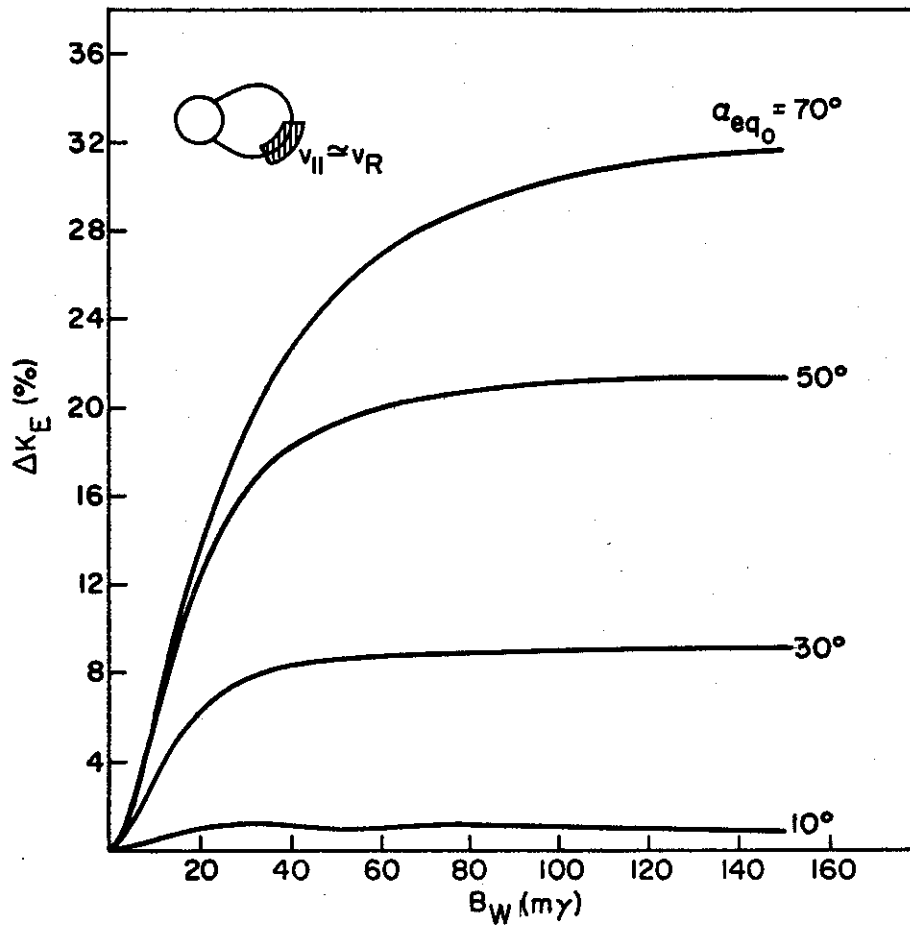


FIGURE 4.18 PERCENTAGE ENERGY CHANGE ΔK_E VERSUS B_W PLOTTED FOR DIFFERENT α_{eq_0} .

Note from Fig. 4.14, that, for instance, for $\alpha_{eq_0} = 30^\circ$ and $B_W = 100 \text{ mγ}$, $\Delta\alpha_{eq} \approx \alpha_{eq_0}$, meaning that the particle has lost all of its perpendicular energy. The initial perpendicular energy of this particle was 25% of its total energy since $v_\perp^2 = (v \sin 30^\circ)^2 = 0.25v^2$. However Fig. 4.18 shows that the particle has lost only 8% of its total initial energy. That the particle's total initial perpendicular energy is not extracted can be understood as follows: During the process of the strongly trapped interaction $v_\parallel \approx v_R$ where v_R is the local resonance

velocity. Since v_R increases as the particle moves away from the equator, particles parallel energy must increase during the interaction, resulting in the extraction of less than the initially available perpendicular energy of the particle. One can loosely define an energy extraction efficiency as the ratio of the extracted and initially available perpendicular energies. For $\alpha_{eq} \approx 30^\circ$ that efficiency is $\sim 32\%$. For $\alpha_{eq} \approx 70^\circ$ available energy is 88%, while only $\sim 32\%$ is extracted for $B_w \approx 150 m_Y$ for which $\Delta\alpha_{eq} \approx 60^\circ$. So the energy extraction efficiency for that case is $\sim 36\%$. For $\alpha_{eq_0} = 10^\circ$ the extraction efficiency is $\sim 33\%$. Therefore we can conclude that for the values used in our computations and approximately independent of pitch angle the cyclotron resonance interaction is $\sim 30\%$ efficient in extracting the particle's perpendicular energy. This is true regardless of the wave intensity as long as B_w is large enough so that $\Delta\alpha_{eq} \approx \alpha_{eq_0}$. Note that in terms of pitch angle the interaction is 100% efficient, since for any α_{eq_0} a B_w could be found for which $\Delta\alpha_{eq} \approx \alpha_{eq_0}$. Again wave intensities beyond that one cannot do any better.

ρ as an empirical criteria

We have indicated in section 3.B that the correlation between the pitch angle dependence of ρ and the variation of $\Delta\alpha_{eq}$ vs. ϕ_0 curves given in Fig. 4.7 was interesting and could mean that ρ can be used as an indication of absolute scattering for a given case as well as a criterion for linear theory.

Figure 4.19 shows rms scattering $\sqrt{\langle \Delta\alpha_{eq}^2 \rangle}$ versus ρ for $\alpha_{eq_0} = 30^\circ, 50^\circ$ and 70° . In this case ρ is varied by varying B_w . The dashed line is drawn to indicate the average trend. Note that the var-

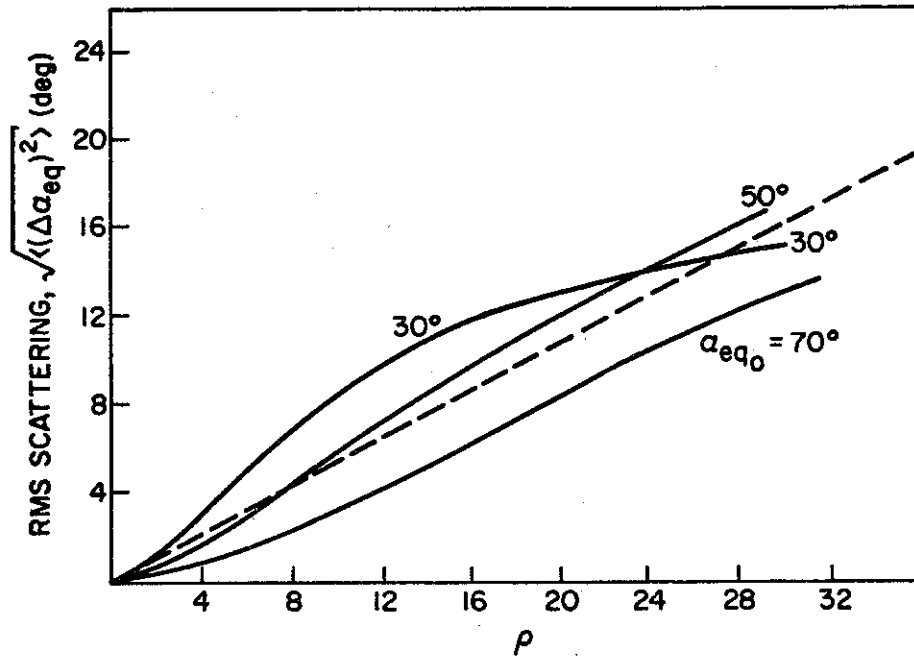


FIGURE 4.19 rms SCATTERING $\sqrt{\langle (\Delta \alpha_{eq})^2 \rangle}$ VERSUS ρ . The dashed line shows the average trend.

iations for different α_{eq_0} do not deviate more than 20% from the dashed line. Hence in any given problem where B_w , k , $\frac{\partial \omega_H}{\partial z}$ and is specified, one can compute ρ using (4.4) and find the rms scattering from Fig. 4.19 within an error of 20%. It could be possible to increase the accuracy further by multiplying by some appropriate functions of pitch angle. This seems possible since comparing Figs. 4.14 and 4.19 we see that the pitch angle dependence of ρ brings the curves for different α_{eq_0} together in the right direction but rather too much probably because it is computed in terms of initial parameters and the pitch angle significantly changes during the interaction.

V. PRECIPITATED FLUX FROM A FULL DISTRIBUTION OF PARTICLES

In this chapter we present an application of our simulation for the calculation of the one-pass precipitated electron flux for a particular case.

A. SIMULATION OF THE FULL DISTRIBUTION

The full distribution of particles is simulated by a large number of test particles. For energetic particles adiabatically trapped in the earth's magnetic field, the particles population in every flux tube can be represented by an equatorial distribution function $f_{eq}(v_{||eq}, \alpha_{eq})$.

From this point on we drop the subscript 'eq' for the purpose of simplifying the text. Unless otherwise mentioned all quantities $v_{||}$ and α in this chapter represent equatorial values. We have chosen to work with the distribution function in the $v_{||}$ - α space as opposed to v - α or $v_{||}$ - v_{\perp} spaces. This formulation is convenient for our simulation since it directly shows the pitch angle scattering along the axis and makes it possible to uniquely identify each $v_{||}$ mesh point with a resonance location through (2.30). The velocity space volume element in terms of $v_{||}$ and α is $v_{||}^2 \frac{\sin \alpha}{\cos^3 \alpha} d\alpha dv_{||} d\phi$ (see Appendix C).

For a given field line and a given wave, only a limited portion of the total particle population represented by this distribution will resonate with and hence be scattered significantly by the wave. Therefore, in our simulation, we need only consider that limited portion of the distribution function. This is the shaded area shown in Fig. 5.1a. The α_{min} is determined by the loss cone. For given plasma and wave parameters α_{max} is determined by the nature of the problem. For

EQUATORIAL DISTRIBUTION FUNCTION

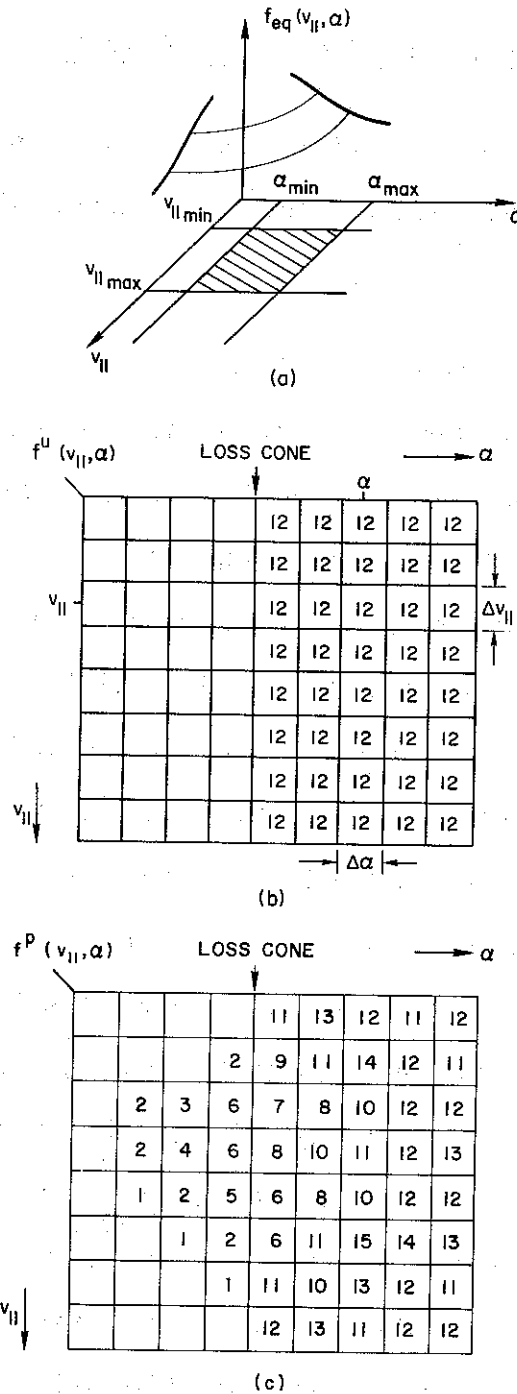


FIGURE 5.1 SIMULATION OF THE DISTRIBUTION FUNCTION. (a) The general distribution. The shaded area is the portion that will be significantly affected by the wave. (b) Unperturbed distribution. In this illustration a uniform distribution with $f(v_{||}, \alpha) = 12$ above the loss cone and $f(v_{||}, \alpha) = 0$ in the loss cone is shown. (c) Perturbed distribution.

example, for the computation of the one-pass precipitated flux, an $\alpha_{\max} < \pi/2$ can always be found such that for the given parameters, particles with $\alpha > \alpha_{\max}$ cannot be scattered into the loss cone at the first encounter with the wave. On the other hand, if one wishes to consider the steady state scattering problem, it is necessary to take $\alpha_{\max} \approx 90^\circ$ since in this case multiple scatterings can bring high pitch angle particles down to the loss cone. The $v_{\parallel \min}$ is determined by the resonance velocity at the equator. Particles with parallel velocities lower than $v_{\parallel \min}$ do not resonate with the wave at any point along the field line. The upper limit $v_{\parallel \max}$ is determined by the fact that particles with higher v_{\parallel} resonate at points so far down the field line that the scattering produced is less than one half of the pitch angle mesh size used in the calculations. That is for given parameters we can find a $v_{\parallel \max}$ such that the scattering for particles with $v_{\parallel} > v_{\parallel \max}$ will be negligible and need not be considered. Once the shaded area is determined, this region in the $v_{\parallel} - \alpha$ space is divided into a number of mesh points. Each mesh point is identified with a pair v_{\parallel} and α . The value of the distribution at each mesh point is $f(v_{\parallel}, \alpha)$. Figure 5.1b illustrates such a representation of the distribution function. For purposes of illustration we have chosen a uniform distribution with a sharp cutoff at the loss cone. The mesh sizes in v_{\parallel} and α are Δv_{\parallel} and $\Delta \alpha$ respectively. The number density of particles with parallel velocities $v_{\parallel} \pm \frac{\Delta v_{\parallel}}{2}$ and pitch angles $\alpha \pm \frac{\Delta \alpha}{2}$ is given by

$$\Delta N = 2\pi f(v_{\parallel}, \alpha) v_{\parallel}^2 \frac{\sin \alpha}{\cos^3 \alpha} \Delta \alpha \Delta v_{\parallel} \quad (5.1)$$

where the factor 2π is due to integration over the cyclotron phase ϕ . We assume a uniform distribution in ϕ .

In our formulation each such population $(v_{\parallel} \pm \frac{\Delta v_{\parallel}}{2}, \alpha \pm \frac{\Delta \alpha}{2})$ of particles is represented by test particles with parallel velocity v_{\parallel} and pitch angle α . When the mesh sizes Δv_{\parallel} and $\Delta \alpha$ are chosen adequately small, the motion of these test particles accurately represent the motion of all particles with $v_{\parallel} \pm \frac{\Delta v_{\parallel}}{2}$ and $\alpha \pm \frac{\Delta \alpha}{2}$.

Since the gyroresonant interaction is highly dependent on initial phase we use 12 test particles uniformly distributed in ϕ for each mesh point. In that case each test particle with initial equatorial values $v_{\parallel 0}, \alpha_0$ and a certain phase ϕ_0 represents the population of particles with

$$\begin{aligned} v_{\parallel} &= v_{\parallel 0} \pm \frac{\Delta v_{\parallel}}{2} \\ \alpha &= \alpha_0 \pm \frac{\Delta \alpha}{2} \\ \phi &= \phi_0 \pm \frac{\pi}{12} \end{aligned} \quad (5.2)$$

The actual number density of particles described by (5.2) is

$$\frac{\Delta N}{12} = f(v_{\parallel 0}, \alpha_0) v_{\parallel 0}^2 \frac{\sin \alpha_0}{\cos^3 \alpha_0} \Delta \alpha \Delta v_{\parallel} \left(\frac{\pi}{6} \right) \quad (5.3)$$

The next step is to simulate the interaction for the test particle. The test particle is allowed to go through the complete interaction as described in Chapter 3. In other words the equations of motion for the test particle are integrated from the point N' in the northern hemisphere where $\epsilon = \frac{v_{\parallel} - v_R}{v_R} = -0.03$ till the point S' in the southern hemisphere where $\epsilon = +0.05$ (see Fig. 3.2b). At the end of the inter-

action the test particle has acquired a new equatorial velocity and pitch angle, namely $v_{\parallel F}$ and α_F (F for final) and must now be identified with the mesh point $(v_{\parallel F}, \alpha_F)$. This in effect means that the number of particles described by (5.3) have all acquired parallel velocity and pitch angle values in the ranges $v_{\parallel F} \pm \frac{\Delta v_{\parallel}}{2}$ and $\alpha_F \pm \frac{\Delta \alpha}{2}$ respectively. In order to conserve the total number density of particles in the system the following changes must be made in the values of the distribution function at $(v_{\parallel 0}, \alpha_0)$ and $(v_{\parallel F}, \alpha_F)$.

$$f_{\text{new}}(v_{\parallel 0}, \alpha_0) = f_{\text{old}}(v_{\parallel 0}, \alpha_0) - \frac{1}{12} f_{\text{old}}(v_{\parallel 0}, \alpha_0)$$

$$f_{\text{new}}(v_{\parallel F}, \alpha_F) = f_{\text{old}}(v_{\parallel F}, \alpha_F) + \frac{1}{12} f_{\text{old}}(v_{\parallel 0}, \alpha_0) \frac{v_{\parallel F}^2 \frac{\sin \alpha_F}{\cos^3 \alpha_F}}{v_{\parallel 0}^2 \frac{\sin \alpha_0}{\cos^3 \alpha_0}}$$

Using 12 such test particles for each mesh point, and repeating the procedure for every mesh point, we obtain the perturbed distribution.

Figure 5.1c shows an illustrative sketch of the perturbed distribution. After one pass of the wave the empty loss cone of the initial distribution is partly filled. The total number of precipitated particles and the precipitated flux can be obtained by properly integrating the perturbed distribution over v_{\parallel} and α . This is done in detail for the sample computation of the next section.

B. COMPUTATION OF FLUX FOR A PARTICULAR CASE

As an application of the technique described above, we compute the precipitated particle flux for a particular case. The medium and wave parameters given in Table 1 are used for different wave intensities. For these computations a pitch angle mesh size of 0.5 degrees is used, with 60 mesh points in pitch angle covering from $\alpha = 0^\circ$ to 30° in 0.5° steps. Pitch angles greater than 30° were not considered because even for the largest wave intensity used in the calculations ($B = 50 m_T$) no particles with $\alpha_0 > 30^\circ$ are scattered into the loss cone during one pass through the wave. A variable mesh size in $v_{||}$ is used with mesh size increasing with $v_{||}$. About 85 bins in $v_{||}$ covering the range from $v_{||} = 1.87 \times 10^4$ km/sec (parallel energy ~ 1 keV) to $v_{||} = 6.01 \times 10^4$ km/sec (parallel energy ~ 10 keV) were used with mesh sizes ranging from 0.1% to 2.8%. The resonance points are at the equator for the 1 keV particles and at $\pm 20^\circ$ for particles at 10 keV parallel energy (assuming $\alpha_{eq} \approx 15^\circ$). Altogether about 40,000-50,000 test particles are used for each computation.

The initial unperturbed distribution is taken to be of the form

$$f(v, \alpha) = \frac{A}{v^4} g(\alpha) \quad (5.4)$$

where A is a constant and $g(\alpha)$ is some function of pitch angle. The energy variation of $f(v, \alpha)$ is reasonable compared to particle data [Schield and Frank, 1970]. In our computations we consider two different distribution functions

(a) an isotropic distribution for which

$$\begin{aligned} g(\alpha) = g_1(\alpha) &= 1 & \alpha > \alpha^{1c} \\ &= 0 & \alpha < 0 \end{aligned} \quad (5.5)$$

and

(b) an anisotropic distribution with

$$\begin{aligned} g(\alpha) = g_2(\alpha) &= 0.2 \sin^{0.2} \alpha + 0.8 \sin^{12} \alpha & \alpha > \alpha^{1c} \\ &= 0 & \alpha < \alpha^{1c} \end{aligned} \quad (5.6)$$

The two distributions have the same value at $\alpha = 90^\circ$ and they are sketched in Fig. 5.2. Both isotropic and anisotropic distributions have been measured in the magnetosphere [Lyons and Williams, 1975]. The particular anisotropic distribution of Fig. 5.2b was measured by Anderson [1976] and is considered to be highly anisotropic.

Note that both distributions of Fig. 5.2 are essentially flat for $0 < \alpha < 30^\circ$. In our computations of the precipitated flux due to one pass through the wave we only consider particles with $\alpha < 30^\circ$. Therefore for the purposes of the computer simulation both distributions can be treated as isotropic, but with different flux levels above the loss cone.

(a) isotropic case

In this case the initial unperturbed distribution is

$$\begin{aligned} f(v_{\parallel}, \alpha) &= \frac{A \cos^4 \alpha}{v_{\parallel}^4} & \text{for } \alpha > \alpha^{1c} \\ &= 0 & \text{for } \alpha < \alpha^{1c} \end{aligned} \quad (5.7)$$

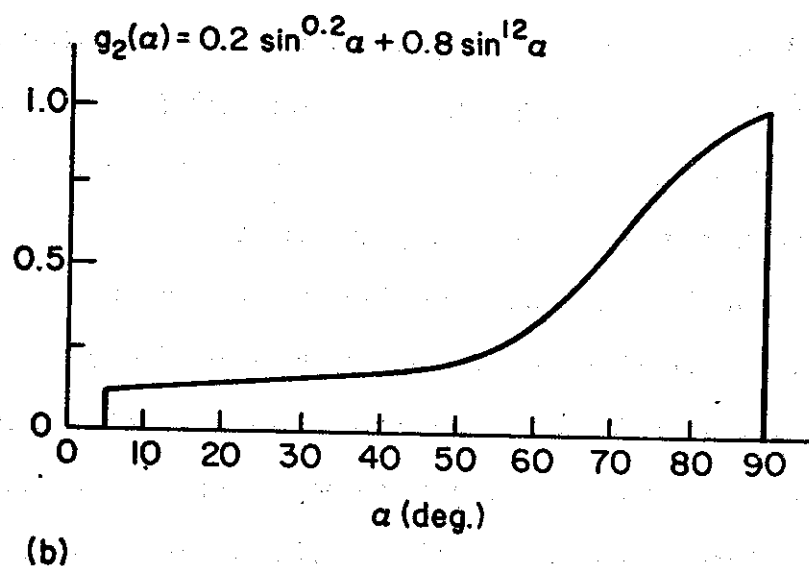
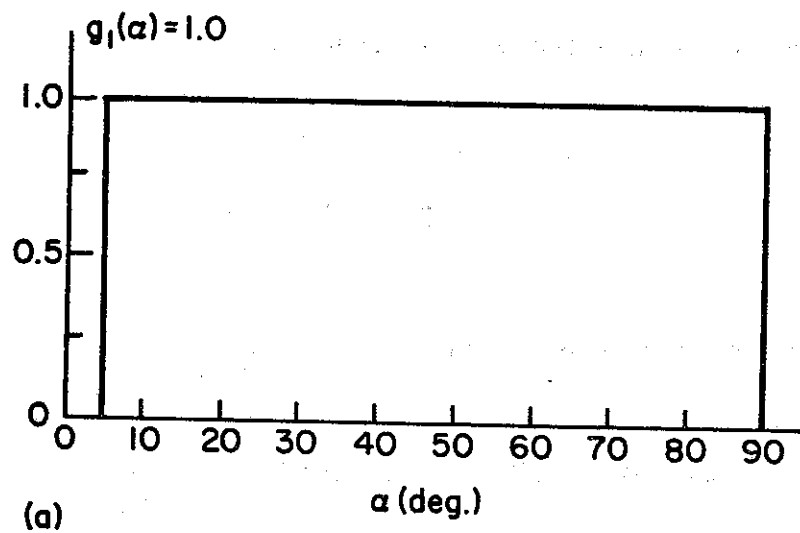


FIGURE 5.2 PITCH ANGLE DEPENDENCE OF THE TWO DISTRIBUTION FUNCTIONS USED IN THE CALCULATIONS. (a) an isotropic distribution, (b) an anisotropic distribution.

With this as the input distribution, the test particle simulation described in the last section is carried out and the perturbed distribution is obtained. The output of this computation is the value of the perturbed distribution at the $30 \times 85 = 2550$ mesh points, covering from $\alpha = 0^\circ - 30^\circ$ and $v_{\parallel} = v_k$ to $v_{\parallel} = \sqrt{10} v_k$ where $v_k = 1.9 \times 10^7$ m/sec is the velocity corresponding to 1 keV energy, such that $0.5 m v_k^2 \approx 1$ keV.

In the following, we concentrate on the 1-2 keV total energy band. First, in order to show the wave induced pitch angle perturbations of the distribution function we integrate the distribution over v_{\parallel} , to obtain:

$$f(\alpha) = 2\pi \int_{v_{\parallel} = v_k \cos \alpha}^{v_{\parallel} = \sqrt{2} v_k \cos \alpha} f(v_{\parallel}, \alpha) v_{\parallel}^2 dv_{\parallel} \quad (5.8)$$

where we again assume uniform distribution over ϕ .

Figure 5.3 shows the normalized distribution $f(\alpha)$ vs. α , for different wave intensities. The dashed lines show the unperturbed distribution which is isotropic above the loss cone as is clear from (5.7). The solid lines show the one-pass perturbed distribution. Note again that only the 1-2 keV total energy band is considered. The integral given in (5.8) is easily carried out with the computer, using the mesh point values $f(v_{\parallel}, \alpha)$ and $\Delta v_{\parallel} \approx dv_{\parallel}$, and approximating the continuous integral by a weighted sum of finite number of values of $f(v_{\parallel}, \alpha)$.

For $B_w = 1 m\gamma$ the perturbations are small and only a small percentage of the particle population from the range just above the loss cone have been precipitated. For $B_w = 10 m\gamma$ we see that the loss

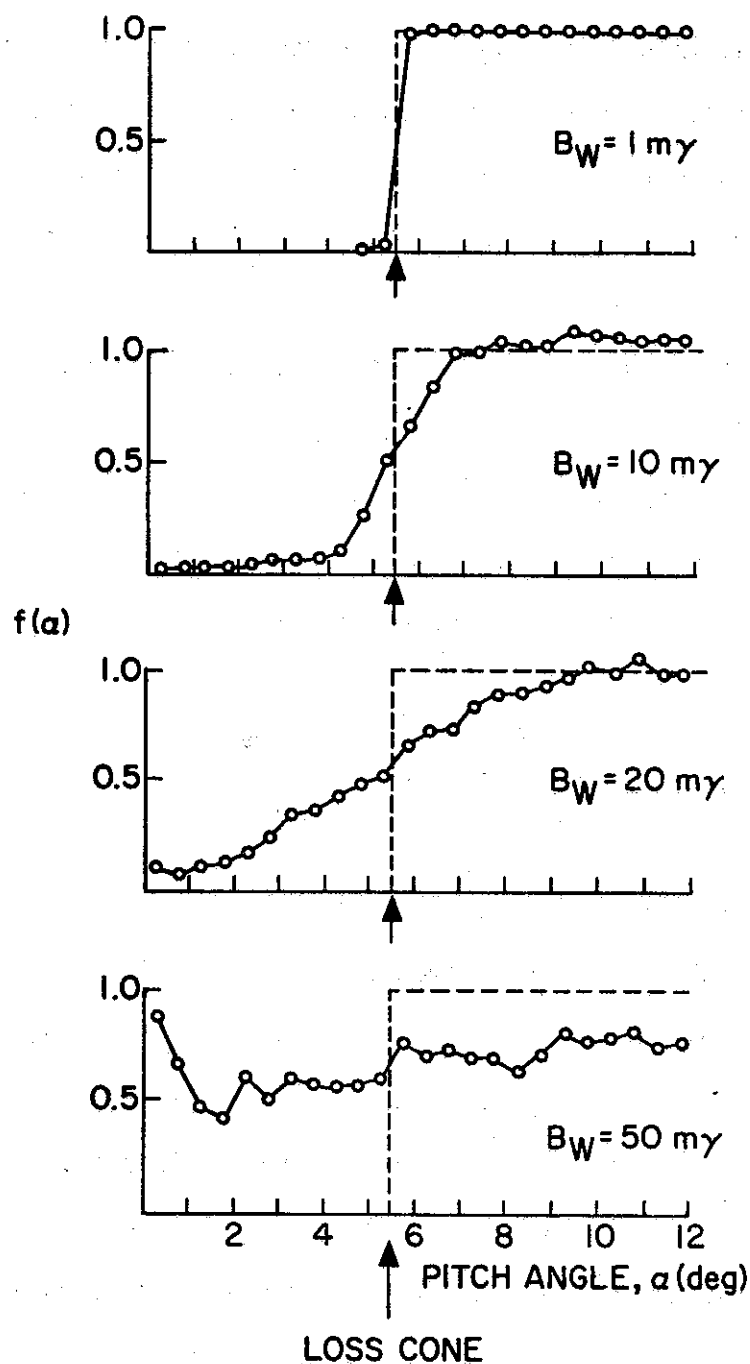


FIGURE 5.3 NORMALIZED PARTICLE DISTRIBUTION $f(\alpha)$. The dashed lines represent the unperturbed distribution which is isotropic in pitch angle. The solid lines represent the one-pass perturbed distribution. Note that the number density in any given range $d\alpha$ is equal to $f(\alpha)\sin\alpha d\alpha$.

cone is partly filled with particles scattered down from higher pitch angles. As can be seen from the figure most of the particles scattered into the loss cone originally had pitch angles in the 2-3° range just above the loss cone. For $B_w = 20 \text{ m}\gamma$ and $50 \text{ m}\gamma$ we observe that the number of precipitated electrons is higher than for $B_w = 10 \text{ m}\gamma$ and there are more particles deeper into the loss cone. Also by observing the distribution at pitch angles above the loss cone we see that contributions to the loss cone population come from a wider range of pitch angles for higher wave intensities.

The total number density of precipitated electrons in the 1-2 keV energy range is given by:

$$N_T = 2\pi \int_0^{\alpha^{1c}} \int_{v_{\parallel} = v_k \cos \alpha}^{\sqrt{2} v_k \cos \alpha} f(v_{\parallel}, \alpha) v_{\parallel}^2 \frac{\sin \alpha}{\cos^3 \alpha} dv_{\parallel} d\alpha [L^3 (1 + 3 \sin^2 \lambda_i)^{1/2}] \quad (5.9)$$

where α^{1c} is the loss cone angle (5.5° at equator for $L = 4$) and the last factor $L^3 (1 + 3 \sin^2 \lambda_i)^{1/2}$ is due to the convergence of the field lines which gives a reduced flux tube cross section at the ionosphere as compared to that at the equator. In this case λ_i would be the latitude at which the $L = 4$ field line crosses ionospheric heights, i.e., $\lambda_i = 60^\circ$. Note that all evaluations in the integrand are done using equatorial values whereas N_T is the precipitated number density at the ionosphere. The precipitated energy deposition rate in the same range is:

$$Q = 2\pi \int_0^{\alpha} \int_{v_{\parallel} = v_k \cos \alpha}^{\sqrt{2} v_k \cos \alpha} f(v_{\parallel}, \alpha) v_{\parallel}^2 \frac{\sin \alpha}{\cos^3 \alpha} \left(\frac{1}{2m} \frac{v_{\parallel}^2}{\cos^2 \alpha} \right) (v_{\parallel}) dv_{\parallel} d\alpha [L^3 (1 + 3 \sin^2 \lambda_{\perp})^{1/2}] \quad (5.10)$$

Both integrations (5.9) and (5.10) reduce to finite weighted sums in our computer formulation. With the perturbed distribution $f(v_{\parallel}, \alpha)$ obtained at the mesh points, N_T and Q are evaluated without difficulty. For $B_w = 10$ mG we obtain

$$N_T = 9.5 \times 10^{-11} A \text{ cm}^{-3} \quad (5.11)$$

and

$$Q = 4.2 \times 10^{-10} A \text{ ergs/cm}^2\text{-sec} \quad (5.12)$$

where A is the proportionality constant in (5.4) and (5.7).

The constant A can be evaluated in terms of measured number density as follows. Assume a total number density in the 1-2 keV energy range of N_e el/cc isotropically distributed in pitch angle. Then,

$$N_e = 2\pi \int_0^{\pi} \int_{v=v_k}^{\sqrt{2} v_k} \frac{A}{v^4} v^2 \sin \alpha dv d\alpha \quad (5.13)$$

From the above we obtain

$$A = 5.2 \times 10^8 N_e \quad (5.14)$$

Substituting (5.14) in (5.11) and (5.12) we have

$$N_T = 0.05 N_e \text{ cm}^{-3} \quad (5.15)$$

and

$$Q = 0.2 N_e \text{ ergs/cm}^2\text{-sec} \quad (5.16)$$

The above results are for $B_w = 10 \text{ mV}$. Figure 5.4 shows the energy deposition rate as a function of wave intensity. The dashed straight line gives the results predicted on the basis of linear theory. The vertical scale on the left is normalized to $|N_e|$. The one on the right is normalized to $|\phi_1|$, the differential energy spectrum for $\alpha \approx 90^\circ$ particles with $\sim 1 \text{ keV}$ energy. As seen from Fig. 5.4 the precipitated flux increases with wave intensity for $B_w \leq 40 \text{ mV}$ and begins to saturate for $B_w > 40 \text{ mV}$. The variation should be compared to that of the rms scattering given in Fig. 4.6.

Schild and Frank [1970] have reported measurements of low energy electrons on the OGO-3 satellite. Figure 6 of their paper indicates number densities of 3 el/cc in the energy range $750 \text{ eV} \leq E \leq 50 \text{ keV}$ inside the plasmopause at $L \approx 4$. Figure 4 of the same paper indicates that number density varies as v^{-4} with velocity (E^{-2} with energy). Using this type of energy dependence we obtain $N_e = 1 \text{ el/cc}$ in the 1-2 keV range. Using (5.15) and (5.16) we then have a precipitated number density of $N_T = 0.05 \text{ cm}^{-3}$ and a flux of $Q = 0.22 \text{ ergs/cm}^2\text{-sec}$ for $B_w = 10 \text{ mV}$ wave intensity.

The energy deposition rate can also be expressed in terms of the differential energy spectrum [Schild and Frank, 1970]. The differential energy spectrum ϕ in $\text{el/cm}^2\text{-ster-sec-keV}$ is given by

$$\phi = \frac{f(v, \alpha) v^2 dv \sin \alpha d\alpha d\phi}{d\Omega dE} \quad (5.17)$$

ONE-PASS PRECIPITATED FLUX (ergs/cm²-sec) IN THE 1-2 keV RANGE

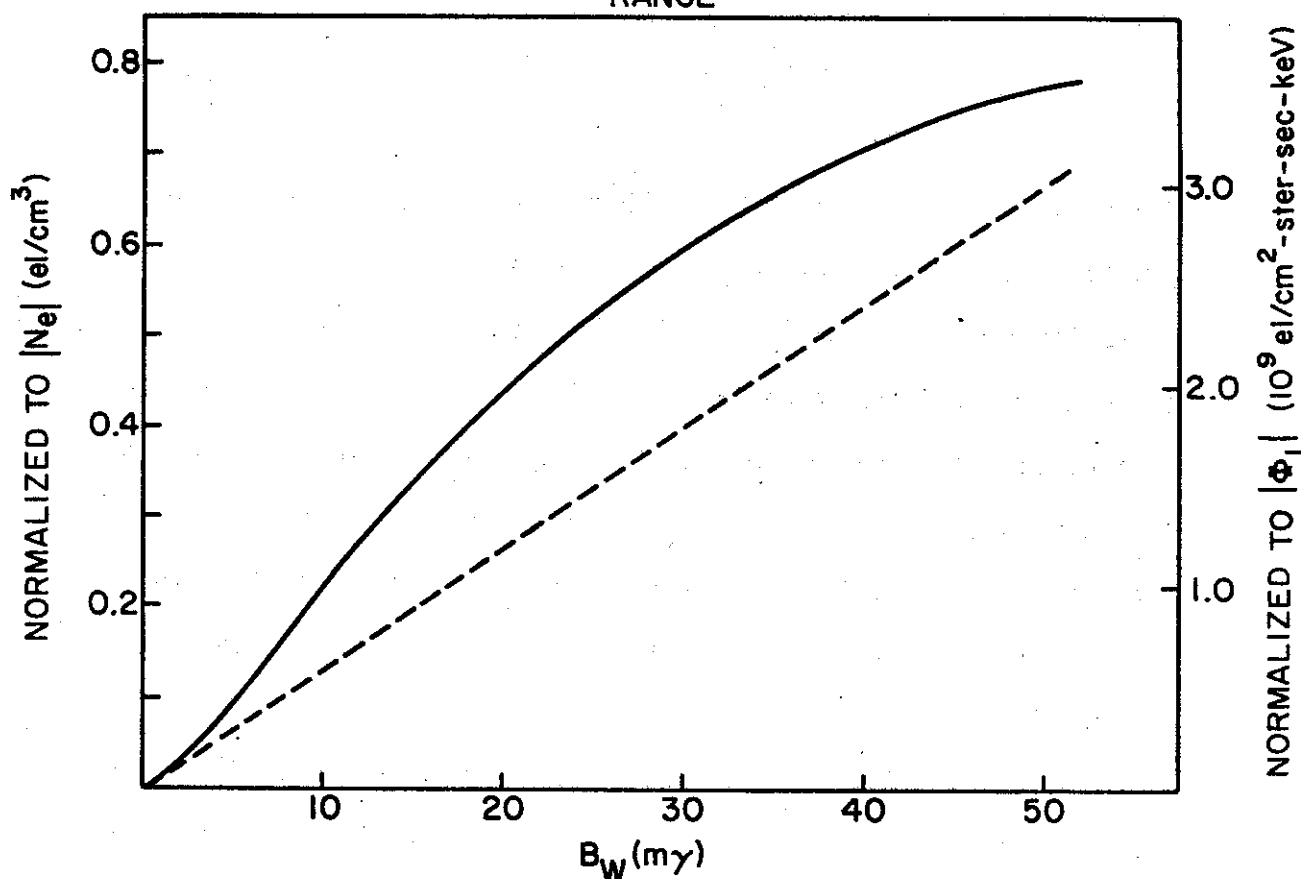


FIGURE 5.4 THE ONE-PASS PRECIPITATED FLUX IN THE 1-2 keV RANGE AS A FUNCTION OF WAVE INTENSITY. This result is for an isotropic distribution. The vertical scale on the left gives the flux (ergs/cm²-sec) normalized to $|N_e|$ where N_e is the electrons per cm³ in the 1-2 keV range. The one on the right gives flux normalized to $|\Phi_1|$, the differential energy spectrum in el/cm²-ster-sec-keV, for ~1 keV electrons at $\alpha \approx 90^\circ$.

where $d\Omega = \sin\alpha d\alpha d\phi$ and $dE = mv dv$ are the solid angle and energy differentials respectively. In the case of an isotropic distribution $f(v, \alpha) = A/v^4$ and Φ is the same for all pitch angles. Substituting above we obtain

$$A = 2 \Phi_1 \quad (5.18)$$

where ϕ_1 is the differential energy spectrum in $\text{el/cm}^2\text{-ster-sec-keV}$ for the ~ 1 keV electrons. Substituting (5.18) in (5.11) and (5.12) we have

$$N_T = 1.9 \times 10^{-10} \phi_1 \text{ cm}^{-3} \quad (5.19)$$

and

$$Q = 1.0 \times 10^{-9} \phi_1 \text{ ergs/cm}^2\text{-sec} \quad (5.20)$$

for $B_w = 10$ mG. The energy deposition rate as a function of wave amplitude is shown in Fig. 5.4, where the vertical scale on the right is normalized to ϕ_1 .

A more recent measurement of low energy electron fluxes on the Explorer 45 (S^3) satellite was reported by Anderson [1976]. For disturbed pre-midnight conditions and for ~ 1 keV electrons with isotropic distributions the energy spectrum ϕ_1 is of the order of $\sim 10^8$ $\text{el/cm}^2\text{-ster-sec-keV}$. Substituting in (5.20) we obtain energy deposition rate $Q \approx 0.1 \text{ ergs/cm}^2\text{-sec}$.

(b) anisotropic case

For this case the initial unperturbed distribution is given as

$$f(v_{\parallel}, \alpha) = \frac{A \cos^4 \alpha}{v_{\parallel}^4} [0.2 \sin^{0.2} \alpha + 0.8 \sin^{12} \alpha] \quad \text{for } \alpha > \alpha^{1c} \quad (5.21)$$

$$= 0 \quad \text{for } \alpha < \alpha^{1c}$$

The pitch angle dependence $g(\alpha) = 0.2 \sin^{0.2} \alpha + 0.8 \sin^{12} \alpha$ is plotted in Fig. 5.2. For $\alpha < 30^\circ$ this distribution can be approximated by

$$f(v_{\parallel}, \alpha) \approx (0.15)A \frac{\cos^4 \alpha}{v_{\parallel}^4} \quad \alpha^{1c} < \alpha < 30^\circ$$

$$= 0 \quad \alpha \leq \alpha^{1c}$$
(5.22)

When the distribution given by (5.23) is used as the initial distribution in our simulation, the results should be the same as those for the distribution given by (5.7) within a factor 0.15. Therefore we have for this anisotropic case and for $B_w = 10 \text{ m}\gamma$,

$$N_T = 9.48 \times 10^{-11} \times (0.15)A = 1.42 \times 10^{-11} A \text{ cm}^{-3} \quad (5.23)$$

and

$$Q = 4.23 \times 10^{-10} \times (0.15)A = 6.35 \times 10^{-11} A \text{ ergs/cm}^2\text{-sec} \quad (5.24)$$

where A is the proportionality constant in (5.9) or (5.23).

The differential energy spectrum (defined in (5.17)) for the distribution given in (5.21) is:

$$\Phi = \frac{A}{2E} [0.2 \sin^{0.2} \alpha + 0.8 \sin^{12} \alpha] \quad (5.25)$$

where E is the energy. Substituting $E \approx 1 \text{ keV}$ and $\alpha = 90^\circ$, we obtain:

$$A = 2 \Phi_1 \quad (5.26)$$

where Φ_1 is the spectrum in $\text{el/cm}^2\text{-ster-sec-keV}$ for $\sim 1 \text{ keV}$ electrons at $\alpha = 90^\circ$. That this is the same relation as (5.18) is not surprising since the two distributions shown in Fig. 5.2 were chosen to have the same value at $\alpha = 90^\circ$. Substituting (5.26) in (5.23) and (5.24) we have for $B_w = 10 \text{ m}\gamma$

$$N_T = 2.8 \times 10^{-11} \phi_1 \text{ cm}^{-3} \quad (5.27)$$

$$Q = 1.3 \times 10^{-10} \phi_1 \text{ ergs/cm}^2\text{-sec} \quad (5.28)$$

We again use the data reported by Anderson to find absolute values for the energy deposition rate. For ~ 1 keV electrons with anisotropic distributions similar to that of Fig. 5.2, the differential energy spectrum for $\alpha = 90^\circ$ particles $\phi_1 \approx 10^8 \text{ cm}^{-2}\text{ster}^{-1}\text{sec}^{-1}\text{keV}^{-1}$. Substituting in (5.28) we obtain $Q = 1 \times 10^{-2} \text{ ergs/cm}^2\text{-sec}$.

These values show that the one-pass fluxes in the 1-2 keV range precipitated by a 10 mV CW signal at 5 kHz can be as much as 1×10^{-2} to $0.2 \text{ ergs/cm}^2\text{-sec}$ depending on the anisotropy of the distribution function. Such fluxes are well within the resolution of most particle detectors. The intensities approach that of a moderate aurora.

C. LEVERAGE

As was shown in section 2.E, large pitch angle changes induced by the wave on particles do not necessarily require a large amount of energy exchange in the cyclotron resonance interaction. The basic reason for this is the fact that the wave perturbations are mainly through the wave magnetic field which changes the direction of momentum (i.e., pitch angle) of the particle without energy transfer.

We have shown in the previous section that energy fluxes of as much as $0.2 \text{ ergs/cm}^2\text{-sec}$ can be precipitated by waves of 10 mV intensity. It is instructive to compare the energy density of the precipitated flux and that of the input wave and compute the leverage involved in the

wave induced precipitation process.

For longitudinal whistler-mode propagation the wave Poynting flux is given by

$$|\bar{P}| = |E_w \times H_w| = |E_w| |H_w| = \left| \frac{\omega}{k} B_w \right| \left| \frac{B_w}{\mu_0} \right| = \left| \frac{\omega}{k \mu_0} \right| |B_w|^2 \quad (5.29)$$

Using $n = \frac{kc}{\omega}$, (5.29) can be expressed in terms of the refractive index as

$$|\bar{P}| = \frac{c}{n \mu_0} |B_w|^2 = \frac{2.5 \times 10^{-10}}{n} |B_w|^2 \frac{\text{watts}}{\text{m}^2} \quad (5.30)$$

where B_w is in milligammas. For the parameters of Table I used for our computations, the refractive index $n \approx 40$ at the equator. Using this together with a $B_w = 10$ mγ we obtain from Eq. (5.30) the wave energy flux

$$|\bar{P}| \approx 6 \times 10^{-9} \text{ watts/m}^2$$

A precipitated flux of $0.2 \text{ ergs/cm}^2\text{-sec}$ is equivalent to an energy density of about $0.2 \times 10^{-3} \text{ watts/m}^2$. This shows that the leverage involved in this interaction is $\sim 10^5$ or 50 dB. Therefore significant particle fluxes can be precipitated by waves of moderate intensity.

The above calculations have compared the energy densities. We can also consider the total input and output power and compute the leverage on an integrated basis. The Siple VLF transmitter operates with a total radiated power ranging from 100 W to 1 kW. Assuming that the precipitated flux is distributed over an area which is 100 km in radius, the total precipitated power is $\sim 10^7$ watts, a factor of $\sim 10^5$ larger than the radiated power. Hence the power leverage of the interaction is ~ 50 dB. The input power of the transmitter is ~ 100 kW. Since an output of

$\sim 10^7$ watts is obtained the net power gain is ~ 20 dB. The source of this extra power is of course the energy of the trapped energetic particles.

Note that these numbers are only considering the 1-2 keV energy band. The same wave will also precipitate particles with higher energies. Therefore the total leverage and the power gain are likely to be larger than those computed above. Furthermore we have implicitly assumed that 100 kW of input power is necessary for generating a 10 mV signal. This is very likely to be an over estimate. Recent results from a power-step (up and down) experiment using the Siple transmitter has showed that the same magnetospheric signals could be produced with lower power levels [R. A. Helliwell, private communication].

D. IONOSPHERIC EFFECTS

In this section we investigate the effects in the nighttime ionosphere of the wave induced precipitation fluxes computed in the previous sections.

The precipitating electrons impinge on the lower ionosphere, where they produce numerous secondary electrons and create an impulsive ionization enhancement throughout the volume of the precipitation region. As a result the ionospheric conductivity in the same volume is also enhanced. The incoming electrons with higher energies penetrate to lower altitudes and produce Bremsstrahlung x-rays which are detected by balloon measurements.

The ionospheric density enhancements produced by an incoming flux of electrons at a given energy can be roughly estimated using the results of Banks et al. [1974] and Bailey [1968]. Figure 9 of Banks et al.

[1974] gives the ionization rates per unit incident flux for monoenergetic fluxes in the range 0.42-10 keV. Bailey [1968] gives the ion pair production rates for energies up to 150 keV.

In previous sections we have computed an energy deposition rate of 0.2 ergs/cm²-sec for electrons in the 1-2 keV energy range. This flux can be approximated as a monoenergetic beam of precipitating electrons of energy 1.5 keV.

The flux computation of section 7.B was done for particles with 1-10 keV parallel energy, but in that section we discussed only the 1-2 keV flux. The precipitated flux for higher energies can also be obtained from the same computer output. For instance, in the 6.5 to 7.5 keV range (average energy 7 keV) the flux is 6×10^{-2} ergs/cm²-sec. Although the simulation is carried out only up to 10 keV we can assume linear theory and extrapolate to higher energies. This assumption is justified since we have shown that linear theory applies for resonances sufficiently far from the equator. Particles with parallel energies greater than 10 keV resonate at latitudes beyond 20° and linear theory can be comfortably used. In linear theory the rms scattering is approximately proportional to $\frac{1}{v_{\parallel}}$ or $(E)^{-1}$ where E is the parallel energy. The precipitated flux is not reduced by $\frac{1}{v_{\parallel}}$, since for the same number density, particles with higher energy constitute a larger flux. Extrapolating from the computed 7 keV flux to 30 keV using linear theory we obtain $\sim 2 \times 10^{-2}$ ergs/cm²-sec, in the 29.5 to 30.5 keV range.

Figure 5.5 shows the ionospheric density enhancements produced by these three computed monoenergetic incoming fluxes with energies 1.5±0.5 keV, 7±0.5 keV and 30±0.5 keV. The density enhancements are

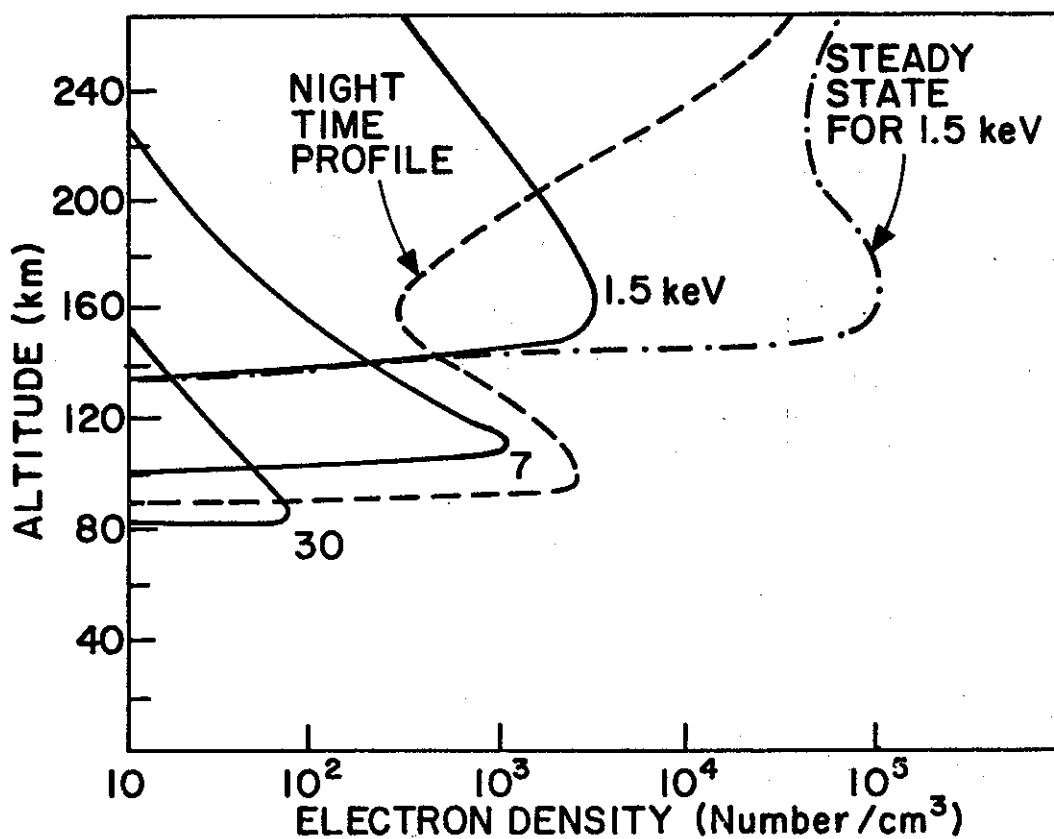


FIGURE 5.5 PRECIPITATION INDUCED DENSITY ENHANCEMENTS PRODUCED BY THREE MONOENERGETIC INCOMING FLUXES AT 1.5, 7 AND 30 keV. The solid lines represent the enhancements due to a precipitation pulse of one second duration. The steady state due to 1.5 keV flux is also shown.

computed assuming a one-second duration of precipitation of these monoenergetic beams. It is assumed that there is negligible recombination in this brief period. We have used the results of Banks et al. [1974] and Bailey [1968] to roughly estimate the density enhancements. We have also given the steady state density enhancement for the 1.5 keV flux assuming a flux of $0.2 \text{ ergs/cm}^2\text{-sec}$ is continuously impinging on the ionosphere. For the steady state computation we have used for altitudes

up to 200 km, the relation

$$\frac{dN}{dt} = q - \psi N^2$$

where N is the electron density, q is the volume rate of production of electron ion pairs and ψ is the effective loss coefficient (due to recombination and attachment) for electrons. We have used a value of ψ of about $2 \times 10^{-7} \text{ cm}^3/\text{sec}$ in the 80-200 km altitude range [Bailey, 1968]. For altitudes above 200 km the continuity equation (neglecting diffusion) becomes

$$\frac{dN}{dt} = q - \beta N$$

and the loss coefficient β is in the range $10^{-4} - 10^{-3} \text{ cm}^{-3} \text{ sec}^{-1}$ [Park and Banks, 1974]. These values are used in our calculations of the steady state flux for altitudes above 200 km.

Note that a 5 kHz, 10 mV wave at $L = 4$ will precipitate electrons at all energies above 1 keV. We have shown in Fig. 5.5 the perturbations due to only three monoenergetic components of the incoming flux. Using a more accurate computation the total enhancement profile can be obtained from an incoming precipitated flux with given energy spectrum. Elaborate computer programs which give the ionospheric density enhancements due to a given spectrum of precipitated flux do exist and are widely used for studying the penetration of the auroral electrons into the atmosphere [Walt et al., 1969; Banks et al., 1974].

For comparison, an average typical ambient nighttime electron density profile [Hanson, 1961] is also shown in Fig. 5.5. These results show that significant perturbations in the nighttime electron density over the 80-250 km altitude range can be produced by one-second duration

precipitation pulses. The perturbation caused by the 1.5 keV flux could be measured with ionosondes. The enhancements caused by the 30 keV flux occur at low altitudes and could cause detectable modifications in the subionospheric VLF propagation [Helliwell et al., 1973]. These density enhancements also result in significant enhancements in the ionospheric conductivity and could conceivably give rise to micropulsation activity [Bell, 1976].

In addition to density enhancements the computed precipitation fluxes of $\sim 10^{-1}$ ergs/cm²-sec are intense enough to cause enhanced atmospheric photo emission which could be measured by photometers.

VI. CONCLUSIONS AND DISCUSSION

A. SUMMARY

We have analyzed the nonlinear gyroresonance interaction between energetic electrons and coherent VLF waves in the magnetosphere. This mechanism is important since it is believed to produce strong wave-particle interactions in the magnetosphere with large resultant pitch angle and energy scattering of the energetic electrons. Some examples of coherent VLF waves which are thought to be involved in this strong nonlinear interaction include natural whistlers [Helliwell et al., 1973], naturally and artificially triggered VLF emissions [Stiles and Helliwell, 1975], signals from VLF ground transmitters [Helliwell and Katsufakis, 1974], and harmonic waves from large scale power grids [Helliwell et al., 1975; Park, 1976]. An additional future source of coherent VLF waves in the magnetosphere may be VLF wave-injection experiments using satellite borne transmitters.

In our study we have focused on magnetospheric parameters appropriate for the $L = 4$ field line. This is the approximate location of the Siple VLF transmitter in Antarctica, the source of much of the data concerning nonlinear interactions between the coherent VLF waves and energetic electrons in the magnetosphere.

We have used a computer simulation of the full nonlinear equations of motion for energetic particles interacting with a longitudinal whistler mode wave in an inhomogeneous magnetoplasma. We have studied, in detail, interaction of single particles, sheets of particles uniformly distributed in phase and a full distribution of particles with a given wave. The interaction of a full particle distribution is studied with a

test particle approach. In this approach, in order to estimate the perturbation of the full distribution, complete trajectories of sufficient number of particles distributed appropriately in phase space are computed.

We have shown how the nonlinear pitch angle scattering varies as a function of particle pitch angle, wave amplitude, cold plasma density, and resonance position along the magnetic field line. We have compared the nonlinear theory with the well-known linear theory and have derived a convenient quantitative criterion for determining the applicability of linear theory in any particular case. In particular, our results indicate that nonlinear effects are significant for wave amplitudes as low as 3 mV for a 5 kHz signal near the magnetic equatorial plane at $L \approx 4$. Detailed study of the strong trapping and scattering case have shown that significant pitch angle changes can be induced in the energetic particle population. These results indicate that at high wave amplitudes even particles with very high pitch angles ($> 60^\circ$) can be scattered into the loss cone in a single encounter with the wave.

Our full distribution calculations show that significant precipitated energetic electron fluxes can be produced with moderate strength VLF waves. For example our results indicate that at $L \approx 4$ a 10 mV, 5 kHz wave can produce a precipitated energy flux of 1-2 keV electrons of as much as 10^{-1} ergs/cm²-sec, the exact value depending upon the value of the energetic electron distribution function near the loss cone. We have shown that significant leverage is involved in the wave induced particle precipitation process. Typically, the energy density of the precipitated flux is 50-60 dB higher than that of the wave. We have computed the ionospheric perturbations due to these precipitated fluxes

and have shown that significant density enhancements can be induced in the night-time ionosphere.

In summary, we have shown that significant energetic electron pitch angle scattering and precipitation can be produced by coherent VLF waves of moderate amplitude during nonlinear cyclotron resonance interactions in inhomogeneous magnetoplasmas. This type of scattering has not previously been considered in the large volume of work which has appeared in the literature over the last decade concerning energetic particle pitch angle scattering in the magnetosphere. Although it remains to be seen what role coherent wave scattering plays in determining the large scale characteristics of energetic electrons in the magnetosphere, it is clear that this type of scattering should play an important part in VLF wave-injection experiments, both from the ground and in space.

B. MEASUREMENT OF THE PRECIPITATED FLUX

Assuming that our calculations are correct and that an energetic electron flux of 10^{-1} ergs/cm²-sec can be precipitated into the atmosphere during VLF wave injection experiments, the question arises as to how this flux or the ionospheric perturbations produced by this flux can be detected.

The most direct method of detection is to employ satellite particle detectors. However this method has drawbacks at both high and low altitude. At high altitude near the magnetic equatorial plane the precipitating fluxes are less intense and the particle detectors must be directed into the loss cone. Since the half angle of the loss cone is very small, ($\sim 5^\circ$ at $L \sim 4$) the pointing accuracy of the detector must be high and its angular resolution must be at least equal to the loss cone half

angle. At low altitude (~500 km) the loss cone half angle approaches 90° and the detector pointing accuracy and angular resolution are not critical parameters. However the satellite velocity is high (~7 km/sec) and the region of precipitation may be small (~100 km scale) so that the time available for flux measurements may be severely limited.

A second method involves the use of photometers at ground stations such as Siple Station, Antarctica. If an experiment lasts for several weeks, there is a good probability that the precipitation region will sometimes be located within 100 km of the transmitter. In this case enhanced photo emission from the atmosphere should be readily detectable on the ground near the transmitter if the precipitated flux exceeds $0.01 \text{ ergs/cm}^2\text{-sec}$. Recent photometer measurements at Siple Station have shown that significant enhancements in the photometer output can be produced by precipitation induced by VLF whistler-mode noise bursts at 2-4 kHz [J. Doolittle, private communication].

A third method makes use of precipitation induced modification of the D region. In this effect the energetic electrons are precipitated into the atmosphere, penetrate the D layer and change the properties of the earth-ionosphere waveguide, altering their amplitude and/or phase of VLF waves propagating over long distances (~1000 km) in the waveguide. This type of modification has been observed to occur because of scattering of energetic electrons by whistlers [Helliwell et al., 1973]. It appears that the same type of interaction should take place whether the coherent input scattering wave is a signal from a VLF transmitter, a natural whistler or a discrete emission. Thus wave-induced particle precipitation events may be detectable through this effect. Our calcu-

lations indicate that the flux of electrons of energy 30 ± 0.5 keV precipitated by a CW input wave of 10 mV amplitude and a frequency of 5 kHz should lie in the range 10^{-2} - 10^{-3} ergs/cm²-sec, depending upon the value of the particle distribution function near the loss cone. This flux produces a substantial electron density enhancement below the nighttime D layer and should lead to detectable perturbations in the VLF waves propagating in the earth-ionosphere waveguide.

One other method of precipitation detection is high altitude balloon measurements of the Bremsstrahlung x-rays produced by the precipitating electrons. Rosenberg et al. [1971] have measured one-to-one correlation between VLF emissions and bursts on the balloon x-ray measurements.

Additional methods of precipitation detection include riometer and ionosonde techniques.

C. INTENSITY OF COHERENT WAVES IN THE MAGNETOSPHERE

Although we have presented our results for a wide range of wave intensities we have, from time to time, stressed the results for a 10 mV wave amplitude. Such a wave intensity is a reasonable estimate of the amplitude of coherent whistler mode waves in the magnetosphere. The evidence for this comes predominantly from high altitude satellite data. For instance the amplitude of the navigational VLF stations NAA (17.8 kHz) and NPG (18.6 kHz) were often measured by a VLF experiment on the high altitude satellite OGO 1 when this satellite crossed the magnetic field lines linking the transmitters ($L \approx 3$). It was found that 10 mV was a representative amplitude for the transmitter signals near the magnetic equatorial plane [Heyborne, 1966]. This wave amplitude was asso-

ciated with a radiated power output of one megawatt for NAA and 1/4 megawatt for NPG.

The amplitude of VLF waves in the magnetosphere produced by the relatively low power (output ≤ 1 KW) Siple Station transmitter has been measured only once to date. On this occasion a wave amplitude of 0.3 mV was measured on the high altitude satellite IMP-6 when at a latitude of 20°S on the field lines ($L \sim 4$) linking the transmitter [Inan et al., 1977a]. Since the satellite intercepted the signal on the transmitter side of the equator and before the signal has traveled once over the field line, it was concluded that this was an unamplified wave amplitude. Considering the commonly observed 20-30 dB amplification of VLF signals in the magnetosphere [Helliwell and Katsufurakis, 1974], the signal intensity at the equator could be as high as 3-8 mV. The amplitude of the naturally occurring highly coherent VLF signals known as "chorus" has been measured on a number of satellites [Burtis and Helliwell, 1976; Tsurutani and Smith, 1974; Taylor and Gurnett, 1968]. The amplitude of these quasi-coherent signals near 5 kHz has typically been found to lie in the range 2-20 mV.

Furthermore, because of the high whistler mode radiation efficiency of dipole and loop antennas at VLF frequencies in the ionosphere and magnetosphere [Wang and Bell, 1972], it appears possible to produce a 10 mV wave near the magnetic equatorial plane on the $L = 3-5$ field lines using a Space-Shuttle based VLF transmitter of 1 kilowatt radiated power.

Similarly a high altitude satellite based VLF transmitter of 1 kilowatt output, which operated within a few thousand km of the magnetic equatorial plane, could be expected to produce a wave field exceeding

100 mV within 1000 km of the equatorial plane.

Thus a 10 mV amplitude is representative of highly coherent VLF wave types that are presently found, or that may be introduced in the future, in the magnetosphere. When these waves are present, strong pitch angle scattering of energetic electrons can be expected. Details of this scattering will depend upon the spectral form of the coherent wave. Our present results, which are based on the assumption of a fixed frequency wave, are meant to apply primarily to the case of VLF wave injection experiments involving fixed frequency inputs near the $L = 4$ field lines. These experiments can be either ground, space station or satellite based. However, our results can also be applied to the case of pitch angle scattering by chorus and whistler elements so long as the wave frequency changes slowly with time.

D. DISCUSSION

The particle scattering calculations presented in the main body of this report have been carried out under the assumption that the wave amplitude is reasonably constant over the region near the magnetic equatorial plane where significant scattering takes place. In other words, our calculations do not include the effects of the electromagnetic fields generated by the perturbed energetic particles. This assumption will be valid if the currents stimulated in the energetic particle population by the incident wave do not lead to significant damping or amplification of the wave near the magnetic equatorial plane. Although linear theory cannot describe the long term behavior of our system, the initial behavior of the system can be obtained from linear theory using the linear Boltzmann-Vlasov theory [Stix, 1962; Kennel and Petschek, 1966; Bernard,

1973]. It should be noted that many of the observed features of wave growth and emission generation in the magnetosphere, especially those that show generation of multiple frequencies and wave entrainment effects [Helliwell and Katsufakis, 1974; Helliwell et al., 1975; Raghuram et al., 1977], cannot be explained by using linear theory. Our argument in this section makes use of linear theory to describe the initial behavior of the system. The following expression can be derived for the asymptotic spatial growth rate for longitudinally propagating whistler mode waves in a homogeneous relatively cold magnetic plasma with a dilute energetic electron component:

$$k_{\perp} = \pi^2 \left(\frac{N_h}{N_c} \right) (\omega_H - \omega) \left[1 - \left(\frac{\omega_H}{\omega} - 1 \right) A \right] F(v_R) \quad (6.1)$$

where

$$A \equiv F^{-1}(v_R) \int_0^{\infty} \tan \alpha \left. \frac{\partial f_h}{\partial \alpha} \right|_{v_{\parallel} = v_R} v_{\perp} dv_{\perp}$$

$$F(v_R) = \int_0^{\infty} f_h(v_{\perp}, v_{\parallel} = v_R) v_{\perp} dv_{\perp}$$

and $f_h(v_{\perp}, v_{\parallel})$ is the normalized energetic electron distribution function; $v_R = \frac{\omega_H - \omega}{k}$ is the local resonance velocity, N_h is the total number of energetic (hot) electrons, N_c is the total number of cold electrons and it is assumed that $N_h \ll N_c$.

Although (6.1) is derived for a homogeneous plasma, it can be expected to hold point to point in a slowly varying plasma such as that of the magnetosphere. When this is the case, the total amplitude change over a distance S along the magnetic field lines can be obtained by

the relation

$$\bar{B}_F = \bar{B}_i e^{-\int_0^S k_i dz} \quad (6.2)$$

where \bar{B}_i and \bar{B}_F are the initial and final wave magnetic field intensities respectively.

Schild and Frank [1970] have reported quiet time electron fluxes measured on the high altitude satellite, OGO-3, on L shells ranging from 3 to 10. During the measurements (June, July, 1966) the satellite was located near local midnight at low magnetic latitudes.

Near L ~ 4, the differential energy spectrum, Φ , of electrons near 90° pitch angle could be closely fitted by the relation:

$$\Phi \approx 10^8 \left(\frac{E_0}{E} \right) \text{ electrons/cm}^2\text{-steradian-keV-sec} \quad (6.3)$$

where $E_0 = 1$ keV and $E \geq E_0$. If we assume that the electrons were isotropically distributed in pitch angle, then we can use (6.1) and (6.3) in conjunction with the parameters of Table 1 to determine the initial wave attenuation rate due to the presence of these energetic electrons. We obtain the result

$$k_i = -2.5 \times 10^{-3} \text{ km}^{-1} \quad (6.4)$$

For commonly accepted models of the cold plasma distribution along the earth's magnetic field lines it can be shown that the damping rate of (6.1) remains reasonably constant over a distance of approximately ± 4000 km about the magnetic equatorial plane near the L ~ 4 field line. In this case the linear theory predicts total damping at 5 kHz of

approximately 170 dB.

However, it can be shown [Dysthe, 1971; Palmadesso and Schmidt, 1971; Bud'ko et al., 1972] that the linear growth (damping) rate of (6.1) can apply at most over a distance $S_T = v_R \bar{t}_T$ where \bar{t}_T is the average trapping time of the energetic resonant particles. Assuming that the energetic electron distribution falls off as v^{-4} , we find (using the parameters of Table 1) that the trapping distance has the value $S_T = 400$ km and total wave intensity change over this distance is approximately -9 dB. Thus during the time of its validity, linear theory predicts a substantial wave damping due to the quiet time energetic electron fluxes. With damping of this magnitude it can be concluded that whistlers and other natural whistler-mode signals would not be able to propagate between hemispheres. However it is just in magnetically quiet periods that whistler and VLF emission activity tends to peak [Carpenter and Miller, 1976]. Thus it must be the case that quiet time energetic electron fluxes in the range 1-10 keV are generally not isotropically distributed with respect to pitch angle. This conclusion is supported by recent results from the Explorer 45 spacecraft which show large anisotropies in energetic electron pitch angle distributions during both quiet [Lyons and Williams, 1975] and disturbed [Anderson, 1976] periods in the premidnight sector near $L \sim 4$.

In the past, a number of workers [Bell and Buneman, 1964; Kennel and Petschek, 1966; Liemohn, 1967] have attributed the amplification of whistlers and the generation of VLF emissions to pitch angle anisotropies in the energetic electron distribution function. In fact the gain predicted by (6.1) can be quite high for moderate anisotropies. For ex-

ample if the flux of Schield and Frank is assumed to have a $\sin^2\alpha$ dependence, (6.2) predicts a total gain in wave intensity of about 100 dB at 5 kHz near $L \sim 4$ (6 dB per 400 km).

Although pitch angle anisotropies may play an important role in the amplification of whistler mode signals and in the generation of VLF emissions, the probability of observing such effects during a given quiet period is only about 25% [Carpenter and Miller, 1976]. The lack of significant wave-particle interactions during the remainder of the time has been attributed by Bernard [1973] to a relaxation of the energetic electron distribution function to a state of marginal stability where, in terms of (6.3), $A \approx (\frac{\omega_H}{\omega} - 1)^{-1}$ over a wide band of wave frequency. This relaxation may take place through the Kennel-Petschek [1966] mechanism, but does not necessarily require a large decrease in flux to achieve the marginally stable state. Thus it is possible that fluxes such as those reported by Schield and Frank can exist in a state of marginal stability in which injected whistler mode waves will not exchange a significant amount of energy with the energetic electrons. However, under these conditions a significant scattering of electrons into the loss cone can still take place. Thus our calculations can be expected to apply during magnetically quiet times following magnetic disturbances when the energetic electron distribution function has relaxed to a state marginally stable to injected whistler mode waves.

Our results will also be expected to apply whenever the quiet time energetic particle fluxes are significantly less than those reported by Schield and Frank [1970]. For instance Lyons and Williams [1975] report a quiet time energetic electron flux in the premidnight sector

which is almost two orders of magnitude lower than that reported by Frank for the midnight sector. Using the Lyons and Williams data in (6.1), we find that the assumption of isotropy leads to total attenuation of approximately 2 dB, while the assumption of a $\sin^2\alpha$ anisotropy leads to a total gain of approximately 2 dB. Clearly for these flux levels, the currents stimulated in the energetic particle distribution should have little effect on the wave amplitude. However it is also clear that the precipitated flux will be smaller in these cases where the ambient flux levels are low.

E. APPLICATIONS AND FUTURE IMPLICATIONS

One important conclusion of our study is that significant precipitated particle fluxes can be induced by coherent VLF signals from ground transmitters. The leverage involved in this interaction is very large. As shown in Chapter 5 the energy content of the precipitated flux is as much as 50-60 dB higher than that of the input wave. Thus our results indicate the possibility of controlled particle precipitation out of the radiation belts. Such controlled precipitation would have many conceivable applications, including the following:

- i) Study the physics of the aurora and the lower ionosphere, by controlling x-ray production, ionization, radiation, and recombination processes, chemical and transport processes, and the coupling between the ionosphere and the magnetosphere.

- ii) Control the conductivity and hence the current flow in the E and D regions of the ionosphere. It has been suggested that by varying such currents in a periodic manner ULF radiation in the micropulsation frequency range (1-10 Hz) could be produced [Bell, 1976].

iii) Control density enhancements in the D region of the ionosphere and change the properties of the earth-ionosphere waveguide, causing phase and amplitude scintillation of VLF waves in the waveguide. Thus controlled precipitation can be used to modify the D region for the benefit of VLF communication and navigation systems.

iv) The ionizing radiation from energetic particles trapped in the earth's radiation belts degrades the performance of solar cells and other sensitive equipment during high altitude space flights in the vicinity of the radiation belts. For manned missions this radiation is a serious health hazard to the crew. Controlled particle precipitation can be used to diminish the average energy in the radiation belts by reducing the number of trapped particles. This application requires relatively higher wave intensities ($> 50 \text{ mW}$). For this reason a satellite transmitter might be more suitable.

v) We have shown that large changes ($> 20^\circ$) in particle pitch angle can be induced by coherent VLF waves. Such pitch angle perturbations can be measured by present satellite detectors. Thus it seems possible to use controlled perturbations of the trapped particle distribution function in the magnetosphere in order to study the physics of the radiation belt particles.

vi) The cyclotron resonance interaction that we have studied here will be present in a wide range of plasmas, both natural and manmade. Thus our results could aid in the understanding of laboratory plasmas and plasma physics in general.

vii) As a very long term application, we can speculate that controlled particle precipitation may one day be used to modify weather

processes. The precipitated flux locally heats the ionosphere and this heat may be convected down to the atmosphere thereby changing the stratospheric temperature and affecting the weather. Much more data concerning coupling between the ionosphere and the atmosphere must be acquired before the feasibility of this idea can be evaluated.

F. SUGGESTIONS FOR FUTURE WORK

We have presented a computer simulation of the complete trajectories of a distribution of radiation belt particles interacting with a given longitudinal whistler mode wave in the magnetosphere. We list below some possible extensions of this work:

i) Iteration: In Chapter 5, we have computed the precipitated flux from 'one pass' of the wave allowing each particle in the initial distribution to interact only once with the wave. The result is a one-pass perturbed distribution. One obvious straightfoward extension is to iterate the procedure. That is, to repeat the calculations using as the initial distribution the one-pass perturbed distribution. Iterating further, the time development of the precipitated flux and the distribution function can be calculated. In order for this iteration to reach a steady state the source function must be taken into consideration. Two natural source functions are those provided by particle injection from the tail and convective injection through radial and azimuthal drifts (see section 2.B).

ii) Non-longitudinal propagation: In our formulation we have considered only longitudinally propagating whistler-mode waves. For waves propagating at non-zero wave normal angles both the electric and magnetic fields of the wave have components along the static magnetic field.

In addition, the transverse polarization of the wave is elliptical rather than circular. Therefore the equations of motion have additional terms. Also, a non-longitudinal wave does not follow a given field line and its path in the magnetosphere must be calculated by using ray tracing. The results of the ray tracing must then be incorporated into the simulation in order to obtain wave and medium parameters such as wave number, wave normal and gyrofrequency along the ray path. In addition to first order cyclotron resonance as described by (2.30) a non-longitudinal wave resonates with the particles in the Landau, or longitudinal resonance mode when $v_p \approx v_{\parallel} \cos \theta$. Since there is a non-zero parallel component of the electric field, energy exchange between the wave and the particle can occur in this case. Furthermore there is space charge bunching, again as a result of the parallel electric field component. A given non-longitudinal wave will resonate with the particles in both the cyclotron and Landau mode, as well as all other harmonic resonances, $\omega + kv_{\parallel} = m\omega_H$, $m = 0, \pm 1, \pm 2$, etc. Fortunately, in the magnetosphere the cyclotron and Landau resonance interactions are fully separable, since the former occurs when the wave and the particles travel in opposite directions whereas the latter occurs when they travel in the same direction.

The simulation of the cyclotron resonance interaction with quasi-longitudinal waves, i.e., waves which propagate more or less along the magnetic field line but with $\theta < 30^\circ$, can be simulated with some modification to our computer program. In this case the wave path is defined and the major changes occur only in the equations of motion. The simulation of the Landau resonance interaction between a quasi-

Longitudinal wave and the particles requires little modification in the program. The adiabatic dynamics of particles, the manipulation of the distribution function and the computation of the medium parameters need not be changed. However one must use a different set equations of motions.

iii) Variation of the wave frequency: Our present program uses monochromatic pulses as the wave function. Most of the ground transmitter signals, although not all, and the signals induced by large scale power grids are in this form [Helliwell and Katsufakis, 1974; Helliwell et al., 1975]. However many interesting wave particle or wave-particle-wave interaction phenomena seen in VLF data involve one or more waves at different constant frequencies or one or more waves with varying frequency. To study these phenomena quantitatively it is necessary to modify the program to cover the more general case of multi-component waves with varying frequency. The required changes in the program lie in the computation of a wave structure and appear to be straightforward in nature. One other important application of a program using a variable frequency wave would be to determine the optimum wave frequency variation which would extend the resonance time and optimize the precipitated flux. To first order, for a given wave intensity the wave frequency must vary such that Eq. (2.30) is satisfied over a longer distance along the field line. However the wave induced changes in particle parallel velocity complicate this picture. If B_w is large enough (2.30) can be satisfied over a long path for even a fixed frequency wave.

iv) Feedback: The most general solution to the problem of gyro-resonant wave-particle interaction in the magnetosphere should include

the amplification or growth of the wave, i.e. the energy transfer from the particles to the wave.

In our studies up to this point we have assumed a wave structure and computed the particle mechanics. This is not a very limiting assumption since one could use a spatially growing wave as the wave structure and hence indirectly account for the effect of the particles on the wave. The spatial growth pattern could be calculated in a separate analysis or deduced from data.

The full self-consistent solution however would be a computation which modifies the wave in accordance with the fields radiated by the currents produced by the phase bunched particles [Helliwell and Crystal, 1973] while they are scattered by the wave.

It should be noted that in our present program the full phase motion of all particles, which in effect gives the phase bunched currents, is already computed. Therefore it is conceivable that the present program can be used to find the new fields radiated by the particles. However, this must be done at each step of the interaction on a space-time frame and the computation becomes complicated. Although we believe that this feedback computation could be done, with some limitations, we think that it requires important modifications of the present program.

APPENDIX A: SHAPE OF $\Delta\alpha_{eq}$ vs. ϕ_0 CURVES

In this appendix we will present a semi-quantitative analysis aimed at understanding the shapes of the $\Delta\alpha_{eq}$ vs. ϕ_0 curves discussed in Chapter 4. We first show that for linear theory the total scattering is proportional to $\sin\phi_0$.

By definition, linear theory assumes that the particle scattering can be computed using the unperturbed phase motion of the particle. This is explained in section 2.F where we discuss the linear theory and have derived expressions for Δv_{\parallel} and Δv_{\perp} . Note that for the single equatorially resonant sheet which we have considered in Figs. 4.2 through 4.9 all initial phases have the same $v_{\parallel 0}$ and α_0 , and therefore the variation $\phi = f(t)$ as given by (2.51) is the same for all initial phases. Rewriting the expression (2.53a) for Δv_{\parallel} we have

$$\Delta v_{\parallel} \approx \left(\frac{eB_w}{m}\right) v_{\perp} \int_0^T \sin(F(t) + \phi_0) dt \quad (A.1)$$

Using trigonometric identities, (A.1) can be written as

$$\Delta v_{\parallel} = \frac{eB_w}{m} v_{\perp} \left[\int_0^T \sin\phi_0 \cos[F(t)] dt + \int_0^T \cos\phi_0 \sin[F(t)] dt \right] \quad (A.2)$$

Since $F(t) = \int_0^t f(t') dt'$ is independent of ϕ_0 , so are $\int_0^T \cos[F(t)] dt$ and $\int_0^T \sin[F(t)] dt$. Let

$$K_1 = \int_0^T \cos[F(t)] dt, \quad K_2 = \int_0^T \sin[F(t)] dt \quad (A.3)$$

then

$$\Delta v_{\parallel} = \frac{eB_w}{m} v_{\perp} [K_1 \sin \phi_0 + K_2 \cos \phi_0] = \frac{eB_w}{m} v_{\perp} \sqrt{K_1^2 + K_2^2} \sin(\phi_0 + \beta) \quad (A.4)$$

where $\beta = \tan^{-1} \frac{K_2}{K_1}$.

Similarly by manipulating Eq. (2.53b) we obtain:

$$\Delta v_{\perp} = -\frac{eB_w}{m} (v_{\parallel} + \frac{\omega}{k}) \sqrt{K_1^2 + K_2^2} \sin(\phi_0 + \beta) \quad (A.5)$$

Now since $\alpha = \tan^{-1} (\frac{v_{\perp}}{v_{\parallel}})$ we have:

$$\Delta \alpha = \cos^2 \alpha \left(\frac{1}{v_{\parallel}} - \frac{v_{\perp}}{v_{\parallel}^2} \frac{\Delta v_{\parallel}}{\Delta v_{\perp}} \right) \Delta v_{\perp} \quad (A.6)$$

By substituting (A.4) and (A.5) into (A.6) we obtain

$$\Delta \alpha = C(v_{\parallel 0}, \alpha_0) \sin(\phi_0 + \beta) \quad (A.7)$$

where $C(v_{\parallel 0}, \alpha_0)$ is independent of ϕ_0 and β . Equation (A.7) shows that $\Delta \alpha_{eq}$ vs. ϕ_0 curves obtained using linear theory should have a sinusoidal shape as indicated by Fig. 4.5. For $\rho < 1$, the full solution of Eqs. (2.36) is closely approximated by the linear theory, hence the $\Delta \alpha_{eq}$ vs. ϕ_0 curves are almost sinusoidal.

For $\rho > 1$, the linear approximation is no longer valid. In other words, the phase variation for different ϕ_0 is not the same, since \dot{v}_{\parallel} is different for different ϕ_0 . Moreover, the interaction time T is also a function of ϕ_0 . Therefore Eq. (A.2) cannot be further simplified and the total scattering Δv_{\parallel} for each ϕ_0 must be found by a

general solution of Eqs. (2.36).

Although it is hardly possible to do this analytically, the shape of the $\Delta\alpha_{eq}$ vs. ϕ_0 curves for the nonlinear case can be understood qualitatively by referring to the discussion in connection with Figs. 4.2 and 4.3. The basic idea is that for $\rho \gg 1$, particles with initial phases around $\phi_0 \approx 0$ are trapped in the wave. For the trapped particles $v_{\parallel} \approx v_R$ and $\dot{v}_{\parallel} \approx \dot{v}_R$ since $\dot{v}_R > 0$ for particles moving southward from the equator, $\dot{v}_{\parallel} > 0$ and from Eqs. (4a,b) $\dot{v}_{\perp} < 0$. Thus $\Delta\alpha_{eq} < 0$ for these trapped particles.

1871
The first of the year was a very
cold one, and the weather was
very disagreeable. The snow
was very deep, and the wind
was very strong. The people
were very much distressed,
and the government was very
kind to them. The people
were very much distressed,
and the government was very
kind to them.

APPENDIX B: LOSS CONE REFLECTION EFFECT

This appendix briefly describes what we term the "loss cone reflection effect" to which we have attributed some aspects of Figs. 4.4, 4.14 and 4.15. This effect becomes prominent for very low pitch angles and/or high wave intensities. It is caused by that term in Eq. (2.36c) which is proportional to $B_w \frac{\cos \phi}{v_\perp}$.

In all our computer calculations we have kept this term in the equations of motion. Therefore its effects are seen whenever v_\perp is low enough, i.e. the pitch angle is below a few degrees. In our qualitative discussions however, especially those in connection with the 'pendulum' equation (2.45) we have ignored this term. In the following we reexamine the phase variation to clearly see the effect of this term.

Assume that $B_w \frac{\cos \phi}{v_\perp}$ is so large that $\dot{\phi}$ is approximately given by

$$\dot{\phi} \approx - \left(\frac{eB_w}{m} \right) \left(v_\parallel + \frac{\omega}{k} \right) \frac{\cos \phi}{v_\perp} \quad (\text{B.1})$$

Rewriting Eq. (2.36b) without the adiabatic term we have

$$\dot{v}_\perp = - \left(\frac{eB_w}{m} \right) \left(v_\parallel + \frac{\omega}{k} \right) \sin \phi \quad (\text{B.2})$$

Dividing Eq. (B.2) by (B.1) we obtain

$$\frac{dv_\perp}{v_\perp} = \frac{\sin \phi d\phi}{\cos \phi} \quad (\text{B.3})$$

or, integrating,

$$\ln(v_\perp) = -\ln(\cos \phi) + \text{constant} \quad (\text{B.4})$$

or

$$v_{\perp} \cos \phi \approx \text{constant} \quad (\text{B.5})$$

Eq. (B.5) shows that for the cases when ϕ can be approximated by (B.1), $v_{\perp} \cos \phi$ is a constant of the motion. This constant of motion is a reduced form of the general one that gives the conservation of angular momentum [Bell, 1964].

Note that during the course of any interaction, especially in the trapped mode as described in section 4.C, in which the pitch angle (therefore v_{\perp}) continuously decreases there will always come a time where v_{\perp} is so low that (B.1) would be true. Assume this occurs at time t_a when $v_{\perp} \approx v_{\perp a}$ and $\phi \approx \phi_a$. Then we have

$$v_{\perp} \cos \phi \approx v_{\perp a} \cos \phi_a \quad (\text{B.6})$$

since $|\cos \phi| < 1$, it is apparent that v_{\perp} is bounded on the lower end so that it cannot decrease below a value $v_{\perp a} \cos \phi_a$. Therefore the effect of the $B \frac{\cos \phi}{v_{\perp}}$ term in Eq. (2.36c) is to effectively prevent the pitch angle from reaching zero. Since ϕ continuously changes ($\dot{\phi}(t) \neq 0$) v_{\perp} has to change also and since it is bounded on the lower end, it increases. This can be seen by considering a worst case.

Assume at some $t > t_a$, $\phi \approx 0$. In that case $v_{\perp} = v_{\perp a} \cos \phi_a$ and $\dot{v}_{\perp} = 0$. But $\dot{\phi}$ is a maximum. Therefore ϕ goes negative and v_{\perp} has to increase through (B.2 and B.5). Note that once \dot{v}_{\perp} becomes positive and v_{\perp} starts to increase this trend cannot be reversed. As ϕ approaches $-\pi/2$, v_{\perp} increases through (B.6) and eventually the approximation (B.1) breaks down and the first term in Eq. (2.36c) takes over.

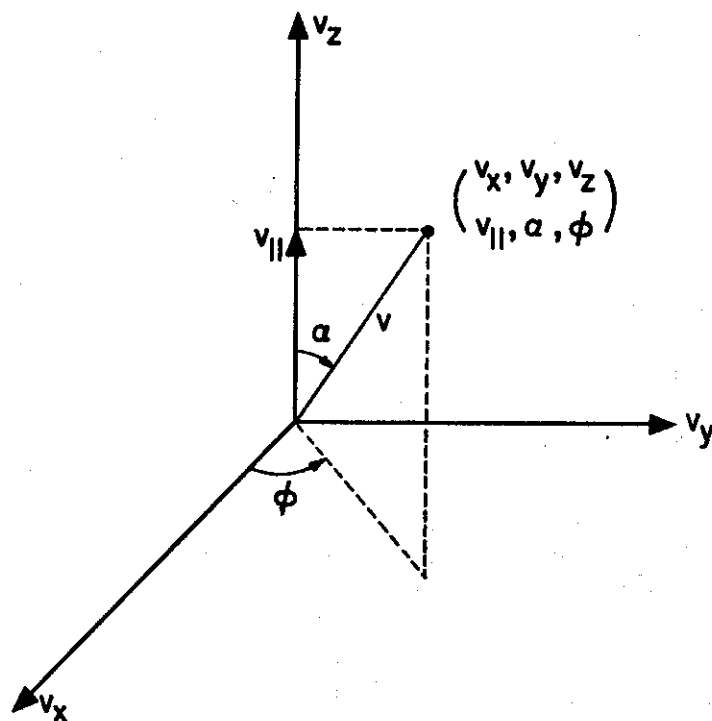
The conclusion of the above analysis is the following: if at any time during the interaction v_{\perp} approaches zero closely enough so that (B.1) becomes valid, it will be 'reflected' back and increase to a value such that (B.1) is not valid. This reflection is termed the 'loss cone reflection effect'. An example of this effect is seen in the sharp reflection of pitch angle at the second minimum of the $\Delta\alpha_{eq}(t)$ for $\phi_0 = -\pi/3$ particle the trajectory of which is given in Fig. 4.3. At that point $\Delta\alpha_{eq} \approx \alpha_{eq_0}$.

The slow decrease of $\Delta\alpha_{eq}$ for the $\alpha_{eq_0} = 10^\circ$ and 30° particles for $B_w \geq 50$ mγ and 100 mγ are also due partially to this effect. However these cases are more difficult to describe and will not be detailed here.

Note that in addition to the loss cone reflection effect the $B_w \frac{\cos\phi}{v_{\perp}}$ term also changes the mode of trapping when B_w is sufficiently large. This occurs when $|\omega_H - \omega - kv_{\parallel}| \approx |(\frac{eB}{m})(v_{\parallel} + \frac{\omega}{k}) \frac{\cos\phi}{v_{\perp}}|$ so that neither (B.1) nor (2.38) is not valid. In that case one has to use the complete equation (2.36c) for $\dot{\phi}$. The interaction is no longer analogous to a simple pendulum with an applied torque.

APPENDIX C: JACOBIAN FOR $f(v_{||}, \alpha, \phi)$

In this appendix we demonstrate that the velocity space volume element in terms of $v_{||}$ and α is $v_{||}^2 \frac{\sin \alpha}{\cos^3 \alpha} d\alpha dv_{||} d\phi$ as used in Chapter 5. The coordinate system is shown below.



We have

$$v_x = v \sin \alpha \cos \phi = v_{||} \frac{\sin \alpha}{\cos \alpha} \cos \phi$$

$$v_y = v \sin \alpha \sin \phi = v_{||} \frac{\sin \alpha}{\cos \alpha} \sin \phi$$

$$v_z = v \cos \alpha = v_{||}$$

The Jacobian is then given by,

$$J = \frac{\partial(v_x, v_y, v_z)}{\partial(v_{\parallel}, \alpha, \phi)} = \begin{vmatrix} \frac{\partial v_x}{\partial v_{\parallel}} & \frac{\partial v_x}{\partial \alpha} & \frac{\partial v_x}{\partial \phi} \\ \frac{\partial v_y}{\partial v_{\parallel}} & \frac{\partial v_y}{\partial \alpha} & \frac{\partial v_y}{\partial \phi} \\ \frac{\partial v_z}{\partial v_{\parallel}} & \frac{\partial v_z}{\partial \alpha} & \frac{\partial v_z}{\partial \phi} \end{vmatrix}$$

$$= \begin{vmatrix} \frac{\sin \alpha}{\cos \alpha} \cos \phi & v_{\parallel} \frac{1}{\cos^2 \alpha} \cos \phi & -v_{\parallel} \frac{\sin \alpha}{\cos \alpha} \sin \phi \\ \frac{\sin \alpha}{\cos \alpha} \sin \phi & v_{\parallel} \frac{1}{\cos^2 \alpha} \sin \phi & v_{\parallel} \frac{\sin \alpha}{\cos \alpha} \cos \phi \\ 1 & 0 & 0 \end{vmatrix}$$

$$= - (v_{\parallel} \frac{1}{\cos^2 \alpha} \cos \phi) (-v_{\parallel} \frac{\sin \alpha}{\cos \alpha} \cos \phi) + (-v_{\parallel} \frac{\sin \alpha}{\cos \alpha} \sin \phi) (-v_{\parallel} \frac{1}{\cos^2 \alpha} \sin \phi)$$

$$= v_{\parallel}^2 \frac{\sin \alpha}{\cos^3 \alpha} [\cos^2 \phi + \sin^2 \phi] = v_{\parallel}^2 \frac{\sin \alpha}{\cos^3 \alpha}$$

Hence the volume element in the $v_{\parallel}, \alpha, \phi$ coordinate system is

$$dV = v_{\parallel}^2 \frac{\sin \alpha}{\cos^3 \alpha} d\alpha dv_{\parallel} d\phi$$

APPENDIX D: THE COMPUTER SIMULATION

This program is a simplified version of the one used for the computations in this report.

The program simulates the cyclotron resonance interaction of energetic electrons with a fixed frequency wave of constant amplitude in the Magnetosphere.

In the following we give a listing of the program together with brief descriptions of various sections.

INPUT PARAMETERS

F = wave frequency (degrees)

YL = L value of the field line

PHI1D = Latitude at 1000 km altitude (degrees)

YNEQ = Equatorial cold plasma density (el/cc)

YLAMAX = Latitude range (see Chapter III) (Degrees)

M = Number of mesh points between - YLAMAX and Equator.

N = Number of electrons per sheet

BWEQ = Wave intensity (in milligammas)

PHIWH = Initial phase of the first electron in the sheet (degrees)

ALPHMN, HALPHA, ALPHMX determine the initial equatorial pitch angle for which the calculation is to be made.

Initial pitch angles varying from ALPHMN to ALPHMX in steps of HALPHA are simulated. All three quantities are in degrees.

MSTEP = Number of steps between each spatial step for which the medium is stored.

DUR = The integration is stopped when the particle is away from resonance by an amount $100 \times \text{DUR}$ percent

PHSTOP = The interaction is not stopped until DPHI becomes larger than PHSTOP (degrees).

STRT = The particle is introduced to the wave at a location where it is away from resonance by an $(1 - \text{STRT}) \times 100$ percent.

ALPHAV = Average pitch angle of the particles to be simulated. This is useful for the setting up of the parallel velocity mesh of the distribution function (Degrees).

RSTSZ = The parallel velocity mesh of the distribution function is set up in such a way that the mesh points are separated in the corresponding resonance latitude by RSTSZ (Degrees).

NPITCH = Pitch angle mesh size for the distribution.

NVB = Number of mesh points in parallel velocity.

NPB = Number of mesh points in pitch angle.

DSTPLT = If DSTPLT is less than 1.0 the full distribution computations not made.

PLT = If PLT is less than 1.0 the single particle trajectories are not plotted.

RANGE = Pitch angle range (degrees) for the plot of single particle trajectory.

RANGPH = Phase range (degrees) for the same plot.

IGRSTP = Number of integration steps between each plotted point.

YLF, YTT, YLST determine the initial equatorial parallel velocity for which the calculation is to be made. Parallel velocities are determined according to latitude of resonance. Particles with equatorial parallel velocities such that they will resonate with the wave at latitudes YLF to YTT in steps of YLST are simulated. All three quantities are in degrees.

```

1    DIMENSION Z(4000),WH(4000),VPA(4000),
2    2ALPH(900),PHASE(900),VPERP(900),VPARA(900),TIM(900),HRA(10),
3    1YLT(900),EQALPH(900),
4    3HRZPH(10),VDIFF(900),ALAT(201),LFEQ(100)
5    DIMENSION FFEQ(80,40),VILEQ(401),PTCHEQ(91),VIIBEQ(401)
6    LOGICAL GR(79),BLANK,HORBAR,VERBAR,YMULT,PLUS,GSH(119)
7    DATA BLANK/1H/,HORBAR/1H-/,VERBAR/1H/,YMULT/1H/,PLUS/1H+/
8    1,GR/79*1H/,GSH/119*1H/
9    PI=3.1415926535
10   PIR=180.0/PI
11   PI2=2.0*PI
12   BIR2PI=0.5/PI
13   FHEQ=873600.0
14   R0=6370
15   a1=7370
16   H1=227.185
17   H2=908.061
18   H3=3606.121
19   READ(5,600) F,YL,PHI1D,YNEQ,YLAMAX,M
20   800 FORMAT(5F10.2,I10)
21   WRITE(6,800) F,YL,PHI1D,YNEQ,YLAMAX,M
22   READ(5,900) N,BWEQ,PHIWH,ALPHMN,HALPHA,ALPHMX,YLF,YTT,YLSI
23   900 FORMAT(I3,F7.2,F10.5)
24   WRITE(6,900) N,BWEQ,PHIWH,ALPHMN,HALPHA,ALPHMX,YLF,YTT,YLSI
25   READ(5,801) MSTEP,DUR,PHSTOP,STRT,ALPHAV,RSTS2,NVB,HPITCH,NPB
26   801 FORMAT(I3,F7.3,4F10.5,I10,F10.5,I10)
27   WRITE(6,801) MSTEP,DUR,PHSTOP,STRT,ALPHAV,RSTS2,NVB,HPITCH,NPB
28   READ(5,802) DSTPLT,PLT,RANGE,RANGPH,IGRSTP
29   802 FORMAT(4F10.2,I10)
30   WRITE(6,802) DSTPLT,PLT,RANGE,RANGPH,IGRSTP
31   JBF=ALPHMN/HPITCH
32   JBT=ALPHMX/HPITCH
33   JBST=(ALPHMX-ALPHMN)/HALPHA+1
34   PHSTOP=PHSTOP/PIR
35   PHSTN=-PHSTOP
36   HPITCH=HPITCH/PIR
37   ALPHAV=ALPHAV/PIR
38   YMSTEP=MSTEP
39   YN=M
40   W=F*PI2
41   HE=RANGE/4.0
42   SE=80.0/(2.0*RANGE)
43   HAPH=AANGPH/4.0
44   SFPH=80.0/(2.0*AANGPH)
45   DURM1=1.0-DUR
46   DUAP1=1.0+DUR
47   YN=N
48   BW=BWEQ*0.175927
49   REQ=YL*R0

```

C

C THE COMPUTATION OF THE MEDIUM

C

```

46   C1=1.0/YL
47   C2=SQR(C1)
48   PHI0R=ARCCOS(C2)
49   C3=(0.5)*(a0/(1.73205*C1))
50   C4=FHEQ*C1*C1*C1*6.2831852
51   C5=5*IN(PHI0R)
52   C6=SQR(3.0*C5*C5+1.0)
53   S0=C3*(ALOG(1.73205*C5+C6)+1.73205*C5*C6)
54   PHI1R=PI*PHI1D/180.0
55   R1SQ=a1*R1
56   C7=COS(PHI1R)
57   C8=R1SQ*C7*C7

```

```

58      ZEQ=R1-R1SQ/R-3.6094E-10*(R-REQ-CE)
59      C9=YNEQ/SQRT(0.9*EXP(-ZEQ/H1)+0.02*EXP(-ZEQ/H2)+0.08*EXP(-ZEQ/H3)
1.)
60      C10=RC/C1
61      YLARAD=YLAMAX/PIR
62      H=-YLARAD/YM
63      KL=M+1
64      DO 22 I=1, KL
65      YI=I-1
66      PHIR=YLARAD+YI*H
67      IF(I.EQ. KL) PHIR=0.0
68      C11=SIN(-PHIR)
69      C12=1.73205*C11
70      C13=SQRT(3.0*C11*C11+1.0)
71      S=C3*(ALOG(C12+C13)+C12*C13)
72      C14=COS(PHIR)
73      C15=C14*C14
74      C16=C15*C15*C15
75      WH(I)=(C4/C16)*C13
76      Z(I)=(S0-S)*1.0E+03
77      R=C10*C15
78      ZE=R1-R1SQ/R-3.6094E-10*(R*R*C15-CE)
79      YN=C9*SQRT(0.9*EXP(-ZE/H1)+0.02*EXP(-ZE/H2)+0.08*EXP(-ZE/H3))
80      C17=WH(I)-Y
81      YK=0.33357E-05*SQRT(W/C17)*1.0E-03*SQRT(YN*0.31833E+10)
82      VPAR(I)=C17/YK
83      IF(I.EQ. 1) GO TO 22
84      20 IF(PHIR.EQ.0.0) GO TO 21
85      22 CONTINUE
86      21 KL=I
87      NT=2*KL-1
88      EMAX=2.84217E-15*VPAR(1)*VPAR(1)
89      IEQ=1+(NT-1)/2
C
C END OF COMPUTATION OF THE MEDIUM.
C THE OUTPUT OF THIS SECTION IS THE
C TRIPLET Z , WH(Z) AND VPAR(Z)=LOCAL RESONANCE VELOCITY
C
90      IBF=0
91      IBT=0
92      MVII=RSTSZ/(PIR*H)
C
C SETTING UP THE PITCH ANGLE AND PARALLEL VELOCITY
C LABELS OF THE MESHES OF THE DISTRIBUTION FUNCTION.
C NVB MESH POINTS WITH PARALLEL VELOCITIES VIIEQ(.)
C AND NEB MESH POINTS WITH PITCH ANGLES PTCHQ(.).
C
93      DO 621 KSET=1,35
94      YKSET=KSET-1
95      621 PTCHQ(KSET)=YKSET*HPITCH*PIR
96      DO 620 KSET=2,15
97      YKSET=KSET
98      VIIEQ(KSET)=VPAR(IEQ)*(1.0-0.001*(-YKSET+16))
99      IF(KSET.EQ.2) GO TO 620
100     VIIEQ(KSET)=(VIIEQ(KSET)+VIIEQ(KSET-1))/2.0
101     620 CONTINUE
102     SNEQEQ=SIN(ALPHAV)*SIN(ALPHAV)
103     DO 622 KSET=16,NVB
104     ILOC=IEQ+(KSET-16)*MVII
105     ILPA=-ILOC+NT+1
106     IF(ILOC.GT.NT) GO TO 761
107     YI=ILPA-1
108     YLATI=YLAMAX+YI*H*PIR
109     IF(ILPA.EQ. IEQ) YLATI=0.0

```

```

110      ALAT(KSET) = -YLATI
111      SWSQLC = WH(ILPR) * SNSQEQ / WH(IEQ)
112      VIIEQ(KSET) = SQRT((1.0 - SWSQLC) * VPAR(ILPR) * VPAR(ILPR) / (1.0 - SWSQLC))
113      VIIEQ(KSET) = (VIIEQ(KSET) + VIIEQ(KSET-1)) / 2.0
114      622 CONTINUE
115      761 VIIEQ(1) = 0.5 * VPAR(IEQ)
116      VIIEQ(1) = 0.5 * VPAR(IEQ)
117      NVB = KSET - 1
118      NVBP1 = NVB + 1
119      VIIEQ(2) = 2.0 * VIIEQ(2) - VIIEQ(3)
120      VIIEQ(NVBP1) = VPAR(1) * 1.5
121      VIIEQ(NVB) = VPAR(1)
122      KSETM1 = KSET - 2
123      DO 760 KS = 16, KSETM1
124      IF(YLF.GE.ALAT(KS).AND.YLF.LT.ALAT(KS+1)) IBF=KS
125      C760=YLF-ALAT(KS)
126      C761=ALAT(KS+1)-YLF
127      IF(IBF.EQ.KS.AND.C760.GT.C761) IBF=KS+1
128      IF(YTT.GE.ALAT(KS).AND.YTT.LT.ALAT(KS+1)) IBT=KS
129      C762=YTT-ALAT(KS)
130      C763=ALAT(KS+1)-YTT
131      IF(IBT.EQ.KS.AND.C762.GT.C763) IBT=KS+1
132      760 CONTINUE
133      IF(IBT.EQ.0) IBT=KS-1
134      IF(IBF.EQ.0) IBF=KS-1
135      STPSZ=YLIST/(PIR*H)
136      IBST=STPSZ/MVII

```

C
C INITIALIZATION OF THE DISTRIBUTION FUNCTION.
C IN THIS CASE FFEQ= N ABOVE THE LOSS CONE AND
C IS ZERO BELOW THE LOSS CONE.

```

137      IF(DSTPLT.LT.1.0) GO TO 614
138      DO 502 IBEQ=2, NVB
139      DO 503 JBEQ=1, 11
140      503 FFEQ(IBEQ, JBEQ) = 0
141      DO 502 JBEQ=12, 39
142      502 FFEQ(IBEQ, JBEQ) = N
143      DO 505 JBEQ=1, 39
144      FFEQ(1, JBEQ) = 0
145      505 FFEQ(NVB, JBEQ) = 0
146      614 CONTINUE
C
147      DO 701 JBEQ=JBF, JBT, JBST
148      ALPHEQ=HPITCH*(2.0*JBEQ-1.0)*0.5
149      TNAL=TAN(ALPHEQ)
150      IOLD=IEQ
151      DO 702 IBEQ=IBF, IBT, IBST
152      VPAREQ=VIIEQ(IBEQ)
153      VPEEQ=VPAREQ*TNAL
154      VPEQSQ=VPEEQ*VPEEQ
155      VPRESQ=VPAREQ*VPAREQ
156      ENERGY=VPRESQ+VPEQSQ
157      DO 401 IRF=IOLD, NT
158      IRFPR=-IRF+NT+1
159      VPESQ=WH(IRFPR)*VPEQSQ/WH(IEQ)
160      VPSQ=ENERGY-VPESQ
161      VPALEL=SQRT(VPSQ)
162      IF(VPALEL.LE.(VPAR(IRFPR)*STRT)) GO TO 402
163      401 CONTINUE
164      402 IOLD=IRF
165      IF(IRF.EQ.(NT+1)) IRF=NT
166      I=IRF
167      VPA0=VPALEL

```



```

168      VPEQ=SQRT(VPESQ)
169      IPRIME=I
170      IF (I.GT. IEQ) IPRIME=-I+NT+1
171      IWHAT=I
172      DO 52 J=1,N
173      L1POLD=0
174      ITO=NT
175      IF (DSTPLT.LT. 1.0) GO TO 789
176      CSA=COS (ALPHEQ)
177      OLBNFC=VPAHEQ*VPAHEQ*SIN (ALPHEQ) /CSA*CSA*CSA
178      FFEQ (IBEQ,JBEQ) = FFEQ (IBEQ,JBEQ) -1.0
179      789 CONTINUE

C
C PLOTTING ROUTINE
C
180      IF (PLT.LT. 1.0) GO TO 902
181      VDIF=(VPA0-VPA (IPRIME)) /VPA (IPRIME)
182      DO 250 LHA=1,7
183      YLHA=LHA
184      HRZ (LHA) =HR*YLHA-RANGE
185      HRZPH (LHA) = (HRPH*YLHA) -RANGPH
186      NHA=LHA*10+1
187      250 GR (NHA) =VERBAR
188      WRITE (6,249) BWEQ,VDIF
189      249 FORMAT (1H1,'BWAIVE AT EQUATOR =',F8.2,' MILLIGAMMAS',',', VOFF =',
1E10.5/)
190      WRITE (6,251) (HRZPH (LHA),LHA=1,7),GR
191      251 FORMAT (39X,'+++++ PHASE (ANGLE BETWEEN -BWAIVE & VPERP) (DEGREES)'
1/44X,7(F8.2,2X)/39X,79A1/)
192      WRITE (6,252) (HRZ (LHA),LHA=1,7),GR
193      252 FORMAT (39X,'$$$$$ CHANGE IN EQUATORIAL PITCH ANGLE (DEGREES) '/'
1PITCH OFFLES. PHASE LATITUDE TIME',8X,7(F6.2,4X)/1X,' (DEG) '
2 X ) (DEG) (DEG) (MSEC)',79A1)
194      DO 254 LHA=1,79
195      254 GR (LHA) =HORBAR
196      WRITE (6,255) GR
197      255 FORMAT (39X,79A1)
198      DO 256 LHA=1,79
199      256 GR (LHA) =BLANK
200      GR (41) =VERBAR
201      902 CONTINUE

C
202      VPA=VPA0
203      VPE=VPE0
204      T=0.0
205      YJ=J-1
206      PHI=PHIWH/PIR+YJ*PI2/YN
207      DVPA=0.0
208      L1OLD=1
209      405 IM1=I-1

C
C INTEGRATION OF EQUATIONS OF MOTION. A DIRECT SIMULATION
C OF THE EQUATIONS IS USED.
C
210      DO 53 L1=L1OLD,IM1
211      LPR=I-L1+1
212      L=LPR
213      LM1=LPR-1
214      IF (LPR.GT. IEQ) L=-LPR+NT+1
215      IF (LPR.GT. IEQ) LM1=L+1
216      IF (PLT.LT. 1.0) GO TO 903
217      L1PLT=(L1-1)/IGRSTF+1
218      IF (L1PLT.EQ. L1POLD) GO TO 899
219      ALPH (L1PLT) =ATAN (VPE/VPA)

```

```

220      SNAL=SIN(ALPH(L1PLT))
221      EQALPH(L1PLT)=ARCSIN(SQRT((WH(IEQ)/WH(L))*SNAL*SNAL))-ALPHEQ
222      PHASE(L1PLT)=PIR*PHI
223      YI=L-1
224      YLAFI=YLADAX+YI*H*PIR
225      IF(L.EQ.IEQ) YLAFI=0.0
226      YLT(L1PLT)=YLAFI
227      IF(LPR.GT.IEQ) YLT(L1PLT)=-YLAFI
228      VPEHF(L1PLT)=VPE
229      VPAKA(L1PLT)=VPA*1.0E-03
230      TIM(L1PLT)=T*1000.0
231      VDIF(L1PLT)=VDIF*100.0/VPAR(L)
232      L1POLD=L1PLT
233      899 CONTINUE
234      903 CONTINUE
235      CWH=(WH(LM1)-WH(L))/YMSTEP
236      DO 55 MD=1,MSTEP
237      VPYN=VPA(L)+((VPA(LM1)-VPA(L))/YMSTEP)*(MD-1)
238      WHNW=WH(L)+CWH*(MD-1)
239      WHNWM1=WH(L)+CWH*MD
240      DZ=(Z(L)-Z(LM1))/YMSTEP
241      IF(LPR.GT.IEQ) DZ=-DZ
242      SNPHI=SIN(PHI)
243      CSPHI=COS(PHI)
244      YKNA=(WHNW-W)/VPYN
245      C36=1.0/VPA
246      DT=DZ*C36
247      C30=VPA+W/YKNA
248      C34=VPE*0.5*(WHNW-WHNWM1)*C36/WHNW
249      C35=BW*SNPHI*DT
250      DVPE=-C30*C35-C34*VPA
251      DVPA=(C35+C34)*VPE
252      VDIF=VPA-VPYN
253      DPHI=(-VDIF*YKNA)
254      DPHI=DPHI-BW*C30*CSPHI/VPE
255      57 DPHI=DPHI*DT
256      58 CONTINUE
257      T=T+DT
258      VPE=VPE+DVPE
259      VPA=VPA+DVPA
260      PHI=PHI+DPHI
261      55 CONTINUE
262      IF(DPHI.LT.PHSTOP.AND.DPHI.GT.PHSTN) GO TO 53
263      VWHT=VPA
264      IF(VWHT.LT.(DURM1*VPA(L))) GO TO 54
265      IF(VWHT.GT.(DURP1*VPA(L))) GO TO 54
266      53 CONTINUE
267      54 IF(LPR.LT.IEQ) GO TO 404
268      ITO=IEQ-(LPR-IEQ)
269      L1QLD=L1+1
270      GO TO 405
271      404 CONTINUE

```

C
C END OF INTEGRATION. THE OUTPUT OF THIS SECTION IS THE
C LOCAL VALUES VPE AND VPA (THE PERPENDICULAR AND PARALLEL
C VELOCITIES)
C
C
C
C CONVERSION BACK TO EQUATORIAL VALUES AND ADJUSTMENT OF THE
C DISTRIBUTION FUNCTION.
C

```

272      VPESQ=VPE*VPE
273      CUTEAG=VPESQ+VPA*VPA
274      VPEQSQ=WH(IEQ)*VPESQ/WH(L)

```

```

275      VPRESQ=OUTLNG-VPEQSQ
276      VPARNW=SQRT (VPRESQ)
277      VPEEQ=SQRT (VPEQSQ)
278      ALPHNW=ATAN (VPEEQ/VPARNW)
279      DO 623 ISOAT=1,NVB
280      IE (VPARNW.LE.VIIBEQ (ISOAT+1) .AND.VPARNW.GT.VIIBEQ (ISOAT)) GO TO 624
281 623 CONTINUE
282 624 IBNEW=ISOAT
283      JBNBW=ALPHNW/HPITCH+1
284      IF (JBNBW.LT.1) JBNBW=1
285      IF (JBNBW.GT.NPB) JBNBW=NPB
286      IR (DSTPLT.LT.1.0) GO TO 790
287      CSNA=COS (ALPHNW)
288      YBNBFC=VPARNW*VPARNW*SIN (ALPHNW) /CSNA*CSNA*CSNA
289      FREQ (IBNEW,JBNBW)=FFEQ (IBNEW,JBNBW)+OLBNBFC/YBNBFC
290 790 CONTINUE

```

C

C

C

C

PLOTTING ROUTINE FOR THE SINGLE PARTICLE TRAJECTORIES.

```

291 905 IF (PLT.LT.1.0) GO TO 52
292      L1M1=L1-1
293      IHMMCH=(L1-1)/IGRSTP+1
294      DO 93 IA=1,IHMMCH
295      YANG=EQA LPH (IA)*PIR
296      ALPH (IA)=ALPH (IA)*PIR
297      NNP=(YANG+RANGE)*SF+1.0
298      NNPPH=(PHASE (IA)+RANGPH)*SPPH+1.0
299      IF (NNP.LT.1.OR.NNP.GT.79) GO TO 907
300      GR (NNP)=YHULT
301 907 IF (NNPPH.LT.1.OR.NNPPH.GT.79) GO TO 202
302      GR (NNPPH)=PLUS
303 202 WRITE (6,203) YANG,VDIFF (IA),PHASE (IA),YLT (IA),TIM (IA),GR,VPARA (IA),
304      1ALPH (IA)
305 203 FORMAT (F7.1,F8.2,F9.1,F8.2,F8.2,79A1,F7.0,F5.2)
306      IF (NNP.LT.1.OR.NNP.GT.79) GO TO 908
307      GR (NNP)=BLANK
308 908 IF (NNPPH.LT.1.OR.NNPPH.GT.79) GO TO 94
309      GR (NNPPH)=BLANK
310 94 GR (41)=VERBAH
311 93 CONTINUE
312 52 I=I+HAT
313 702 CONTINUE
314 701 CONTINUE

```

C

C

C

PRINTING OF THE DISTRIBUTION FUNCTION.

```

314      IF (DSTPLT.LT.1.0) GO TO 524
315      WRITE (6,604) (PTCHEQ (KU),KU=1,32,2)
316 604 FORMAT (1H1,'EQUATORIAL DISTRIBUTION FUNCTION',/ VPARALEL (KM/SEC)
317      1',50X,'PITCH ANGLE (DEG) '/7X,16F6.1/9X,32(' '))
318      DO 601 IBEQ=1,NVBP1
319      IF (IBEQ.EQ.NVBP1) GO TO 524
320      VIIACT=VII EQ (IBEQ)/1000.0
321      DO 605 JBEQ=1,33
322      IFEQ (JBEQ)=FFEQ (IBEQ,JBEQ)
323 605 FORMAT (1X,F8.0,'-- ',33 (I2,' '))
324      WRITE (6,603) VIIACT, (IFEQ (JBEQ),JBEQ=1,33)
325 601 CONTINUE
326 524 CONTINUE
327      STOP
328      END

```

SDATA
 5000.00 4.00 57.50 400.00 -10.00 2000
 1 10.00 90.00000 7.00000 0.50000 7.33000 0.00000 0.00000 1.00000
 1 0.050 3.50000 1.00000 8.00000 0.30000 33 0.50000 50
 1.00 1.00 10.00 500.00 12

B-AVE AT EQUATOR = 10.00 MILLIGAUSS , VOFF = -0.00000

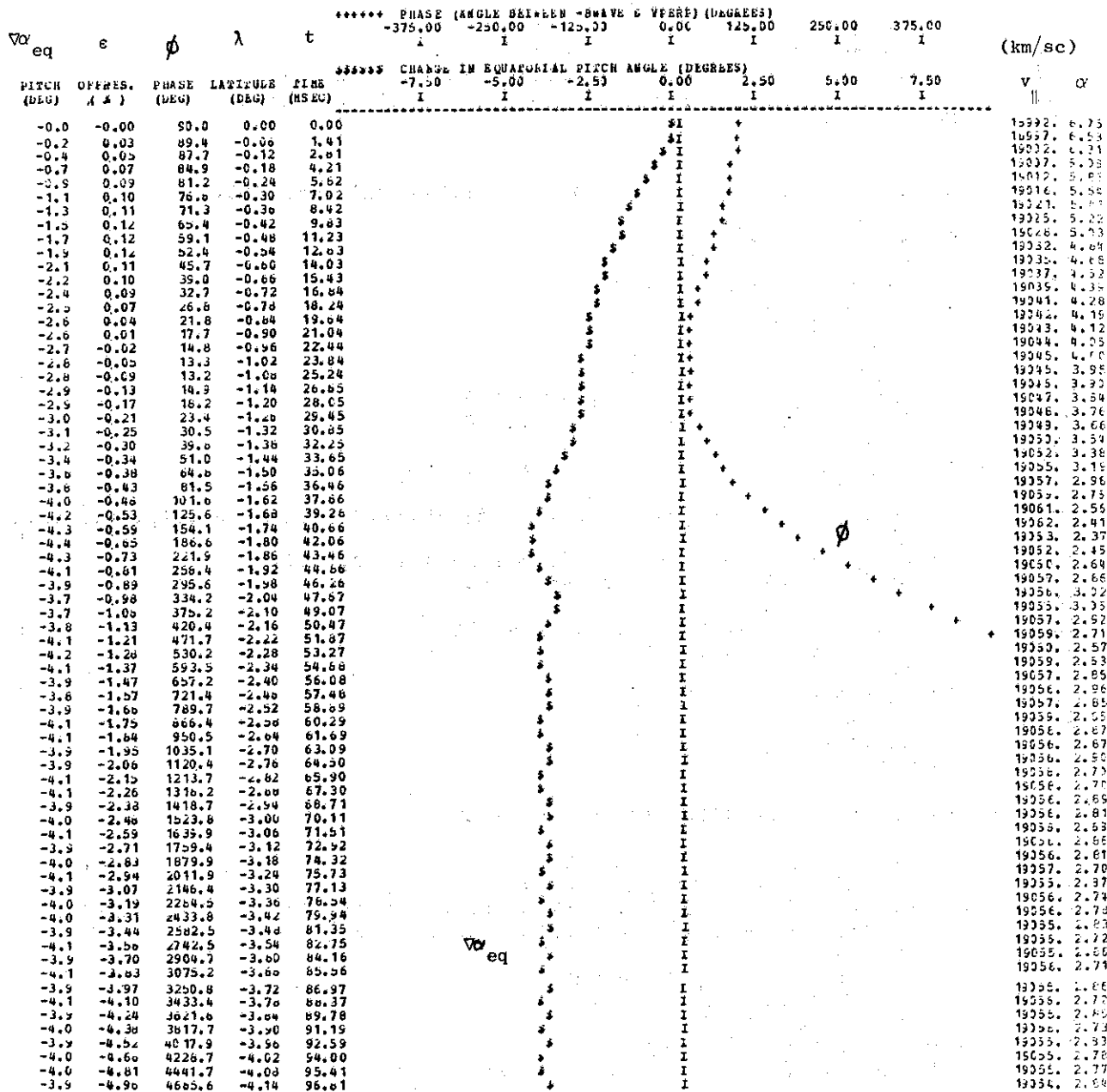


FIGURE D.1 Typical program output for the DATA input shown on the top.

($B_w = 10$ mV, $\alpha_{eq} = 6.75^\circ$, $\phi = 90^\circ$)

a) Particle trajectory.

EQUATORIAL DISTRIBUTION FUNCTION
V PARALLEL (K4/SEC)

	0.0	1.0	2.0	3.0	4.0	5.0	6.0	7.0	8.0	9.0	10.0	11.0	12.0	13.0	14.0	15.0
9496.---	0	0	0	0	0	0	0	0	0	0	0	0	0	0	0	0
18720.---	0	0	0	0	0	0	0	0	0	0	0	0	0	0	0	0
18745.---	0	0	0	0	0	0	0	0	0	0	0	0	0	0	0	0
18764.---	0	0	0	0	0	0	0	0	0	0	0	0	0	0	0	0
18783.---	0	0	0	0	0	0	0	0	0	0	0	0	0	0	0	0
18802.---	0	0	0	0	0	0	0	0	0	0	0	0	0	0	0	0
18821.---	0	0	0	0	0	0	0	0	0	0	0	0	0	0	0	0
18840.---	0	0	0	0	0	0	0	0	0	0	0	0	0	0	0	0
18859.---	0	0	0	0	0	0	0	0	0	0	0	0	0	0	0	0
18878.---	0	0	0	0	0	0	0	0	0	0	0	0	0	0	0	0
18897.---	0	0	0	0	0	0	0	0	0	0	0	0	0	0	0	0
18916.---	0	0	0	0	0	0	0	0	0	0	0	0	0	0	0	0
18935.---	0	0	0	0	0	0	0	0	0	0	0	0	0	0	0	0
18954.---	0	0	0	0	0	0	0	0	0	0	0	0	0	0	0	0
18973.---	0	0	0	0	0	0	0	0	0	0	0	0	0	0	0	0
18992.---	0	0	0	0	0	0	0	0	0	0	0	0	0	0	0	0
18997.---	0	0	0	0	0	0	0	0	0	0	0	0	0	0	0	0
19014.---	0	0	0	0	0	0	0	0	0	0	0	0	0	0	0	0
19041.---	0	0	0	0	0	0	0	0	0	0	0	0	0	0	0	0
19080.---	0	0	0	0	0	0	0	0	0	0	0	0	0	0	0	0
19129.---	0	0	0	0	0	0	0	0	0	0	0	0	0	0	0	0
19190.---	0	0	0	0	0	0	0	0	0	0	0	0	0	0	0	0
19202.---	0	0	0	0	0	0	0	0	0	0	0	0	0	0	0	0
19345.---	0	0	0	0	0	0	0	0	0	0	0	0	0	0	0	0
19440.---	0	0	0	0	0	0	0	0	0	0	0	0	0	0	0	0
19546.---	0	0	0	0	0	0	0	0	0	0	0	0	0	0	0	0
19604.---	0	0	0	0	0	0	0	0	0	0	0	0	0	0	0	0
19793.---	0	0	0	0	0	0	0	0	0	0	0	0	0	0	0	0
19935.---	0	0	0	0	0	0	0	0	0	0	0	0	0	0	0	0
20088.---	0	0	0	0	0	0	0	0	0	0	0	0	0	0	0	0
20254.---	0	0	0	0	0	0	0	0	0	0	0	0	0	0	0	0
20432.---	0	0	0	0	0	0	0	0	0	0	0	0	0	0	0	0
20623.---	0	0	0	0	0	0	0	0	0	0	0	0	0	0	0	0

(b) The full distribution. The distribution in this case is $f(v_{\parallel}, \alpha) = 1$ above the losscone and is zero below the losscone. The one particle for which the trajectory is shown in the previous page has moved from $\alpha_{eq_0} = 6.75^\circ$ and $v_{\parallel eq_0} = 18992$ km/sec to $\alpha_{eq_0} = 2.75^\circ$ and $v_{\parallel eq_0} = 19041$ km/sec. The value of the distribution at the new location is modified in accordance with the description given on page 121.

REFERENCES

- Akasofu, S. I. and S. Chapman, Solar Terrestrial Physics, Oxford at the Clarendon Press, 1972.
- Anderson, R. R., Wave particle interactions in the evening magnetosphere during geomagnetically disturbed periods, Ph. D. thesis, The University of Iowa, Iowa City, Iowa, 1976.
- Angerami, J. J., Whistler duct properties deduced from VLF observations made with the OGO-3 satellite near the magnetic equator, J. Geophys. Res., 75, 6115, 1970.
- Angerami, J. J. and J. O. Thomas, Studies of planetary atmospheres, 1, the distribution of electrons and ions in the earth's exosphere, J. Geophys. Res., 69, 4537, 1964.
- Appleton, E. V., URSI Reports, Washington, 1927.
- Ashour-Abdalla, M., Amplification of whistler waves in the magnetosphere, Planet. Space Sci., 20, 639, 1972.
- Bailey, D. K., Some quantitative aspects of electron precipitation in and near the auroral zone, Rev. Geophys. Space Phys., 6, 289, 1968.
- Banks, P. M., C. R. Chappell and A. F. Nagy, A new model for the interaction of auroral electrons with the atmosphere: spectral degradation, backscatter, optical emission, and ionization, J. Geophys. Res., 79, 1459, 1974.
- Bell, T. F., Wave particle gyroresonance interactions in the earth's outer ionosphere, Tech. Rept. No. 3412-5, Radioscience Lab., Stanford Electronics Labs., Stanford Univ., Stanford, Ca., 1964.
- Bell, T. F., Nonlinear Alfvén waves in a Vlasov plasma, Phys. of Fluids, 8, 1829, 1965.

- Bell, T. F., ULF wave generation through particle precipitation induced by VLF transmitters, J. Geophys. Res., 81, 3316, 1976.
- Bell, T. F. and O. Buneman, Plasma instability in the whistler mode caused by a gyrating electron stream, Phys. Rev., 133, A1300, 1964.
- Bernard, L. C., Amplitude variations of whistler mode signals caused by their interaction with energetic electrons in the magnetosphere (Ph.D. thesis); Tech. Rept. No. 3465-2, Radioscience Laboratory, Stanford Electronics Labs., Stanford University, Stanford, Calif., 1973.
- Brice, N., Fundamental of VLF emission generation mechanism, J. Geophys. Res., 69, 4515, 1964.
- Brinca, A. L., Whistler sideband growth due to nonlinear wave particle interaction, J. Geophys. Res., 77, 1972.
- Budden, J. G., Radio Waves in the Ionosphere, Cambridge University Press, Cambridge, England, 1961.
- Bud'ko, N. I., V. I. Karpman and O. A. Pokhstelov, Nonlinear theory of the monochromatic circularly polarized VLF and ULF waves in the magnetosphere, Cosmic Electrodynamics, 3, 147, 1972.
- Buneman, O., Class notes for Introduction to Plasma Physics, Stanford University, 1973.
- Burtis, W. J., Users' Guide to the Stanford VLF Ray Tracing Program, Radioscience Laboratory, Stanford Electronics Labs., Stanford University, Stanford, Calif., 1974.
- Burtis, W. J. and R. A. Helliwell, Magnetospheric chorus: occurrence patterns and normalized frequency, Planet. Space Sci., 24, 1007, 1976.

- Carpenter, D. L., Whistler evidence of a 'knee' in the magnetospheric ionization density profile, J. Geophys. Res., 68, 1675, 1963.
- Carpenter, D. L. and C. G. Park, On what ionospheric workers should know about the plasmopause-plasmasphere, Rev. Geophys. Space Phys., 11, 13, 1973.
- Carpenter, D. L. and T. R. Miller, Ducted magnetospheric propagation of signals from the Siple, Antarctica VLF transmitter, J. Geophys. Res., 81, 2692, 1976.
- Carpenter, D. L. and N. T. Seely, Cross-L plasma drifts in the outer plasmasphere: quiet time patterns and some substorm effects, J. Geophys. Res., 81, 2728, 1976.
- Crystal, T. L., Nonlinear currents stimulated by monochromatic whistler mode (WM) waves in the magnetosphere, Tech. Rept. No. 3465-4, Radioscience Laboratory, Stanford Electronics Labs., Stanford University, Stanford, Calif., 1975.
- Das, A. C., A mechanism for VLF emissions, J. Geophys. Res., 76, 6915, 1971.
- Dungey, J. W., Loss of Van Allen electrons due to whistlers, Planet. Space Sci., 11, 591, 1963.
- Dungey, J. W., Effects of electromagnetic perturbations on particles trapped in the radiation belts, Space Sci. Rev., 4, 199, 1964.
- Dysthe, K. B., Some studies of triggered whistler emissions, J. Geophys. Res., 76, 6915, 1971.
- Edgar, B. C., The structure of the magnetosphere as deduced from magnetospherically reflected whistlers, Tech. Rept. No. 3438-2, Stanford Electronics Labs., Radioscience Laboratory, Stanford University,

- Stanford, Calif., 1972.
- Gendrin, R., Pitch angle diffusion of low energy protons due to gyroresonant interaction with hydromagnetic waves, J. Atmos. Terr. Phys., 30, 1313, 1968.
- Gurnett, D. A. and L. A. Frank, VLF hiss and related plasma observations in the polar magnetosphere, J. Geophys. Res., 77, 172, 1972.
- Hanson, W. B., Structure of the ionosphere, in Satellite Environment Handbook, ed. by F. S. Johnson, pp. 25-46, Stanford University Press, Stanford, Calif., 1961.
- Helliwell, R. A., Whistlers and Related Ionospheric Phenomena, Stanford University Press, Stanford, Ca., 1965.
- Helliwell, R. A., A theory of discrete VLF emissions from the magnetosphere, J. Geophys. Res., 72, 4773, 1967.
- Helliwell, R. A., Intensity of discrete VLF emissions, Particles & Fields in the Magnetosphere, ed. by B. M. McCormac, p. 292, 1970.
- Helliwell, R. A., J. P. Katsufakis and M. L. Trimpi, Whistler-induced amplitude perturbation in VLF propagation, J. Geophys. Res., 78, 4679, 1973.
- Helliwell, R. A. and T. L. Crystal, A feedback model of cyclotron interaction between whistler-mode waves and energetic electrons in the magnetosphere, J. Geophys. Res., 78, 7357, 1973.
- Helliwell, R. A. and J. P. Katsufakis, VLF wave-injection experiments into the magnetosphere from Siple Station, Antarctica, J. Geophys. Res., 79, 2571, 1974.
- Helliwell, R. A., J. P. Katsufakis, T. F. Bell and R. Raghuram, VLF line radiation in the earth's magnetosphere and its association with

- power system radiation, J. Geophys. Res., 80, 4249, 1975.
- Helliwell, R. A. and J. P. Katsufakis, Controlled wave-particle interactions experiments, in Upper Atmosphere Research in Antarctica, ed. by L. J. Lanzerotti and C. G. Park, 1977.
- Hess, W. N., The Radiation Belt and the Magnetosphere, Blaisdell Publishing Co., Mass., 1968.
- Heyborne, R. L., Observations of whistler mode signals in the OGO satellites from VLF ground station transmitters, Tech. Rept. No. 3415/3418-1, Radioscience Lab., Stanford Electronics Labs., Stanford University, Stanford, Calif., 1966.
- Inan, U. S. and T. F. Bell, The plasmopause as a VLF wave guide, J. Geophys. Res., 82, 2819, 1977.
- Inan, U. S., T. F. Bell, D. L. Carpenter and R. R. Anderson, Explorer 45 and IMP-6 observations in the magnetosphere of injected waves from the Siple Station VLF transmitter, J. Geophys. Res., 82, 1177, 1977a.
- Inan, U. S., T. F. Bell and R. R. Anderson, Cold plasma diagnostics using satellite measurements of VLF signals from ground transmitters, J. Geophys. Res., 82, 1167, 1977b.
- Karpman, V. I., Ja. N. Istomin and D. R. Shklyar, Nonlinear frequency shift and self-modulation of the quasi-monochromatic whistlers in the inhomogeneous plasma (magnetosphere), Planet. Space Sci., 22, 1974a.
- Karpman, V. I., Ja. N. Istomin and D. R. Shklyar, Nonlinear theory of a quasi-monochromatic whistler mode wave packet in inhomogeneous plasma, Plasma Phys., 16, 685, 1974b.
- Kennel, C. F., Consequences of a magnetospheric plasma, Rev. Geophys., 7, 379, 1969.

- Kennel, C. F. and F. Engelmann, Velocity space diffusion from weak plasma turbulence in a magnetic field, Phys. Fluids, 9, 2377, 1966.
- Kennel, C. F. and H. E. Petschek, Limit on stably trapped particle fluxes, J. Geophys. Res., 71, 1, 1966.
- Kimura, I., Effects of ions on whistler mode ray tracing, Radio Sci., 1, 269, 1966.
- Laaspere, T. and R. A. Hoffman, New results on the correlation between low-energy electrons and auroral hiss, J. Geophys. Res., 81, 524, 1976.
- Liemohn, H. B., Radiation Belt Particle Orbits, Boeing Scientific Labs., Rept. No. D1-82-0116, June, 1961.
- Liemohn, H. B., Cyclotron-resonance amplification of VLF and ULF whistlers, J. Geophys. Res., 72, 39, 1967.
- Lorentz, H. A., The Theory of Electrons, ed. by B. G. Teubner, Leipzig, Germany, 1909.
- Lyons, L. R., Comments on pitch-angle diffusion in the radiation belts, J. Geophys. Res., 78, 6793, 1973.
- Lyons, L. R., General relations for particle diffusion in pitch angle and energy, J. Plasma Phys., 12, 45, 1974a.
- Lyons, L. R., Pitch angle and energy diffusion coefficients from resonant interactions with ion-cyclotron and whistler waves, J. Plasma Phys., 12, 417, 1974b.
- Lyons, L. R., R. M. Thorne and C. F. Kennel, Pitch-angle diffusion of radiation belt electrons within the plasmasphere, J. Geophys. Res., 77, 3455, 1972.

- Lyons, L. R., R. M. Thorne and C. F. Kennel, Electron pitch-angle diffusion driven by oblique whistler mode turbulence, J. Plasma Phys., 6, 589, 1971.
- Matsumoto, H., Theoretical studies on whistler mode wave particle interactions in the magnetospheric plasma, Kyoto Univ., Kyoto, Japan, 1972.
- Muzzio, J. L. R., ELF propagation in the plasmasphere based on satellite observations of discrete and continuous forms, Tech. Rept. No. 3439-2, Radioscience Lab., Stanford Electronics Labs., Stanford University, Stanford, Calif., 1971.
- Northrop, T. G., The Adiabatic Motion of Charged Particles, New York, Interscience Publishers, 1963.
- Nunn, D., A theory of VLF emissions, Planet. Space Sci., 19, 1141, 1971.
- Nunn, D., A self-consistent theory of triggered VLF emissions, Planet. Space Sci., 22, 349, 1974.
- Palmadesso, G. and G. Schmidt, Collisionless damping of a large amplitude whistler wave, Phys. Fluids, 14, 1411, 1971.
- Palmadesso, G. and G. Schmidt, Stability of a steady, large amplitude whistler wave, Phys. Fluids, 15, 485, 1972.
- Park, C. G., Whistler observation of interchange of ionization between the ionosphere and protonosphere, J. Geophys. Res., 75, 4249, 1970.
- Park, C. G., Methods of determining electron concentrations in the magnetosphere from nose whistlers, Tech. Rept. No. 3454-1, Radioscience Laboratory, Stanford Electronics Labs., Stanford University, Stanford, Calif., 1972.

- Park, C. G., The role of manmade VLF signals and noise in wave-particle interactions in the magnetosphere, Proc. International Symp. on Solar-Terrestrial Physics, Boulder, Colo., D. Williams (ed.), June 1976.
- Park, C. G. and D. L. Carpenter, Very low frequency radio waves in the earth's ionosphere, in Upper Atmosphere Research in Antarctica, edited by L. J. Lanzerotti and C. G. Park, 1977.
- Park, C. G., D. L. Carpenter and D. B. Wiggin, Electron density in the plasmasphere; whistler data on solar-cycle, annual and diurnal variations, submitted to J. Geophys. Res., 1977.
- Park, C. G. and P. M. Banks, Influence of thermal plasma flow on the mid-latitude nighttime F_2 layer: effects of electric fields and neutral winds inside the plasmasphere, J. Geophys. Res., 79, 4661, 1974.
- Raghuram, R., T. F. Bell, R. A. Helliwell and J. P. Katsufakis, Echo-induced suppression of coherent VLF transmitter signals in the magnetosphere, J. Geophys. Res., 82, 2787, 1977.
- Ratcliffe, J. A., The Magneto-Ionic Theory and Its Application to the Ionosphere, Cambridge University Press, Cambridge, England, 1959.
- Roberts, C. S., Electron loss from the Van Allen zones due to pitch angle scattering by electromagnetic disturbances, Radiation Trapped in the Earth's Magnetic Field, ed. by B. M. McCormac, D. Reidel Publ. Co., Dordrecht-Holland, 403, 421, 1966.
- Roberts, C. S., Cyclotron resonance and bounce resonance scattering of electrons trapped in the earth's magnetic field, Earth's Particles & Fields, B. M. McCormac (ed.), Reinholdt, New York, 317-336, 1968.

- Roberts, C. S., Pitch angle diffusion of electrons in the magnetosphere, Rev. of Geophys., 7, 305, 1969.
- Roederer, J. G., Dynamics of Geomagnetically Trapped Particles, Springer, New York, 1970.
- Roux, A., and R. Pellat, A study of triggered emissions, in Magneto-spheric Particles and Fields, ed. by B. M. McCormac, 209, 1976.
- Scarabucci, R. L., Interpretation of VLF signals observed on the OGO-4 satellite, Tech. Rept. 3418-2, Radioscience Lab., Stanford Electronics Labs., Stanford University, Stanford, Calif., 1969.
- Schild, M. A. and L. A. Frank, Electron observations between the inner edge of the plasma sheet and the plasmasphere, J. Geophys. Res., 75, 5401, 1970.
- Schulz, M. and L. J. Lanzerotti, Particle Diffusion in the Radiation Belts, Springer, New York, 1973.
- Smith, R. L., Propagation characteristics of whistlers trapped in field-aligned columns of enhanced ionization, J. Geophys. Res., 66, 3699, 1961.
- Smith, R. L. and N. Brice, Propagation in multicomponent plasmas, J. Geophys. Res., 69, 5029, 1964.
- Smith, R. L. and J. J. Angerami, Magnetospheric properties deduced from OGO-1 observations of ducted and non-ducted whistlers, J. Geophys. Res., 73, 1, 1968.
- Stiles, G. S. and R. A. Helliwell, Frequency time behavior of artificially stimulated VLF emissions, J. Geophys. Res., 80, 608, 1975.
- Stix, T. H., Theory of Waves in Plasmas, McGraw-Hill, New York, 1962.

- Storey, L. R. O., An investigation of whistling atmospherics, Ph. D. thesis, Cambridge University, Cambridge, England, 1953.
- Taylor, W. W. L. and D. A. Gurnett, Morphology of VLF emissions observed with the Injun 3 satellite, J. Geophys. Res., 73, 5615, 1968.
- Thorne, R. M., E. J. Smith, R. K. Burton and R. E. Holzer, Plasmaspheric hiss, J. Geophys. Res., 78, 1581, 1973.
- Tsurutani, B. T. and E. J. Smith, Postmidnight chorus: a substorm phenomenon, J. Geophys. Res., 79, 118, 1974.
- Walt, M., W. M. MacDonald and W. E. Francis, Penetration of auroral electrons into the atmosphere, in Physics of the Magnetosphere, ed. by R. L. Carovillano, pp. 534-555, D. Reidel, Dordrecht, Holland, 1969.
- Walter, F., Nonducted VLF propagation in the magnetosphere, Tech. Rept. No. SEL-69-061, Radioscience Lab., Stanford Electronics Labs., Stanford University, Stanford, Calif., 1969.
- Wang, T. N. C. and T. F. Bell, VLF/ELF radiation patterns of arbitrarily oriented electric and magnetic dipoles in a cold lossless multi-component magnetoplasma, J. Geophys. Res., 77, 7, 1174, 1972.